Processing and Characterization of Directed Energy Deposition Based Additive Manufactured SS 316 and its Composites

Submitted in partial fulfilment of the requirements
for the award of the degree of
Doctor of Philosophy
by

K BENARJI
Roll No: 717022

Under the Supervision of
Dr. Y. Ravi Kumar
Associate Professor, MED

Department of Mechanical Engineering
NATIONAL INSTITUTE OF TECHNOLOGY
WARANGAL – 506004
Telangana State, INDIA.
June - 2021

THESIS APPROVAL FOR Ph.D.

This thesis entitled **“Processing and Characterization of Directed Energy Deposition Based Additive Manufactured SS 316 and its Composites”** by **Mr. Koyilada Benarji** is approved for the degree of Doctor of Philosophy.

____

____

____

Examiner

Dr. Y. Ravi Kumar
Associate Professor, Department of Mechanical Engineering, NIT Warangal
Supervisor

Prof. A. Kumar
Head, Department of Mechanical Engineering, NIT Warangal
Chairman

NATIONAL INSTITUTE OF TECHNOLOGY

WARANGAL – 506 004, Telangana State, INDIA

CERTIFICATE

This is to certify the thesis entitled **“Processing and Characterization of Directed Energy Deposition Based Additive Manufactured SS 316 and its Composites”** submitted by **Mr. K Benarji,** Roll No. 717022, to **National Institute of Technology, Warangal** in partial fulfilment of the requirements for the award of the degree of **Doctor of Philosophy in Mechanical Engineering** is a record of bonafide research work carried out by him under our supervision and guidance. This work has not been submitted elsewhere for the award of any degree.

Place: Warangal.
Date: 22-09-2021

Dr. Y. Ravi Kumar
Supervisor
Associate Professor,
Department of Mechanical Engineering,
National Institute of Technology,
Warangal, Telangana State.

NATIONAL INSTITUTE OF TECHNOLOGY

WARANGAL – 506 004, Telangana State, INDIA

DECLARATION

This is to certify that the work presented in the thesis entitled **"Processing and Characterization of Directed Energy Deposition Based Additive Manufactured SS 316 and its Composites"**, is a bonafide work done by me under the supervision of **Dr. Y. Ravi Kumar**, Associate Professor, Department of Mechanical Engineering, NIT Warangal, India and has not been submitted for the award of any degree to any other University or Institute.

I declare that this written submission represents my ideas in my own words and where ever others ideas or words are included have been adequately cited and referenced with the original sources. I also declare that I have adhered to all principles of academic honesty and integrity and have not misrepresented or fabricated or falsified any idea/data/fact/source in my submission. I understand that any violation of the above will cause for disciplinary action by the institute and can also evoke penal action from the sources which have thus not been properly cited or from whom proper permission has not been taken when needed.

Place: Warangal.
Date: 23-06-2021

K Benarji
Roll No. 717022

ACKNOWLEDGEMENTS

I would like to express my sincere gratitude and profound indebtedness to **Dr. Y. Ravi Kumar**, Associate Professor of Mechanical Engineering Department, National Institute of Technology, Warangal for giving me an opportunity to carry out doctoral work under his esteemed supervision. This work is a reflection of his thoughts, ideas and concepts. **Dr. Y. Ravi Kumar** looks at things in the right perspective, and it has truly been a learning experience working with him. I owe a lot to him for making me a part of the continuity of the profession.

I extend my sincere gratitude to **Prof. N. V. Ramana Rao,** Director, National Institute of Technology Warangal, India for providing the necessary facilities and encouragement throughout my work.

I am thankful to **Prof. A. Kumar**, Head, Department of Mechanical Engineering, NIT Warangal and other faculty members for their encouragement and support extended during this period.

It's my great opportunity to express my deepest gratitude to the Departmental Scrutiny Committee members, **Dr. A. Venu Gopal**, Professor, Department of Mechanical Engineering, and **Dr. N. Narsaiah,** Professor, Department of Metallurgical and Materials Engineering, and **Dr. Syed Ismail,** Assistant Professor, Department of Mechanical Engineering, for their adeptness and many discussions during this research period.

I am grateful to **Dr. C. P. Paul,** Head, **Laser Additive Manufacturing Laboratory,** and Raja Ramanna centre for advanced Technology, Madhya Pradesh, for his constant support and motivation to carry out my experimentation and research work.

I am thankful to **A. N. Jinoop**, Senior research fellow, Laser Additive Manufacturing Laboratory, and Ramanna centre for advanced Technology, for his encouragement and support extended during this period.

I express my sincere thanks to my co-scholars **S. Rakesh, V.V. Narayana and A. Srikanth,** NIT Warangal for their support and help in completion of this thesis.

I am thankful to **Mr. H Kumar, Mr. C H Premsingh and Mr. U Kumar,** technical staff of Laser Additive Manufacturing Laboratory, **and Mr. Dileep Kumar, Mr. Saurav Nayak and Mr. Sunil Yadav,** Research fellows at Ramanna centre for advanced Technology, for their support in sample deposition and cutting.

I would like to extend my heartfelt thanks to **Mr. B. Rangilal, Mr. G. Ilaiah** and **K. Raju** technical staff of Production Engineering Lab and **Mr. M. V. Vijay Kumar** Office staff of Mechanical Engineering Department, NIT Warangal for their constant help and encouragement.

I am thankful to **Asit Kumar Khanra**, Head, Department of **Metallurgical and Materials Engineering**, NIT Warangal and other faculty members for their support for material characterization during this period

A special debt of deep gratitude to my wife, family members for their unceasing sacrifices, endeavors and encouragement.

Finally, I would also like to acknowledge the help given by all the persons who have directly or indirectly supported the work.

Koyilada Benarji

Research Publications

International Journals

1. **K. Benarji** , Y. Ravi kumar , C. P. Paul , A. N. Jinoop , K S Bindra, Parametric Investigation and Characterization on SS 316 built by Laser assisted Directed Energy Deposition, Proceedings of the Institution of Mechanical Engineers, Part L: Journal of Materials: Design and Applications 2019, 234(3), PP: 452-466, **SCI (Impact factor: 2.014)**

2. **K. Benarji** , Y. Ravi kumar , A. N. Jinoop , C. P. Paul , K S Bindra , Effect of Heat-Treatment on the Microstructure, Mechanical Properties and Corrosion Behaviour of SS 316 Structures Built by Directed energy deposition Based Additive Manufacturing", Metals and Materials International, 2021, 27, 488-499. **SCI (Impact factor: 1.990)**

3. **K. Benarji** , Y. Ravi kumar , A. N. Jinoop , C. P. Paul , K S Bindra, Effect of WC composition on the Microstructure and Surface Properties of Laser Directed Energy Deposited SS 316-WC Composites, Journal of Materials Engineering and Performance, 2021. **SCI (Impact factor: 1.652)**

4. **K. Benarji**,Y. Ravi kumar, P. Ashwin, Numerical simulation and experimental study on austenitic stainless steel by laser assisted metal deposition (L-MD), Materials Today: Proceedings, 2020, 39, 1497-1502. **Scopus**

ABSTRACT

Directed energy deposition (DED) is one of the metal additive manufacturing processes, used for building components with complex geometry and high relative density. In the present work, processing and characterization of DED based additive manufactured Stainless Steel 316 (SS 316) and its composites are performed. Initially, parametric investigation and characterization of SS 316 built by DED are performed. Full factorial experimental design is carried out by varying process parameters such as laser power, scanning speed and powder feed rate. The effect of DED process parameters on the track geometry, deposition rate and micro hardness is investigated and three different combinations of process parameters yielding maximum deposition rate and hardness is identified for bulk investigation. The identified process parameters are laser power of 1000 W, powder feed rate of 8 g/min and scanning speed of 0.4 m/min, 0.5 m/min and 0.6 m/min. Finite element analysis of DED is performed to understand the effect of process parameters such as laser power, scanning speed and powder feed rate and on the track height and width. The significant rise in track width and height with an increase in laser power and powder feed rate, whereas reduction in track width and track height is observed with an increase in scanning speed. The finite element analysis of track width and track height agrees well with the experimental results.

DED built SS 316 bulk structures reveal the presence of austenitic phase (γ) at all the conditions. However, the ferrite (δ) peak is observed at 0.6 m/min due to micro-segregation and thermal gradients. The minimum crystallite size is estimated to be 24.88 nm at 0.6 m/min. The fine columnar dendritic structure is observed in DED samples at all conditions. An average micro hardness of 317.4 $\mathrm{HV}_{\mathbf{0.98\ N}}$ is obtained at 0.4 m/min and it is observed that micro-hardness reduces with an increase in scanning speed mainly due to increase in lack of fusion and porosity. Tribology studies are carried out at different values of normal load and sliding velocity. The minimum specific wear rate of $0.02497 \times 10^{-4} \mathrm{mm}^3/\mathrm{Nm}$ is observed at scanning speed of 0.4 m/min. Scanning electron microscope (SEM) of the wear tracks analysis shows abrasive wear as the major wear mechanism.

Subsequently, investigations on the effect of heat-treatment on the microstructure, mechanical, tribological and corrosion characteristics of DED built SS 316 bulk structures are carried out. DED built SS 316 structures are subjected to solution treatment at 1073 K (HT1073) and 1273 K (HT1273) and reduction in ferrite phase with heat-treatment is observed from microstructure. X-ray diffraction and microstructure shows that the austenite phase is observed at all conditions and reducing ferrite phase intensity is noticed with an increase in heat-treatment temperature. Improvement in the plasticity retaining capability and reduction in micro-hardness due to reduction in the volume fraction of ferrite and increasing grain size with heat-treatment. It is observed that the corrosion rate and specific wear rate increases after heat-treatment. The maximum specific wear rate of 0.19375 x 10^{-4} mm^3/N-m is observed in the HT1273 sample with wide and deep grooves noticed on the worn-out surface of heat-treated samples. The SEM images of wear tracks are characterized with abrasive wear mechanism for as-built sample, while heat-treated samples shows plastic deformation, followed by spalling effect.

Further, investigations are performed on SS 316 - tungsten carbide (WC) composites built using DED by varying the WC volume fraction from 6% - 10%. The built structures are subjected to characterizations to investigate the effect of WC volume fraction on the relative density, microstructure, micro-hardness and tribological properties of SS 316-WC composites. It is observed that the relative density of composite reduces with an increase in the volume fraction of WC particles. The microstructure is primarily dendritic, and XRD analysis revealed the presence of WC and γFe phases with a minimum crystallite size of 18.82 nm at 10% of WC in SS 316. The improvement in corrosion resistance is identified with the addition of WC, and the least current density of $1.47\,\frac{\mu A}{cm^2}$ is identified with 8% of WC. The micro hardness of the composite is observed to increase with an increase in the WC content and the wear rate is observed to reduce with an increase in WC content. Maximum hardness of 399.5 HV$_{0.98N}$ and minimum wear rate of 0.03107 ×10^{-4} mm^3/Nm are obtained at 10% of WC. Scanning electron microscopy images indicates the presence of parallel grooves, wear debris and plastic deformation on the wear tracks.

Keywords: Laser Additive Manufacturing, Directed Energy Deposition, Stainless steel 316, Heat-treatment, SS 316 Composites, Characterization

CONTENTS

LIST OF TABLES

LIST OF FIGURES

ABBREVIATIONS

DED	Directed energy deposition
BJ	Binder jetting
SLS	Selective laser sintering
LOM	Laminated object manufacturing
AM	Additive manufacturing
LAM	Laser assisted additive manufacturing
MAM	Metal additive manufacturing
XRD	X-ray diffraction
FWHM	Full width at half maximum
PBF	Powder bed fusion
P-DED	Powder based direct energy deposition
W-DED	Wire based direct energy deposition
SWR	Specific wear rate
SLM	Selective laser melting
COF	Coefficient of friction

NOMENCLATURE

P	Laser power
v	Scanning speed
m	Powder feed rate
E	Laser energy per unit length
F	Powder feed per unit length
λ	Wave length of X-ray
r	Laser beam radius
k	Thermal conductivity
ρ	Density
α	Solid and liquid interface angle
β	Full width half maximum
T	Temperature
C_p	Specific heat capacity
d	Crystallite size
ε	Emissivity
T_0	Room temperature
h	Heat transfer coefficient
A_t	Track area
η	Powder efficiency
V_n	Boundary velocity
Q_r	Heat source
Q_{loss}	Heat loss by convention and radiation
σ_b	Stefan-Boltzmann constant
G	Temperature gradient
R	Solidification rate
C	Scherrer constant
θ	Peak position in radians
E_{corr}	Corrosion potential
I_{corr}	Corrosion current density

β_A	Anodic Tafel constant
β_C	Cathodic Tafel constant

CHAPTER I

INTRODUCTION

1.1. Introduction

Additive manufacturing (AM) is the process of building the component layer by layer fashion from three-dimensional model data, as opposed to subtractive additive manufacturing. It can be called layer manufacturing, rapid prototyping, rapid manufacturing, additive process, additive fabrication, direct digital manufacturing, and solid freeform fabrication [1]. The typical cycle of AM process is shown in figure 1.1.

It can fabricate complex geometries with the absence of special fixtures and also reduces the number of spare parts required for final assembly.AM process can build prototypes and functional parts for industrial applications and services [2]. It can produce intricate and customized parts (lattice structures and cooling channels) without any expensive tools like punches, dies, cutting tools, and casting molds and also reduces the steps involved in the conventional process. In addition, it can build parts on demand resulting in low inventory and decreasing lead time [3]. However, AM cannot replace the position of the conventional process for high volume production [4-5] and the application is also limited by residual stresses and anisotropy nature of the developed component. The component with straight cuts and the round hole is easily fabricated by AM process. AM process can directly produce functional parts resulting in a minimum number of spare parts required for assembly, and also reduce lead time, production cost and material wastage. Metals, ceramics, polymers and composites are generally used materials in AM technologies. Therefore, AM technologies are used in different applications such as medical [6], aerospace [7], marine, automotive [8], and energy applications [3, 9–12]. AM cannot replace conventional process completely but is one of the tool boxes which facilitates the design freedom to engineering. It is not suitable for large production runs and limited to small to medium complex parts. AM shortens the supply chain, transportation cost, time and conserve energy [13]. According to the American Society for Testing of Materials (ASTM), AM technologies are mainly categorized into seven types such as powder bed fusion (PBF), direct energy deposition (DED), vat-photo polymerisation, material jetting (MJ), binder jetting (BJ), material extrusion and sheet lamination

[14]. Polyamide, acrylonitrile-butadiene-styrene (ABS), photo-curable resin, polycarbonate, wax, metal/ceramic/polymer powders, adhesive coated sheets, etc. are used in AM process.

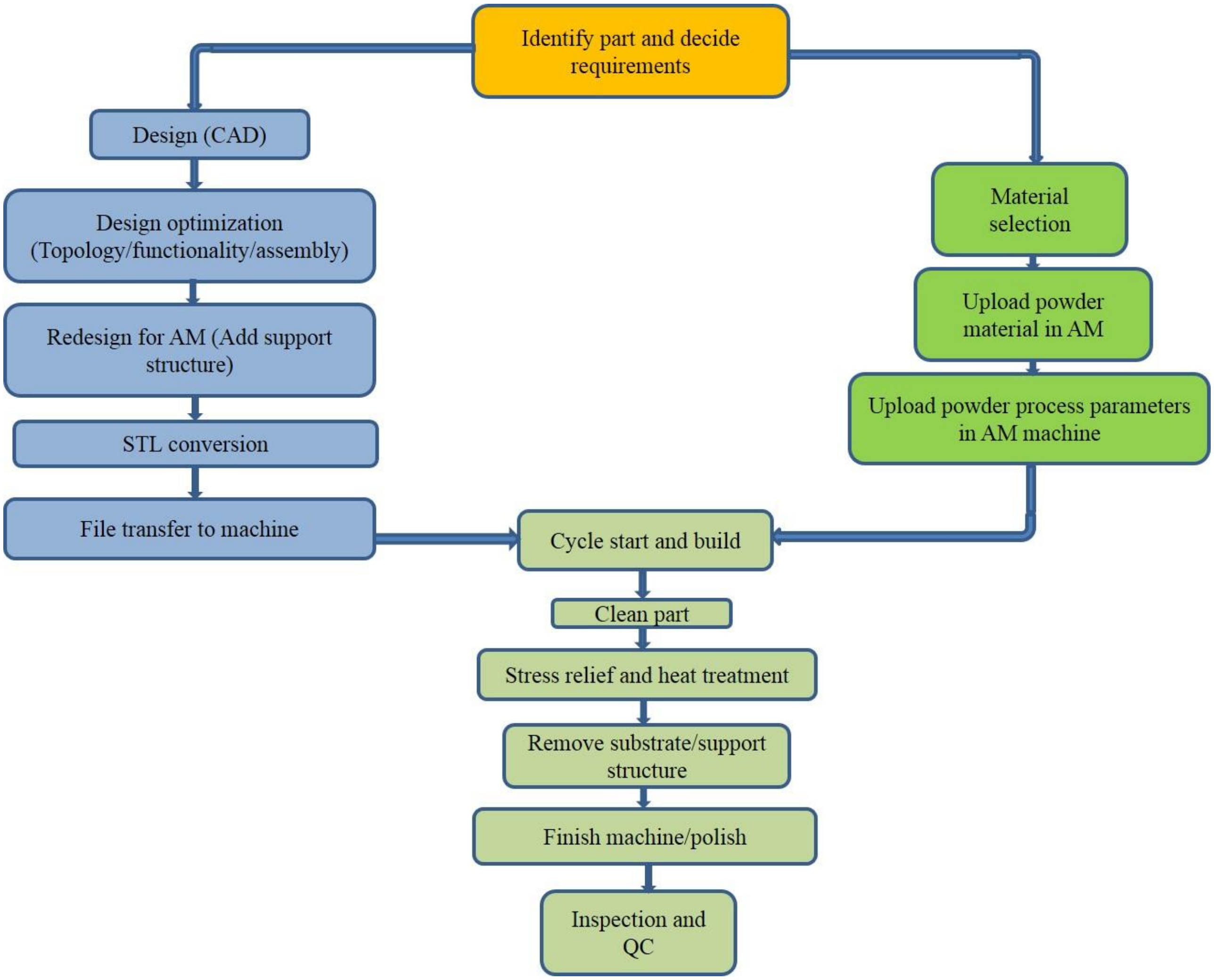

Figure 1.1 Typical AM process cycle [4]

1.2. Metal additive manufacturing

Revenue from metal printed parts is increased by 41.9%, maintaining a five-year trend of above 40% growth each year for additive manufacturing [5]. The parts manufactured by MAM process have a fine microstructure and consequently higher yield strength as compared to the conventional process. Therefore, the aerospace and automotive industries are most interested in the MAM components [11]. Therefore, it is mandatory to understand the behaviour of material properties, microstructure and processing method to high quality, reliable and qualified parts for engineering applications.

The major metal processing AM techniques are sheet lamination (SL), binder jetting (BJ), powder bed fusion (PBF) and directed energy deposition (DED) [15].The classification of MAM process is shown in figure 1.2. Powder bed fusion is further classified based on the heat source (laser /electron beam) and type of melting (Partial/ full melting). The metal parts can be produced indirectly by using binder/ ultrasonic vibrations to combine metal particles/metal foils. The final part with full density is obtained after post-processing. Examples of indirect methods are selective laser sintering (SLS), laminated objective manufacturing (LOM) and binder jetting (BJ). In SLS process, metal parts are manufactured by partial melting of powder particles or low melting point of binder to help powders particles bind together. The post-treatment of the final part (curing, thermal sintering and infiltration) is required to achieve full density components. In LOM process, the sheet foils have joined layer by layer using ultrasonic vibration, and the required geometry is attained by laser cutting. In SLM/EBM process, laser/electron beam sinters the powder layer by layer as per sliced data and bonding powder particles are achieved by full melting.

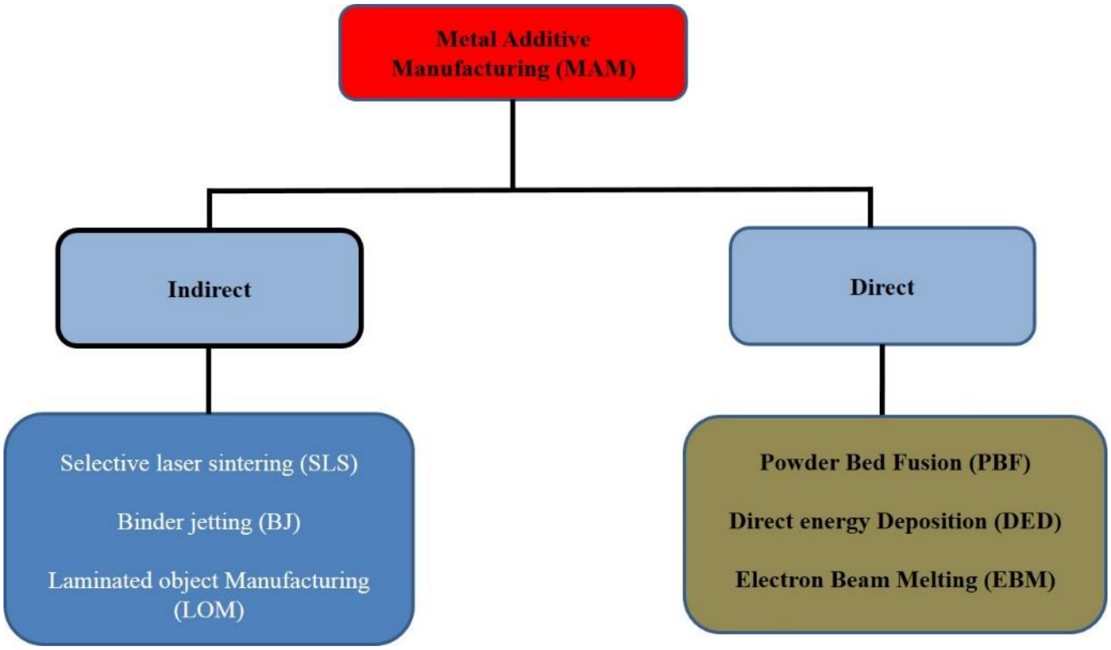

Figure 1.2 MAM classifications [2]

In direct Metal AM, material feed in the form of wire or powder, but most commercial methods use powder as raw material. Examples of direct metal AM processes are PBF and DED [2]. In DED process, a laser melts the fed metal powder/wire and deposit it over the build plate or substrate. The full density components are achieved with AM direct processes like SLM, EBM and DED and their mechanical properties are equivalent to metals manufactured by conventional methods [16]. The full density parts are directly achieved by powder bed fusion and direct energy deposition.

The raw material is used in different forms based on the AM process. For example, powder (powder bed fusion, DED), wire (WDED) and sheet (LOM). The AM technologies such as SLS, SLM, EBM and DED are successfully processed different alloys such as iron alloys, aluminum alloys, titanium alloys, nickel alloy and cobalt alloys. Some of them are summarized in Table 1.1

Table 1.1: Materials processed in additive manufacturing

Alloy	**Grade type**
Stainless steel alloys (SS)	SS 304, 304 L, 316 and 316 L
	SS 304, 304 L and 316 L
Precipitation hardening (PH) stainless steel	17-4 PH
Nickel base alloys	Invar 36, Inconel 625 and Haynes 230
	Inconel 718
	Inconel 625, Inconel 718
Titanium alloys	Ti6Al4V
Aluminum alloys	AlSi10Mg, AlSi10
Cobalt alloys	Co-Cr

Ceramic materials used in AM process are alumina, zirconia and silica. Ceramics are used in vast applications due to their exceptional properties such as chemical resistance and high-temperature resistance. The complex ceramics parts are difficult to achieve by conventional methods due to their hardness. Composites are made from two or more constituent materials with noticeably different physical or chemical properties. AM technology can be used for manufacturing polymer, ceramic and metal based composites by adding fiber and ceramic particles. Metal based composites such as Ti-TiC, Ti-TiN and IN 625-TiC were successfully manufactured by AM process [17]. Functionally graded materials (FGM) are successfully deposited using DED process and FGM is one of the primary advantages of AM technology which cannot possible by conventional methods. DED process is typically opted for fabricating FGM parts and examples include SS304 L+ IN 625, SS 316L+ IN 625, Ti-6Al-4V+ AlSi10Mg etc [18].

The major MAM processes used for different applications are summarized below.

1.2.1 Binder jetting process

The Massachusetts Institute of Technology (MIT) founded binder jetting (BJ) in 1993 and Z Corporation secured a license for the process from MIT two years later. BJ process is initially opted for polymers subsequently ceramics. However, BJ process was opted for metal materials from early 2000's [19]. The working principle of BJ process is similar to PBF but the laser is replaced by the binder droplets (~80 µm). The schematic diagram of BJ process is shown in figure 1.3.

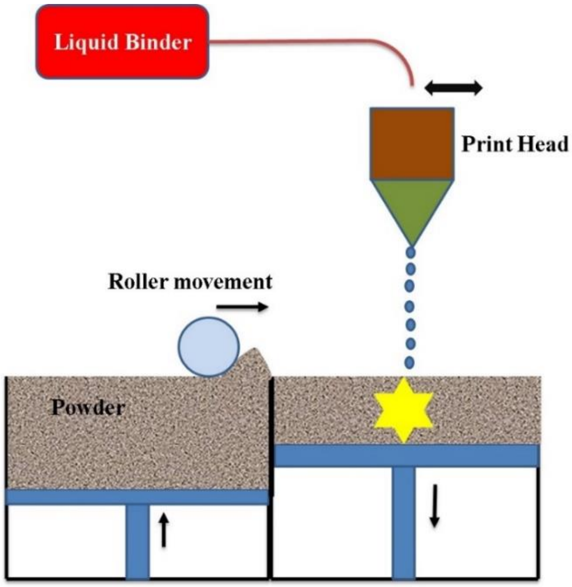

Figure 1.3 Schematic of binder jetting process [1]

Binder droplets from inkjet nozzles are deposited over the powder and act as binding material between powder particles and deposit one layer over the bed as per design data [5, 20]. The powder bed is lowered by one layer thickness and subsequently deposit the second layer. In this way, the process continues to develop the final green part. It is most suitable for materials like polymers, metals and composites. The final green part is subjected to different post-processing techniques: curing, de-powdering, sintering, infiltration, annealing and finishing [5, 12]. The density of stainless steel is increased from 60 to 95% when bronze is used as infiltrate, and similarly, cobalt and aluminum are used as infiltrates for tungsten carbide and boron carbide respectively [1]. BJ process offers high feature resolution and can build hollow cooling passages on a larger scale than the PBF process. It allows design freedom which is not possible by the conventional process like forging, casting and machining. The advantages of the BJ process are large build volumes, high print speed, multi-material per build, self-supporting, and no support structures like powder bed fusion [13]. The process parameters of the BJ process are shown in figure 1.4.

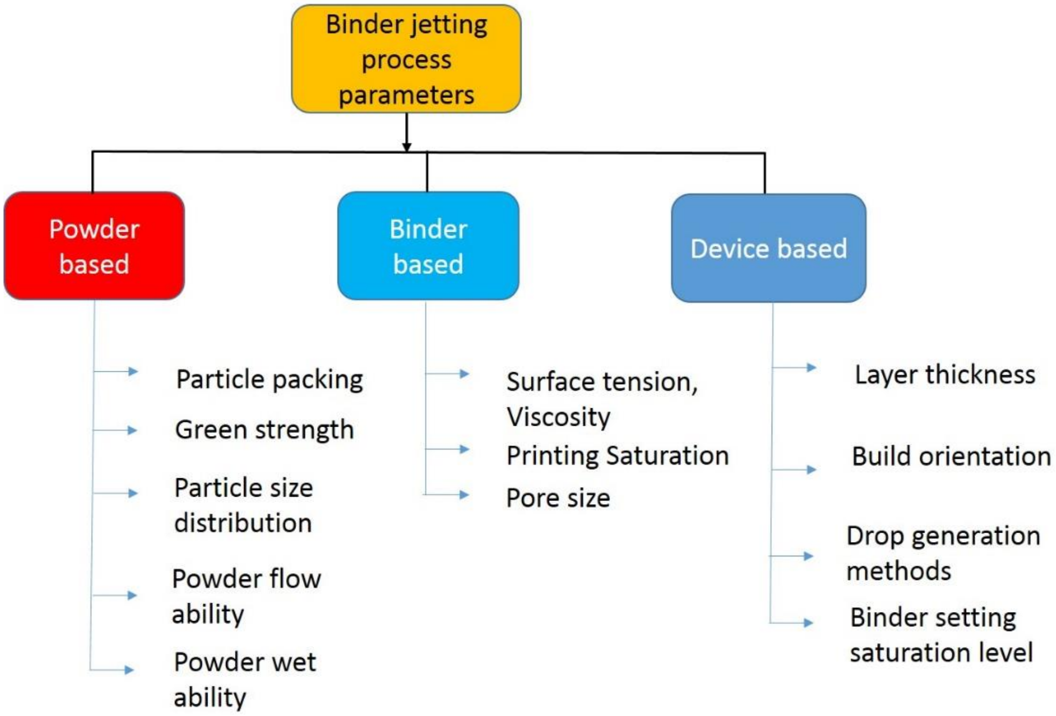

Figure 1.4 Process parameters of BJ process [19]

1.2.2 Laminated object manufacturing (LOM) process

In LOM process, raw material is used in the form of a sheet. The laser cuts the sheet as per the required contour from three-dimensional data when the sheet is laid over the substrate for the first layer. The strong bonding between two successive layers is achieved by moving a hot roller to compress the layer and activating heat-sensitive adhesive paper [9, 15, 21]. The schematic diagram of the LOM process is shown in figure 1.5. The LOM process is classified based on the bonding mechanism between sheet layers includes adhesive or gluing, clamping, thermal bonding and ultrasonic welding. LOM process eliminates the distortion, phase transformation and solidification defects but limited complexity in parts compared to other AM processes [14, 22]. Gluing and bonding can be done in two different ways based on the order followed as, a) bond-then-form (First bond the sheet to substrate and then form the required cross-section), b) form-then-bond (First cut the sheet in the required cross-section and sticks to the substrate).

In the clamping process, metal laminates are fabricated using bolts or clamping rather than thermal and adhesive bonding. Thermal bonding is one of the mechanisms successfully applied for sheet lamination of functional tooling and metal parts.

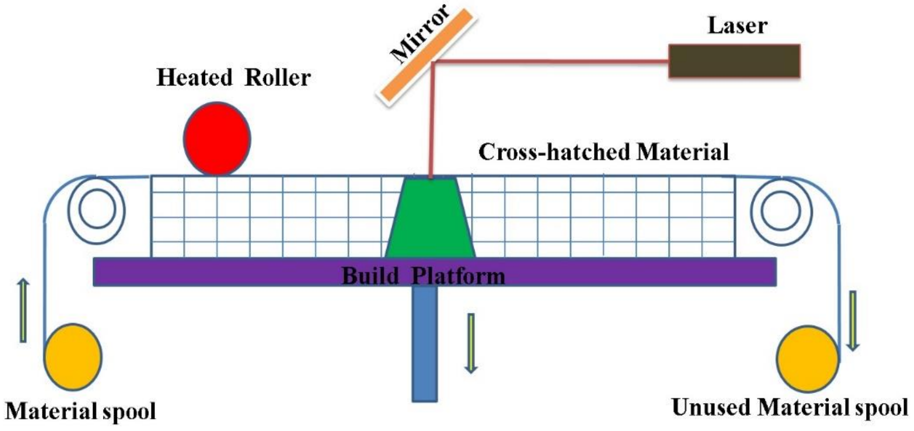

Figure 1.5 Schematic of laminated object manufacturing process [4]

In the ultrasonic additive manufacturing (UAM) process, sheet foil is placed over the base plate or previously deposited layer. Subsequently, sonotrode oscillates and travel along with the sheet joint with a frequency of 20 kHz. The sonotrode oscillations are normal to the moving direction [23, 24]. Here, the required geometry of each layer is achieved by computer numerical controller (CNC) milling. This hybrid process continues for each sheet foil until the final part is fabricated. It is successfully applied to titanium, aluminum and copper sheet foils. The process parameters used in UAM process are oscillation amplitude, normal force, sonotrade travel speed, preheat temperature and foil thickness. Aluminum alloy (6061) is successfully fabricated using UAM process [25].

1.2.3 Selective laser sintering (SLS) process

It consists of a controller unit, roller mechanism, part process chamber, scanner system, CO_2 laser and atmosphere control system. Initially, the chamber is preheated to a temperature below the melting point of powder material and deposit layer as per required thickness using the roller and consequently, laser scans the powder layer as per design [9]. In the SLS process, parts are fabricated by partial melting or melting of low melting point binders to help metal powder particles stick together. The binders commonly used SLS process are low melting point metal and polymers (phenolic polymer).

It can build components using different materials such as polymers (polyvinyl chloride (PVC), Polyethylene (PE), Polypropylene (PP), Polymethyl methacrylate (PMMA), Polystyrene (PS), Polyethylene terephthalate (PET), Polyamide (PA) and Plycarbonate (PC)), metals (cobalt-based, nickel-based, bronze-nickel, pre-alloyed bronze-nickel, 28 Inconel 625, Ti- 6Al-4V, stainless steel, gas-atomized stainless steel 316L, AISI 1018 carbon steel, high-speed steel precoated), ceramics (Al_2O_3, FeO, NiO, ZrO_2 , SiO_2 and CuO), cermets and composite materials, bio-material metals–polymers and metals–ceramics combinations. The post-processing is generally required to attain full density components and it comprises binder removal, thermal sintering and liquid metal infiltration (if required). Figure 1.6 represents the classification of SLS process parameters based on the different modes. The SLS process parameters such as scanning speed, layer thickness, laser power, laser beam density, hatch spacing and scanning pattern have a significant influence on the final properties of the component. Therefore, the selection of optimum combination of process parameters significantly influences the surface finish, built rate and mechanical properties of the final part. The parts developed using SLS are used in engineering and medical applications such as aerospace, automotive, wind tunnel, investment casting, tooling, metallic moulds for injection moulding, turbine, implants, prosthesis and tissue engineering etc.

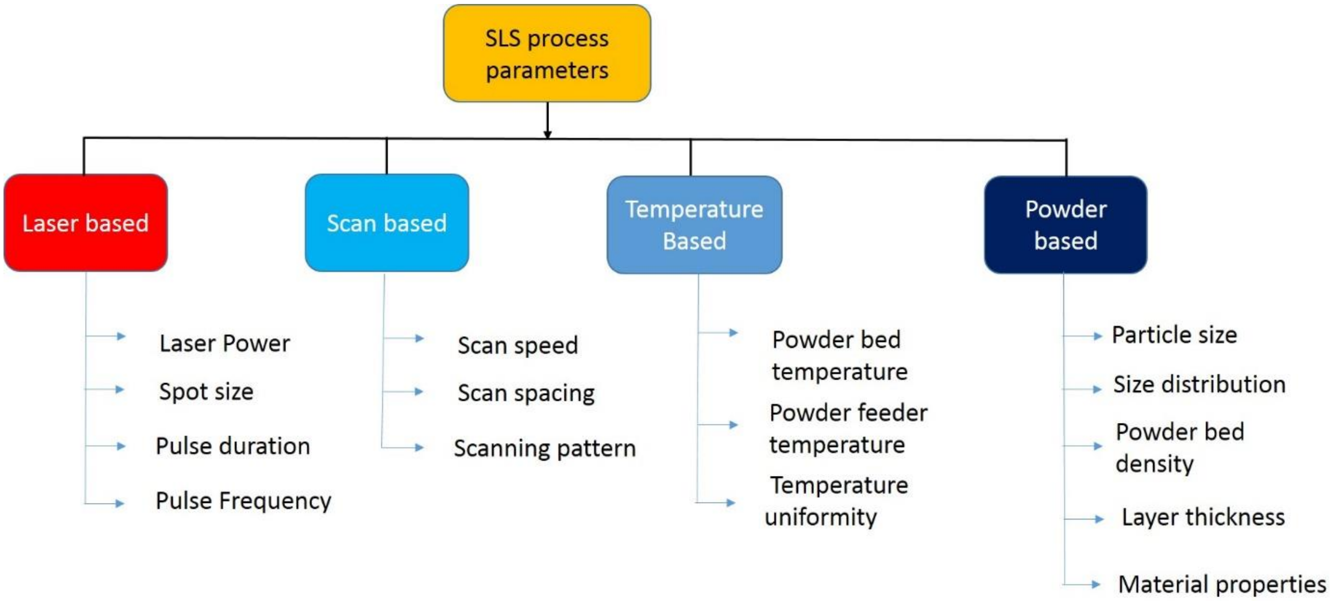

Figure 1.6 Process parameters of selective laser sintering [26]

1.2.4 Laser Additive Manufacturing (LAM)

Laser Additive Manufacturing (LAM) is non-contact process and it can be used for process different materials additively. LAM is a widely used metal additive manufacturing process for building components in a layer-by-layer fashion using high-power lasers as an energy source. LAM is being used for various industrial applications such as aerospace, automotive, electronic, chemical and biomedical [27, 28]. The major advantage is the fabrication of complex shapes without any dedicated tool, with minimum production time and material wastage. Thus, it eliminates the need for complex assemblies for building complex shapes and also provides design flexibility for building geometries not possible by conventional manufacturing techniques. One such example is the manufacturing of mold and dies with conformal cooling channels using LAM, which plays a vital role in terms of cooling effect in casting and injection molding. In addition, LAM can build the entire shape without joining different parts, consequently avoiding joint failures and weak structures. The major freedoms offered by LAM are shape design freedom, material design freedom, logistics freedom, and post-processing freedom [27]. On the process side, LAM possesses higher processing speed and solidification velocity leading to high cooling rates (~ 105 K/s). This results in finer microstructure and better mechanical strength than as-cast samples [29]. LAM can be primarily classified: Laser-assisted Powder Bed Fusion (L-PBF) [30, 31] and Laser-assisted Directed Energy Deposition (L-DED) [32, 33] as shown in figure 1.7. The basic difference lies in the methodology deployed for material feeding. L-PBF uses a blade/roller to spread a thin layer on the substrate and uses a laser to melt the powder selectively based on the required shape. L-PBF is further classified based on the full melting (selective laser melting) and partial melting (selective laser sintering). However, DED involves in-situ feeding of shapeless material like wire or powder onto the melt pool created by high laser power. L-PBF is used for building thin-wall components with fine features, undercuts, overhangs, etc. However, the applications of DED include repairing, remanufacturing, cladding and the building of engineering components etc. [27, 32]. The productivity, capability and quality of AM process are influenced by the type of heat source, energy density, scanning speed, scanning strategy, feeding system and inert gas. The high-power lasers (200 W to 6 kW) are generally used in commercially available systems. Nd: YAG, CO_2, Fibre and diode lasers are generally selected for the LAM process.

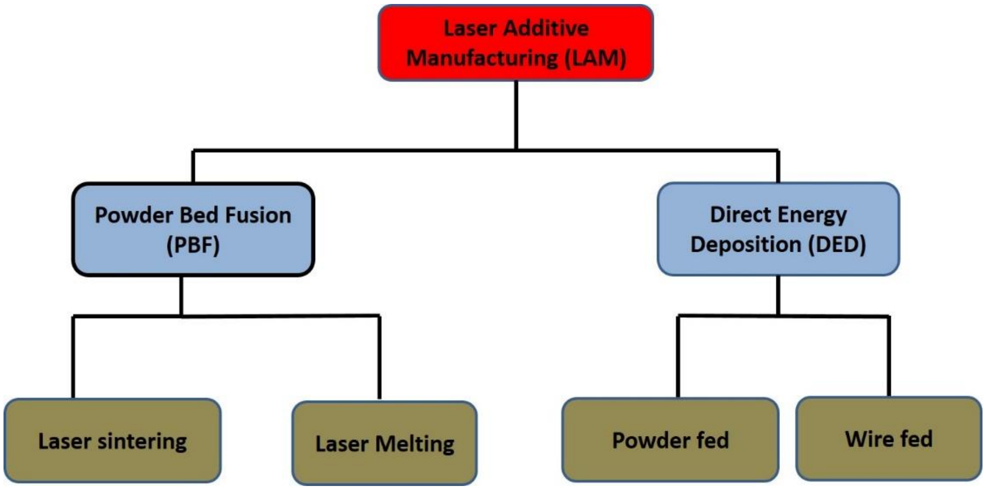

Figure 1.7 Classification of Laser additive manufacturing process [27]

The absorptivity of metal is determined by laser wavelength [4]. Nd: YAG, Fibre and diode lasers are short-wavelength lasers that are generally opted for MAM process due to high absorptivity. The spot size varies from process to process, for example, 50-400 µm range for PBF and 500 µm-3 mm for DED process [27]. The typical process parameters used in LAM processes significantly influence the final composition and mechanical properties of the component.

1.2.4.1 Powder bed fusion process

Powder bed fusion (PBF) is one of the additive manufacturing technologies and used for fabricating complex shapes with high resolution, hollow cooling passages [4,36]. Selective laser sintering (SLS) and selective laser melting (SLM) are two of the most used PBF methods. SLM is also termed direct metal laser sintering (DMLS). The laser is selectively sintered the cross-section one after the other as per sliced 3D data until reached the required shape. The un-sintered powder act as mechanical support during the process [37]. Full density components can be obtained with SLM after post heat treatment. If an electron beam replaces the laser source, this process can be called electron beam melting (EBM). Only limited materials like Ti6Al4V, Inconel 718, CoCrMo and Ti grade 2 are processed by EBM due to high operating cost, slow process, limited size, expensive and difficulty in optimizing process parameters. It is processed under vacuum conditions, unlike the selective laser melting (SLM) process and consequently low chance of porosity. Brittle materials (intermetallic (TiAl) and entropy alloys (NiCrCoTiVAl)) are difficult to process using SLM due to high cooling rates whereas successfully processed by EBM process by maintaining optimum bed temperature of 870 K [12].

The main components of PBF are powder supply piston, sintering piston, feeding roller, laser, control system, powder bed and inert gas supply system as shown in figure 1.8. The powder morphology, powder packing and size distribution have a significant effect on the porosity of the component. The fine spherical powder without too many satellites and average particle size distribution (10-45 µm) are used in PBF process to improve process efficiency [4, 5]. It can be processed by single material per built and unsuitable for multi-material [38]. The whole process is carried out under inert gas (Argon and Nitrogen) atmosphere, which can avoid further unwanted reaction of gas elements with powder material. For example, aluminum reactive with the presence of oxygen in the atmosphere tends to the oxide layer formation which indirectly deteriorates the mechanical properties of the component. PBF is subjected to complex physics and chemical phenomena including heat and mass transfer, and also light energy absorption. PBF process is subjected to high cooling rates (10^3-10^8 K/s) due to the small melt pool size (in microns) and the minimum interaction time between the laser beam and powder particles (high scanning speeds).

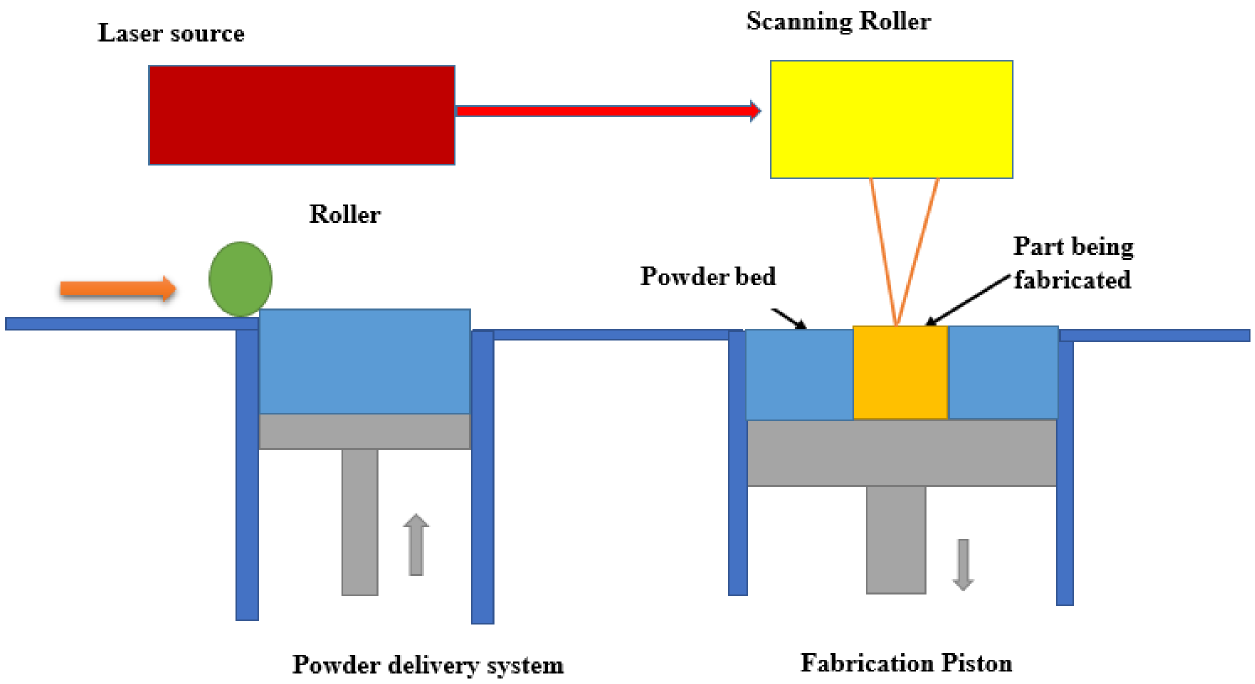

Figure 1.8 Schematic diagram of powder bed fusion [27]

The unique microstructure and improvement in mechanical properties can be acquired due to the high cooling rates [39]. Apart from this, it improves chemical homogeneity and dislocation density, and modifies the microstructure with grain refinement. Moreover, the output product of PBF can be directly used in applications where it is required with minimum post-processing steps. Selecting appropriate input process parameters are much more important during PBF process and categorized based on the laser, powder, and process as shown in figure 1.9. PBF can process materials like plastics, metals, and ceramics but most research has been focused on metallic components and their alloys. Titanium, steel, aluminum, copper, and nickel-based alloys and their composites [12] are successfully fabricated by PBF, which exhibits superior performance over these alloys fabricated by the conventional methods [40]. However, PBF works on limited powder materials, hence further research has been focused on promoting additive technology into the different material fields.

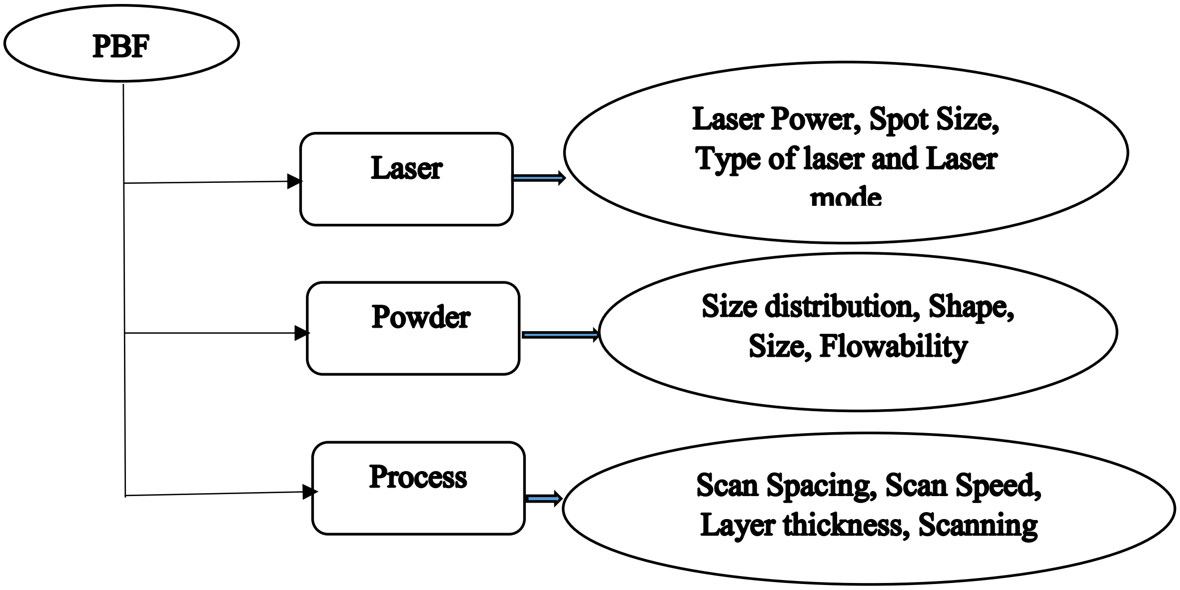

Figure 1.9 Process parameters involved in SLM process [27]

1.2.4.2 Directed energy deposition

In Directed energy deposition (DED), the laser creates a melt pool on the surface of the substrate or previously deposited layer onto which the raw material is added under the presence of inert gas to protect the oxidation of the melt pool. The movement of the laser head or sample is controlled by a CNC workstation or robotic arm. Generally, the substrate/sample is moved in the XY plane and laser head is moved in the Z direction. Thus, layer by layer building of component is achieved and built the final 3D engineering component. Figure 1.10 presents the typical schematic of DED system. The DED is classified based on the feeding material (wire or powder). The DED has advantages over other metal AM by the ability to build large structures, high deposition rates, full density parts, repair damaged parts and allow multiple materials in a single build [4]. The DED process can be powder fed deposition (PFD) or wire fed deposition (WFD) based on the material form (powder or wire) used for building the component.

The PFD system comprises of powder and gas delivery system. The powder delivery system supplies powder to deposition point by a carrier gas (Helium and Argon). The argon gas acts as shielding gas for reactive materials. It is the most convenient and extensively used in DED process. When laser from coaxial nozzle passes through powder cloud turns into melt pool is deposited over the substrate or previously deposited layer. The effective utilization of energy depends upon the absorptivity of powder and multiple internal reflections within the powder. The angle of powder feeding with coaxial nozzle is deciding factor on the final deposition rate and mechanical properties of the part.

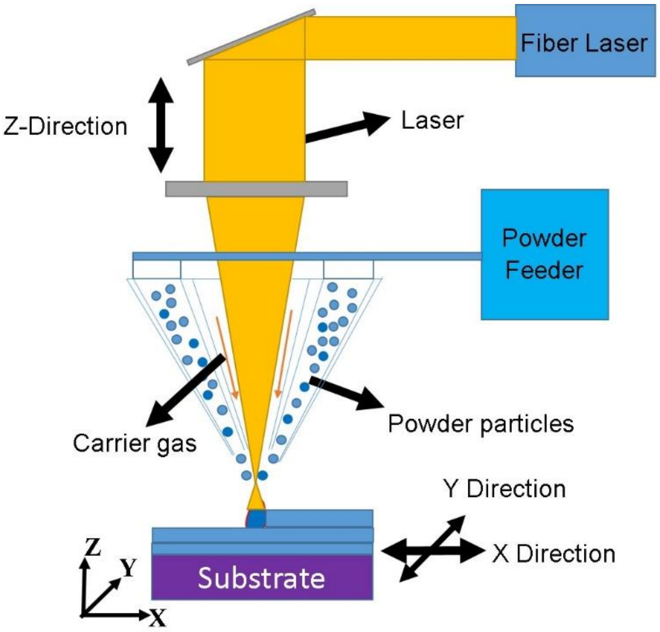

Figure 1.10 Typical Schematic of PFD system

In WFD system, molten pool deposited over the substrate or previously deposited layer when laser melts the feeding metal wire from the nozzle as shown in figure 1.11. The 100% deposition rate can be achieved by the WFD process than PFD process [4]. The entire system is closed with an inert atmosphere to protect from oxidation. The process parameters involved in WFD play a key role in the properties of the material. The wire feed rate, wire tip position in the molten pool, laser power, laser spot size, traverse speed, feed direction and feed angle plays a vital role in a stable process. The wire feed rate and standoff distance are affected by changing the angle between the laser beam and wire. The melting efficiency depends on the position of the wire tip relative to the melt pool. The shape and size of the melt pool are disturbed by improper positioning of wire tip and wire feed rate resulting in the non-uniform deposition. The optimum ratio between beam diameter and wire diameter should be greater than 3 to attain the smooth surface and good metallurgical bond between the substrate and deposited layer. DED can be termed as laser engineered net shaping (LENS), direct metal deposition (DMD), 3D laser cladding, direct light fabrication, laser freeform fabrication (LFF), laser-based metal deposition (LBMD) and laser consolidation, etc. Different organizations named DED process based on the type of laser, laser power and spot size, inert gas, and powder feed and motion control methods utilized. The typical process parameters involved in DED process as shown in figure 1.12. It can fabricate the large volume, and repair damaged parts can be used as a substrate or build rate. It offers a higher deposition rate, full dense parts, and multi-material in a single build (Functional graded materials) as compared to PBF process [9,16].

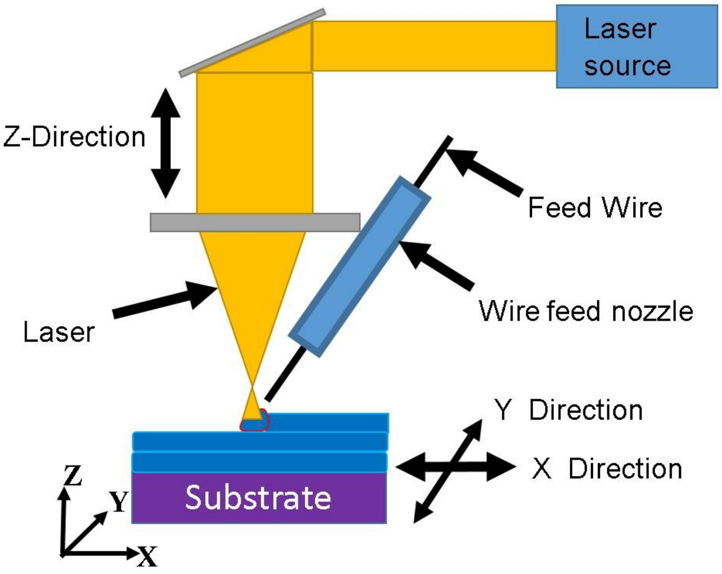

Figure 1.11 Schematic diagram of WFD system

The mechanical properties of DED deposited part can be tuned by controlling microstructure through chemical composition and thermal gradients. DED process is also coupled with the milling process to improve surface finish and dimension tolerance [5]. DED is successfully used for processing a wide variety of materials like Fe-based alloys [41, 42], Ni-based alloys [29, 43], Co-based alloys [44, 45] etc. for various engineering applications. DED can be an option for building near net-shaped structures without significant material loss and reducing the wastage of expensive metals like Ni, Cr and Mo.

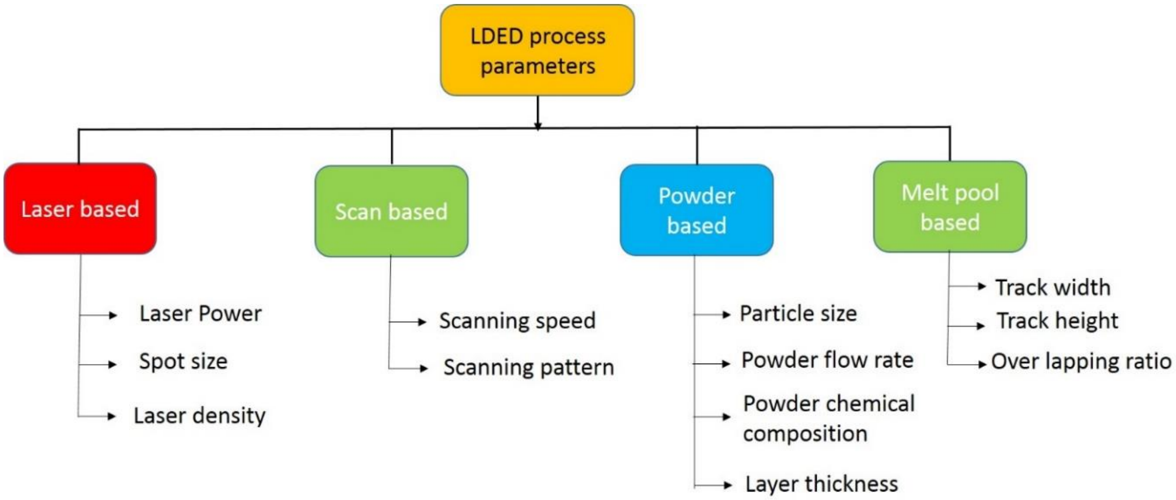

Figure 1.12 Process parameters of DED system

1.2.4.3 Process parameters involved in LAM process

Laser power is termed as the rate at which energy is generated from the laser. The mechanical properties of the final deposited part are determined by laser power supplied to the material. Discontinuous tracks are generated when laser power is insufficient for melting whereas extreme melting of the substrate and previously deposited layer when high laser power than the required for the given material. In the single-track deposition, deposition rate increases with material flow rate up to threshold value for a given laser density and interaction time. The cross-section of the track becomes circular and poor adhesion with the substrate when it reaches beyond the threshold value. Scanning speed can be defined as laser movement per unit time. The typical scan range for PBF and DED process is 1-10 m/s and 300-2000 mm/min respectively [4]. The laser energy per unit length, powder feed per unit length and interaction time are influenced by scanning speed variations as show in equation (1.1, 1.2 &1.3). The following equations are considered in single track analysis to optimize the process parameters for bulk deposition.

Laser energy per unit length $= \frac{P}{V}$ (1.1)

Powder feed per unit transverse length $= \frac{m}{V}$ (1.2)

Interaction time $= \frac{d}{V}$ (1.3)

Here, P is laser power, v is scanning speed, d is laser spot diameter and m is powder feed rate. The tracks are deposited adjacent to each other to create a single cross-section layer as shown in figure 1.13. The overlap ratio is calculated by equation 1.4. The optimum overlap ratio gives excellent mechanical properties, low porosity and good surface finish.

$$\text{Overlap ratio} = \frac{X}{w} \tag{1.4}$$

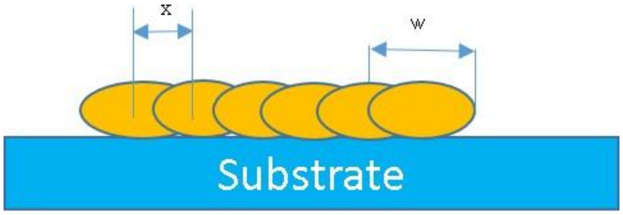

Figure 1.13 Schematic diagram of transverse section of single layer deposition

Here *x* is center distance of two adjacent tracks and *w* is track width. The laser path has a major effect on the mechanical properties of the component [4]. Therefore, the selection of scan strategy plays a major role during the process.

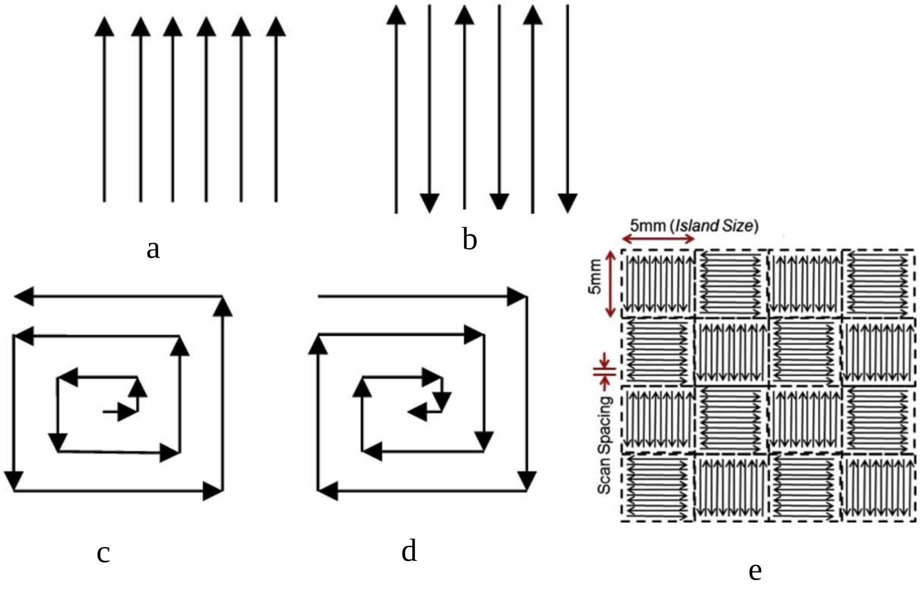

Figure 1.14 Different scanning strategies for LAM process a) Unidirectional b) Bidirectional c) inward to outward d) outward to inward e) island strategy [4]

Different scan strategies are used in PBF and DED processes for different materials. However, the scan strategy is limited for DED process due to restrictions in the feeding system (powder and wire feed). The uni and bi-directional strategies are generally employed for DED process as shown in Figure 1.14. The island strategy is generally selected in the LAM process due to the uniform heat distribution and minimize the residual stresses.

Hatch angle refers to the angle between laser scanning directions to consecutive layers as shown in Figure 1.15. For example, the angle between two consecutive layers is 45^0, which indicates 8^{th} layer is the same as the first layer. The change in properties are not significant with varying hatch angles is noticed in a previous study [34].

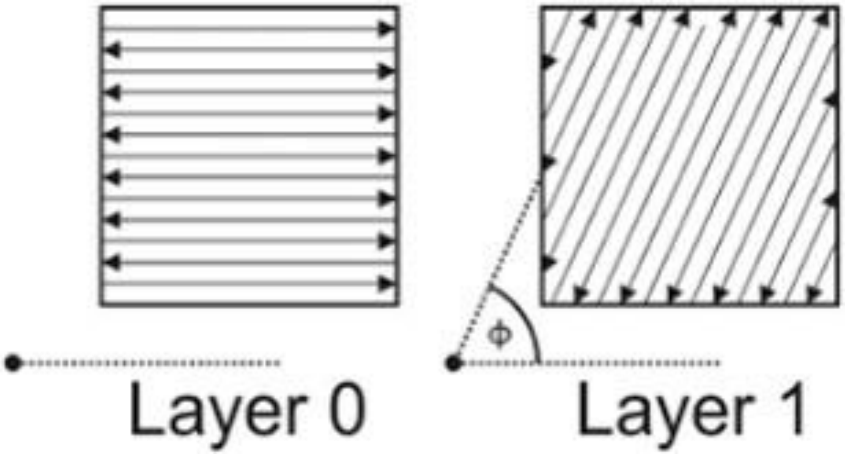

Figure 1.15 Schematic of hatch angle between two consecutive layers [34]

The change in mechanical properties is identified with a change in build direction as shown in Figure 1.16. The specimens built with 45^0 have higher ultimate tensile strength (UTS) and elongation as compared to samples built with 0^0 and 90^0. This indicates significant anisotropy of LAM parts. The average UTS for 0^0, 45^0 and 90^0 is 935.57 MPa, 963.50 MPa and 952.97 MPa, respectively [35].

Layer thickness has the most significant effect on the surface finish of the component. The improvement in the surface finish is achieved in Z- direction when reducing layer thickness of build part. The mechanical properties are not much affected by the change in layer thickness. The typical layer thickness range for PBF and DED process is 50-200 µm and 0.5 to 2 mm respectively [4].

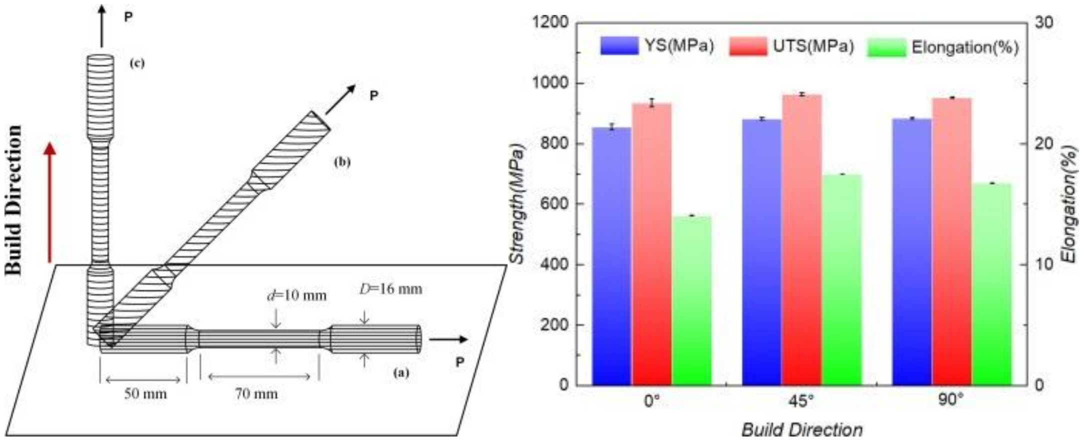

Figure 1.16 Variation of strength with respect to build direction [35]

The common defects are involved in the metal AM process: porosity, cracking, delamination, residual stresses, distortion and balling effect [1]. Therefore, the selection of optimum process parameters is much more important in the metal AM process. The type of defect and remedies for each defect is shown in Table 1.2.

Table 1.2: Typical defects involved in AM process [27]

Type of defect	**Reason**	**Remedies**
Porosity and lack of fusion	Entrapped gas, un-melted powder and insufficient over lap	Selection of optimum laser power and scanning speed, and hot iso-static pressing (HIP)
Delamination and cracking	Generation of residual stresses [20]	Heat treatment
Balling effect	Oxidation of molten pool, high scanning speed and low laser power resulting in low wettability	Optimized process parameters and controlled atmosphere
Stair case effect	High layer thickness and build direction for curved and inclined surfaces	Proper selection of process parameters and build direction

Feature size	Size of the energy source	Process parameters selection and machining
Loss of alloying elements	High laser density, larger surface to volume ratio	Selection of optimum laser power and scanning speed [4]

1.2.4.4 Post treatment of LAM process

The changes in geometry shape, residual stresses, and un-melted powder are major problems during the MAM process. To overcome the above-prescribed problems, post-treatment is required. Initially, the loose and un-sintered powder are removed from the built part and later the supports are extracted from the component using machining or a band saw. In PBF and DED process, the build part is extracted from the substrate or build plate using wire electrical discharge machining. The next step of post-processing depends on the applications. The surface finish can be improved by CNC milling, glass blasting, polishing and ultrasonic machining. The laser shot peening (LSP), laser annealing (LA) and laser machining (LM) techniques are successfully performed to improve the surface finish of the components. LAM components are subjected to tensile stresses on the surface due to rapid heating and cooling. The compressive stresses are induced in the component using LSP and also it improves the surface properties like wear and corrosion resistance. The improvement in hardness, wear and corrosion of LSP processed Inconel 718 are noticed by 27%, 77% and 70% respectively.

Post-heat treatment is carried out to relieve internal stresses due to high thermal gradients. In addition, it is used for altering grain size, grain orientation, porosity and mechanical properties of the component. Annealing is generally adopted to relieve internal stresses, and solution heat treatment followed by aging is typically opted for precipitation hardened materials. Dissolving the undesirable phases is achieved by solution heat treatment while aging helps in improving hardness by formation and growth of precipitation phases. The metal AM defects like porosity, voids and cracks inside the component are reduced by hot iso-static pressing (HIP) [4].

1.3 Motivation

Laser additive manufacturing (LAM) possesses higher processing speed and solidification velocity leading to high cooling rates (~ 10^5 K/s) [3]. This results in finer microstructure and better mechanical strength than as-cast samples. DED is one of the LAM processes, successfully used for processing a wide variety of materials like iron-based alloys, Nickel-based alloys, Cobalt- based alloys etc. for various engineering applications. However, DED can be an option for building near net shaped structures without any significant material losses.

Austenitic stainless steel (SS 316) is used in various engineering applications such as aerospace, energy, automotive, nuclear and marine sectors, due to its superior properties, like - high strength, corrosion fatigue resistance etc.[46] . Although SS 316 built components are fabricated through conventional manufacturing routes, the fabrication of complex shaped engineering components using conventional manufacturing process is costly. Therefore, DED process is adopted for fabricating SS 316 intricate parts with minimal cost. Although, it is used in numerous applications and it is restricted to few applications because of its low hardness and wear resistance [47].

Therefore, the parametric investigation is done based on the maximum hardness and deposition rate. The microstructure, micro hardness and tribology study are conducted for as deposited SS 316, heat-treated samples and its composites. In addition, studied the corrosion behaviour of SS 316 under different circumstances.

1.4 Organization of thesis

Chapter-1: Introduction

The importance of additive manufacturing and its application over conventional processes is discussed. In addition, the chapter focuses on metal additive manufacturing and its classification. The working principle and advantage of MAM-based processes such as binder jetting, selective laser sintering, laminated object manufacturing, powder bed fusion and directed energy deposition are discussed. The basic process parameters and post-processing involved in MAM process are explained.

Chapter-2: Literature review

Literature review attempts to give detailed information related to the microstructure and mechanical properties of SS 316 and SS 316L manufactured by PBF and DED. The effect of post-heat treatment and addition of ceramic particles in SS 316 & SS 316L on the microstructure and mechanical properties are also discussed. The numerical analysis on melt pool, single and multi-track behavior of DED built materials are also reviewed.

Chapter-3: Parametric investigations on Direct Energy Deposited (DED) Austenitic stainless steel 316 using experimental and finite element analysis

Parametric investigation of stainless steel 316 (SS 316) built by DED is performed. Single-track DED experiments are carried by varying laser power, scanning speed, and powder feed rate using full factorial experimental design. The effect of DED process parameters on the track geometry, deposition rate, and micro-hardness is investigated. In this current study, experimental and finite element analysis was carried out based on the track geometry at each process parameter during single track analysis. Apart from this, the size and morphology of microstructure at each process parameter are estimated by finding temperature gradient (G) and solidification rate (R) through finite element analysis.

Chapter-4: Characterization of Direct Energy Deposited SS 316 bulk samples

The microstructure characteristics (XRD, porosity and microstructure) and micro hardness of DED SS 316 bulk samples manufactured at different scanning speed are investigated. Tribology performance of SS 316 is studied under different values of normal load and sliding velocities at identified conditions.

Chapter-5: Effect of post heat treatment conditions on DED built SS 316.

Investigation on the effect of heat-treatment on the microstructure, mechanical, tribological and corrosion characteristics of DED built Stainless Steel (SS 316) bulk structures

Chapter-6: Characterization of DED built SS 316-WC composites at different volume fraction of WC

SS 316- tungsten carbide (WC) composites are built using DED by varying the WC weight fraction from 6% - 10%. Investigations on the relative density, microstructure, micro-hardness and tribological properties SS 316 composite are carried out at different volume fraction of WC.

Chapter-7: Conclusion and future scope

CHAPTER 2

LITERATURE REVIEW

2.1 Investigation on microstructure and mechanical properties of additive manufactured SS 316

Li et al. [48] investigated the effect of build direction on the tribological properties of stainless steel 316L built by L-PBF under different normal load, frequencies, and temperature. It was observed that the wear rate and coefficient of friction (COF) were not influenced by the build direction of the built samples. The increase in normal load causes the enhancement of wear, but no significant influence on the COF was observed as shown in figure 2.1. An increase in wear rate was observed with temperature, whereas a sudden decrease in wear loss is identified at high temperature owing to oxide layer formation. High thermal energy with a rise in frequency causes the material softening resulting in high material removal. Zhu et al. [49] investigated the tribological performance of stainless steel 316L using L-PBF under lubricated conditions. Two different counter material was deployed to investigate the tribological behaviour of L-PBF and conventional SS 316L built samples. In the case of soft counter material (brass), no significant effect on COF and wear rate was observed. In contrast, a significant difference in wear and COF of the L-PBF samples was identified when tested with the harder material (38CrMoAl). A low wear rate was observed for L-PBF samples than the tubular product steel parts owing to the fine

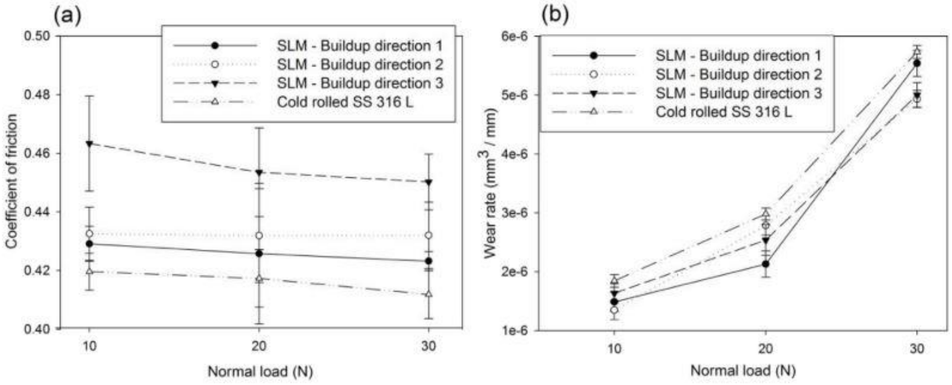

Fig. 5. Effect of build-up direction on COF and wear rate (room temperature, 4-Hz frequency).

Figure 2.1 Effect of build direction on (a) COF and (b) wear rate grain refinement and dislocation density of L-PBF. Li et al. [50] reported the effect of process parameters on the tribological performance of the stainless steel 316L using L-PBF. The small size pores and low hardness values were noticed at the low values of laser power as shown in figure 2.2.

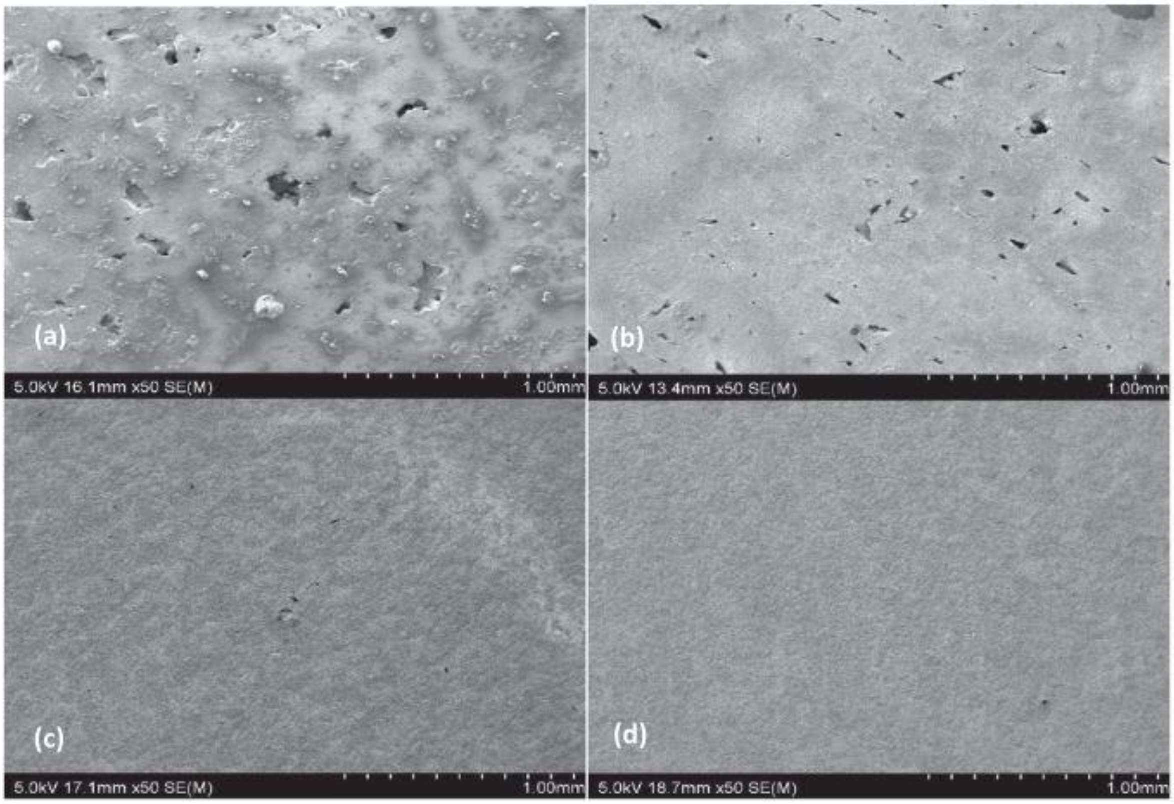

Figure 2.2 Porosity produced by different laser powers: (a) 100 W, (b) 150 W, (c) 200 W, and (d) 300 W

Further, it was noticed that the laser power and build direction were not significantly influencing COF and wear rate. Sun et al. [51] experimentally investigated the tribological properties and corrosion resistance of SS 316L built by L-PBF. The increase in the porosity with scanning speed and effect of volume of porosity on the wear resistance of L-PBF parts was also reported as shown in figure 2.3. It was observed that the wear rate of L-PBF SS 316L samples was 6 – 17 % higher than that of bulk SS 316L and it was attributed to the early fracture and crack initiation due to the presence of pores. J Chen et al. [52] investigated the influence of process parameters on the interfacial region of selective laser melting 316L/CuSn10. The defects like pores, cracks and protrusions are noticed at the interfacial region due to improper selection of volumetric energy input resulting in low ultimate tensile strength (UTS). The optimum US of 459.54 ±3.08 MPa with elongation of 5.23 ±0.65% was noticed at optimum process parameters. And also observed, the maximum nano hardness of 2.97 ±0.36 GPa at interfacial region due to fine grain structure. Yusuf et al. [53] studied the tribology behaviour of L-PBF SS 316L after the sample subjected to high-pressure torsion (HPT). The nano grain refinement (42 nm) is observed after 10 HPT revolutions as compared to as-built sample. The microhardness and wear resistance of SS 316L were improved by 172.7 % and 60% after 10 HPT process. Richard [54] performed the creep behaviour of SS 316L fabricated by L-PBF process under multi-axial loading conditions. The sample built-in horizontal direction was subjected to high creep rates (8 times) than the sample built-in vertical direction. It could be ascribed to columnar gains parallel to the build direction and presence of cracks. G. Sander et al. [55] studied the effect of residual stresses and build direction on corrosion behaviour of SS 316L manufactured by selective laser melting. The horizontal build part comprises of large grains, and vertical and 45^0 build samples are subjected to equiaxed grain. The corrosion resistance of SLM SS 316L was superior to wrought iron. The horizontal build part was subjected to high pitting corrosion resistance than the counterpart. And also noticed that the residual stresses in additively manufactured SS 316L was not significant effect on the pitting corrosion resistance. M Ahmed et al. [56] investigated the effect of spattered stainless steel

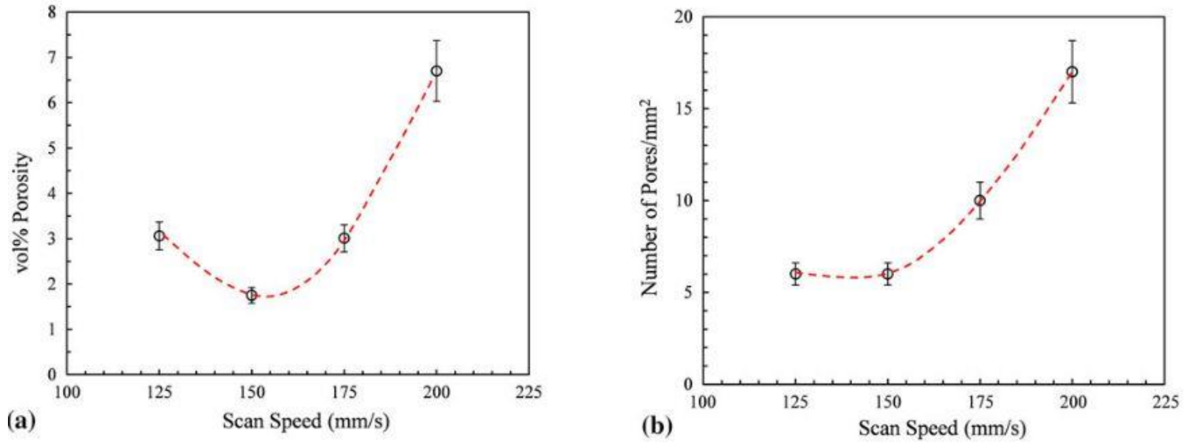

Figure 2.3 Image analysis results of the SLM samples showing (a) percent of porosity and (b) number density of pores per mm^2 area in the samples as a function of scan speed at 150 W

material during selective laser melting process. The gold colour and large irregularly shaped aggregates of SS 316L particles are identified due to chemical reaction with build chamber atmosphere during melting. From EDX analysis up to 100 nm from the surface, reductions in Fe and Ni, rise in oxygen content and Cr and Si content were observed. In addition, observed from XRD analysis, did not notice any variations in crystal structure/phase variations in bulk SS 316L particles. The optimized gas flow rate and laser power can reduce the spatters generation and consequently avoid the effect on the mechanical properties of the SS 316L build part. Y. Song et al. [57] studied the effect of different scanning strategy with rotation and without rotation on microstructure and mechanical properties of the SS 316L manufactured by selective laser melting. The scanning strategy of the sample with rotation consists of columnar growth epitaxially whereas samples without rotation between layers tend to break out columnar grains resulting in fine grain structure. The sample with 47^0 rotation showed high tensile strength and ductility as compared to the sample with 90^0 rotation. Additionally, microhardness of SS 316L samples with a rectangle pattern was better than the parts with hexagonal pattern. J. Ghorbani et al.[58] optimized the process parameters of laser surface re-melting process on selective laser melted inclined SS 316L parts. The layer thickness of 200 μm showed better results for remelted samples with small cracks and sigma phase. V. H. Dao et al. [59] studied the effect of build direction (vertical and horizontal) on creep behaviour of SS 316L fabricated by SLM. The cellular structure with a size of 500-700 nm was noticed for both directions. The creep deformation resistance and longer creep life were observed part with vertical build direction as compared to horizontal build direction. And also noticed, the creep life of SLM manufactured SS 316L was inferior to conventional manufactured part. The vertical and horizontal build parts were subjected to layer to layer melt pool boundary (MPB) and track to track melt pool boundary respectively. The layer to layer MPB had a higher bonding force than the track-track bonding force. Y. Sato et al. [60] investigated the effect of spatter generation during the processing of SS 316L using SLM process. The spatter formation was reduced by selecting optimum laser energy. The optimum laser fluence was found to be 20 kJ/cm2 where the minimum amount of spatter generation was identified. And also, identified that the surface finish of SS 316L was reduced from 30 μm to 3.5 μm. Y. G. Dursun et al. [61] investigated the effect of process parameters on surface characteristics of the selective laser melted SS 316L. The laser power was a most significant effect on the wider melt pool generation resulting in a good surface finish whereas cracks, pores and discontinuity on the surface of SS 316L observed with increased scanning speed. M. Laleh et al. [62] studied the effect of pores and lack of fusion inside the SS 316L manufactured by SLM process. The localized corrosion at the sites of pores and lack of fusion was identified due to lower breakdown potential. And also mention that the selection of optimized parameters are playing vital role to control the porosity effect. S. Afkhami [63] performed the static, cyclic and impact loads on SS 316L developed by SLM process. The performance of additively manufactured SS 316L under static, cyclic conditions was better than conventional methods. However, the sample under fatigue conditions required machining or mechanical post-processing. R.K. Upadhyay et al.[64] investigated the behavior of powder bed fusion of SS 316L during scratch and wear test at a different normal load of 1 N, 5 N and 10 N. The surface deformation was started when the load reached above 5 N while the scratch test. The wear rate of SS 316L was 1.2 x10^{-7} mm^3/N-m to 3.9 x10^{-7} mm^3/N-m when increasing normal load from 1 N to 10 N. The wear resistance of SS 316L is improved by 20.5 % as compared to the conventional method. J.K. Veetil et al. [65] investigated the dimensional deviation of SS 316L built by powder bed fusion process based on the build direction and inert gas flow rate. Samples were placed away from samples along with X direction resulting in high accuracy close to the nominal dimensions. The uniform flow rate and pressure inside the process chamber given better dimensional accuracy. And also identified that samples close to the window chamber side were attained with good circularity due to fast cooling rates. L. Chen et al. [66] investigated the effect of laser polishing on the mechanical properties of SS 316L sample manufactured by selective laser melting process. The grain size and surface roughness of the polished sample were reduced by 86.63 % and 23.2 % respectively. And also noticed that micro-hardness, tensile strength and ductility of laser polished SS 316L were enhanced as compared to as-built SS 316L sample . P. Deng et al. [67] studied the sources of oxygen inclusions in selective laser melted SS 316L sample. Stated that the powder making process like gas atomization process, spattered particles generation while building part, powder exposed to moisture and chemical elements in SS 316L like Si or Mn were major reasons for the formation of oxygen inclusions in SS 316L. P. Margerit et al. [68] investigated the effect of build direction on the tensile strength of SS 316 processed by PBF. The tensile strength of build direction (0^0, 45^0 and 90^0) of SS 316L was 419 MPa, 441 MPa and 431 MPa respectively. It might be due to lack of fusion and consequently, crack formation reason for the failure of built parts. Tolosa et al. [69] examined the mechanical properties of SS 316 using the LPBF process and obtained results were compared with wrought material. The high yield strength and micro-hardness were attained with LPBF compared to the wrought counterpart. Ma et al. [70] optimized the input process parameters for large-scale SS 316L parts with high mechanical properties. It was observed that the variational-orientation raster scanning pattern with high scanning speed and small laser spot size resulted in good dimension accuracy, and high ultimate strength and yield strength. Sun et al. [71] studied the corrosion and dry sliding wear behavior of SS 316L manufactured by the LPBF process. The wear rate of SS 316L built by LPBF was 16 times higher than the conventional SS 316L bulk samples due to the presence of porosity. It was also noticed that the corrosion rate of L-PBF samples was slightly higher due to pitting corrosion.

Weng et al. [72] studied the novel strategy for obtaining thin SS 316L rods using DED in Z-direction. Both austenite and ferrite phase were identified and the acquired phase further enhances the mechanical properties of SS 316L samples. In addition, high tensile strength and shrinkage rates were obtained at optimized parameters. Zhang et al. [73] examined the mechanical properties of stainless steel by DED at the optimum process parameter. Orthogonal experiments (L25_5_6) were carried out to optimize the DED process parameters considering the track width and height, and also developed an ideal overlapping model to build the samples without any defects. The planar zone and slender epitaxial dendritic microstructure were observed in DED samples and its mechanical properties were observed to be similar to conventional cold rolled SS 316 plate. It was also noticed that the scanning speed was the most significant parameter influencing the microstructure morphology and mechanical properties of DED samples rather than the laser power. Riza et al. [74] investigated the wear behavior under dry and severe conditions of high-strength steels such as SS 316L and H13 tool steel built by DED. The high COF values were obtained for DED samples when compared to commercially available grade steel. It could be ascribed to variation in the chemical composition of DED samples and severe test conditions. However, the specific wear rate of DED built sample was found to be similar to commercially available samples, mainly due to ~ 100 % density achieved through DED. Lei et al. [28] investigated the microstructure, micro-hardness and corrosion resistance of SS 316 by DED with Gaussian beam and ring-shaped beam. The transition from coarse to fine microstructure was attained with the rise in scanning speed and decreasing powder feed rate, but laser power was not significant in governing the microstructure of SS 316. The fine microstructure and high micro hardness values were obtained with a ring-shaped beam than the Gaussian beam. In addition, coarse microstructure and low corrosion resistance were noted with increasing overlapping ratio. Milton and Simon [75] studied the microstructure and mechanical properties of SS 316 stringers at different process parameters. In microstructure analysis, the epitaxial dendritic and cellular structure was identified in developed stringers. The maximum yield and flexural stresses were 261 MPa and 2388 MPa, respectively and these results were attained with laser power of 200W, scanning speed of 200 mm/min and an overlapping ratio of 33%. Guo et al.[76] investigated the microstructure and mechanical properties of DED SS 316L samples at two different build directions. The homogenous microstructure for 0^0 build direction sample and coarse dendritic structure for 90^0 build direction were noticed as shown in figure 2.4.

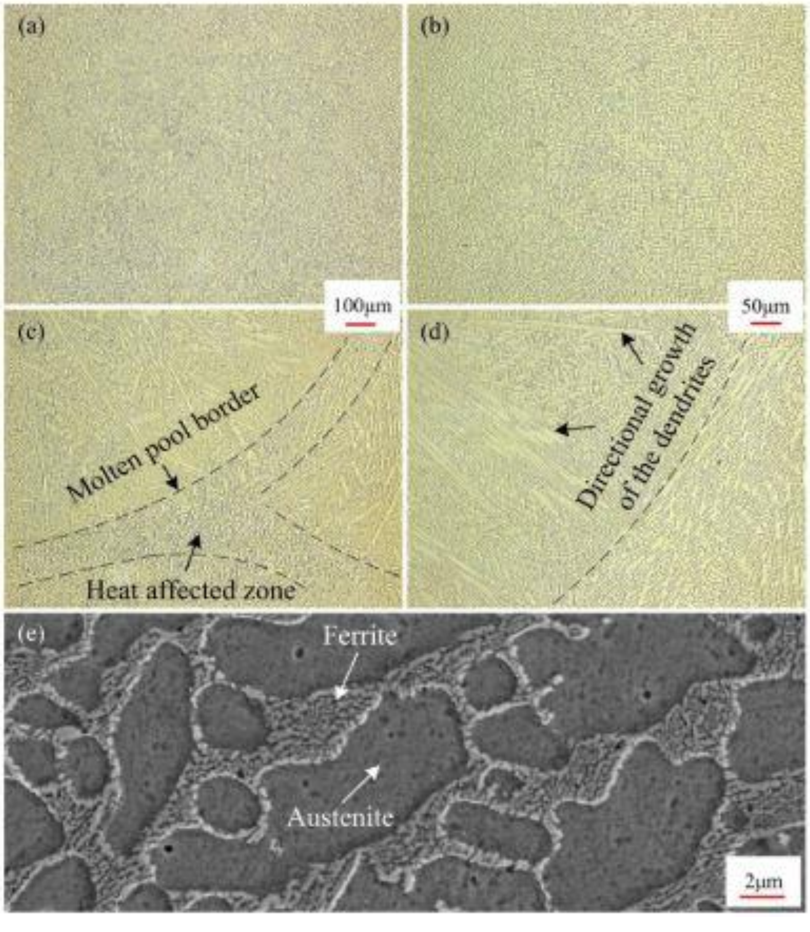

Figure 2.4 Micrographs of the additive manufactured stainless steels at various building directions, (a) and (b) the building direction of 0^0, (c) and (d) the building direction of 90^0, (e) enlarged view of the microstructure corresponding to (b).

The tensile strength, ultimate strength and elongation of build direction of 0^0 samples were better than the 90^0 and it can be attributed to the loading direction parallel to slicing direction of the built sample. Tan et al. [77] examined the microstructure, porosity and density of DED built SS 316 sample. The columnar microstructure was observed with a density of 99.8% and pore size in the range of 0 - 20.09 µm for as-deposited SS 316. Weng et al.[78] selected a novel strategy for thin rod fabrication in Z-direction using DED process. The dual-phase microstructure (austenite and ferrite) was observed with maximum tensile strength of 608.24 MPa and 65.08% shrinkage rate at a laser power of 45.2 W, scanning speed of 0.5 mm/s and powder feed rate of 2.81g/min. Majumdar et al. [79] optimized the process parameters based on the microstructural study on SS 316L using DED process. The equi-axed grain at top layer, medium columnar grain size at the interface of two successive layers and epitaxial fine grain at interface of substrate were observed. The micropores were reduced with low scanning speed and medium powder feed rate, whereas it increased with power density. Feenstral et al.[80] studied the effect of build height on the microstructure and corrosion resistance manufacture by DED. Fine equiaxed grains at bottom of the sample, large columnar grains with the zig-zag pattern at the middle of the sample and large columnar grains at top of the build sample were noticed. The sample built by DED SS 316 was subjected to higher pitting corrosion than the wrought iron, but lower than the sample built by using LPBF.

2.2 Investigation on microstructure and mechanical properties of heat treated SS 316

Researchers have investigated the effect of heat-treatment on the properties of MAM built stainless steel structures. Yadollahi et al [81]. investigated the effect of heat-treatment on the mechanical and microstructural properties of SS 316L built using DED. It was observed that the hardness of heat-treated samples was lower than that of the as-built samples primarily due to reduction in the ferrite (δ) phase. The increased grain size and isotropic structure were also observed after heat-treatment. Chen et al. [82] studied the microstructural and mechanical properties of heat-treated SS 316L samples fabricated by wire arc based DED. The identified phases in SS 316L were austenite (γ), sigma (σ) and delta ferrite (δ). It was observed that σ and δ phases were completely dissolved in austenite phase (γ) after heat-treatment and columnar grain structure changed to equiaxed grain structure, when solution treatment was carried out at 1473 K.

In addition, it was observed that high corrosion resistance was also achieved after heat-treatment as shown in figure 2.5.

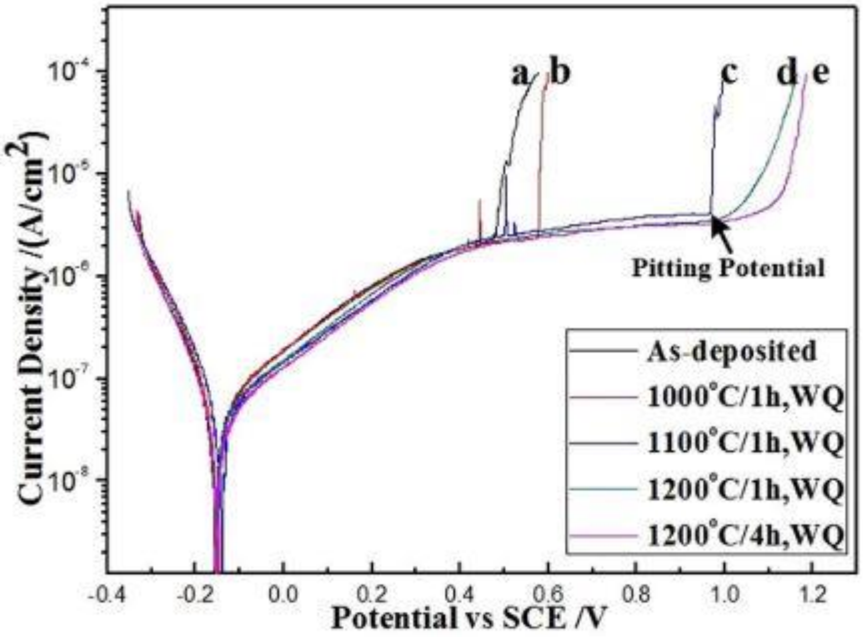

Figure 2.5 Potentiodynamic curves of as-deposited and heat treated GMA-AM 316L in 3.5% NaCl solution at 25 °C: (a) as-deposited, (b) 1000 °C/1 h, WQ, (c) 1100 °C/1 h, WQ, (d) 1200 °C/1 h, WQ, (e) 1200 °C/4 h, WQ.

Salman et al.[83] performed annealing at different temperatures (573, 873, 1273, 1373 and 1673 K) on SS 316L processed by LPBF for microstructure and mechanical properties analysis. It was reported that cellular structure was retained up to the temperature of 873 K and it disappeared after reaching temperature ≥ 1273 K. The increase in cell size and reduction in the strength and ductility of samples with heat-treatment temperature was observed as compared to as-built SS 316L samples. Kong et al.[84] investigated the mechanical properties of SS 316L fabricated by LPBF after heat-treatment at two different temperatures 1323 K and 1473 K. The reduction in microhardness from 280 HV to 200 HV was observed after heat-treatment at the temperature of 1323 K and it was attributed to an increase in dislocation density and grain size with heat-treatment as shown in figure 2.6.

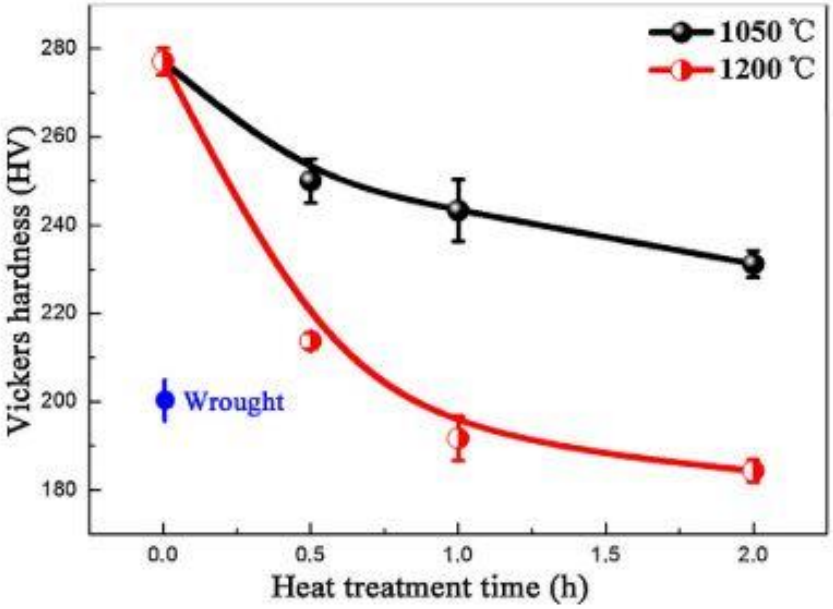

Figure 2.6 Relationship of micro-hardness and heat treatment time for SLMed 316 L stainless steel at 1050^{0}C and 1200^{0}C

Chena et al. [46] studied the effect of heat-treatment on the mechanical properties of LPBF built SS 316L structures at two different annealing temperature: 673 K and 1073 K. The results indicated that a high hardness value of 291 HV and enhanced yield strength by 10% were attained after heat-treatment at 673 K. This was attributed to high dislocation density and nano silicon precipitates. In addition, increment in cell size, reduction in dislocation density and hardness, and absence of precipitates were also observed when annealed at 1073 K. Tascioglu et al.[85] studied the effect of heat treatment temperature on microstructure, mechanical and wear properties of SS 316L manufactured by LPBF process. The cellular and band structure for as built sample and its disappearance after heat treatment at 1100^{0}C for 2 hours followed by furnace cooling were observed. In addition, it was observed that the micro- hardness was reduced by 27% as shown in figure 2.7.Porosity and Full width at half maximum (FWHM) from XRD analysis were reduced by 81.4% and 8%, respectively. However, a decrease in wear rate was noticed after heat treatment due to low porosity.

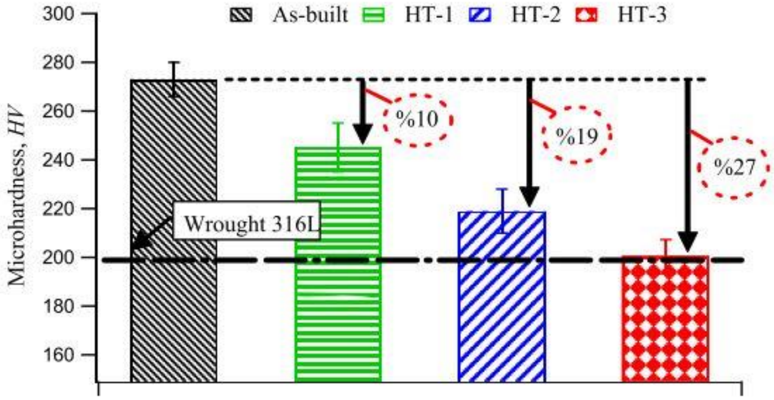

Figure 2.7 Micro hardness of SLM as- built and heat-treated specimens

Kamariah et al. [86] investigated the microstructure and micro-hardness of SS 316L processed by LPBF after heat treatment. As built SS 316L with cellular structure consists of austenite and ferrite phase was observed, but cellular boundaries disappeared after heat treatment due to ferrite phase reduction. The hardness of SS 316L was reduced by 19.34 % after heat treatment at 1100^{0}C for 2 hours followed by furnace cooling. Saeidi et al. [87] performed the heat treatment analysis to understand the microstructure characteristics and micro hardness of SS 316L fabricated by LPBF process. As deposited SS 316L consists of austenite and a small amount of ferrite phases, and microstructure comprising of sub-micron cells with dislocation were noticed. The disappearance of submicron cells as well as ferrite phase was noticed when heat treatment temperature reaches above 900^{0}C. The yield stress, tensile strength, micro hardness of as laser melted SS 316L were reduced by 8.11%,4.12% and 41.5%, respectively as compared to that of heat-treated SS 316L at 1100^{0}C. Saeidi et al. [88] studied the microstructure characterization of SS 316L manufactured by LPBF. The austenite phase and columnar sub grain microstructure was noticed for as-built SS 16L samples. It was observed that the sub grain boundaries in microstructure enriched with Molybdenum including high dislocation concentration. Kong et al. [89] investigated the microstructure and corrosion behavior of post heat-treated SS 316L processed by LPBF process. A significant increase in grain size was observed when the heat treatment temperature reached above 1050^{0}C. The microstructure of SS 316L consists of sub grains with dislocations in the as-built condition, which disappeared after heat treatment. The corrosion resistance of heat-treated samples was more than as deposited SS 316L due to low porosity in heat treated samples. Laleh et al. [90] studied the effect of post heat treatment process on the pitting corrosion resistance of SS 316L built by LPBF process. The high pitting corrosion resistance was noticed for LPBF samples as compared to wrought iron up to post heat treatment temperature 1000^0C. A drastic decline in pitting corrosion of SS 316L samples was observed above 1000^0C due to magnesium silicate inclusions transformed to manganese chromite.

2.3 Investigation on microstructure and mechanical properties of DED SS 316 based composites

Literature indicates that a considerable amount of work is being carried out globally to develop composites using DED. Wu et al. [91] studied the microstructure and corrosion resistance of DED built SS 316L-SiC based composite at different SiC fractions ranging from 4 - 16 %. The fine grain structure with γ-(FeCrNi) and α- (FeCrNi) phases were observed. An improvement in hardness by 169% primarily due to solid solution strengthening and high dislocation density was observed. Composites with 12 and 16% SiC showed lower corrosion resistance as compared to composites with 4 and 8% of SiC due to the high content of SiC and the formation of iron silicides. Farayibi et al. [92] investigated microstructure evolution and hardness behaviour of DED built TiAl4V - TiB_2 composites using satellited TiB_2 powder particles. The deployment of satellite powder leads to enhancement in microstructure homogeneity and uniform distribution of TiB_2 elements in Ti matrix as compared to the simple powder mix process. The hardness of 440-480 HV was observed in the deposited composite due to the presence of TiB_2 reinforcement. The wear and corrosion performance of laser deposited SS 304 reinforced with Al_2O_3 particles at 10% volume fraction was performed by Xu et al [93]. The micro-hardness and wear resistance enhanced by 200% and 80.3%, respectively owing to grain refinement and martensite formation. In contrast, better corrosion resistance was obtained with SS 304 coating than the composite coating. Paul et al. [94] investigated the erosion behaviour of Nickel-based composite involving a different fraction of tungsten carbide particles using the Taguchi method. It was observed that the erosion behaviour was more influenced by particle jet velocity followed by the impact angle. Dissociation/partial melting/full melting of WC particles was not detected in the built layers. The microhardness of the deposition zone was observed to range from 900–2400 VHN as opposed to 230–270 VHN on the substrate. Gorunov [95] investigated the microstructure, micro hardness and wear behavior of carbon fiber reinforced SS 316L and Inconel 718 (Inconel 718/carbon fibre/ SS

316L) composites developed by DED. It was observed that the carbon disintegrates from carbon fiber and interacts with Cr resulting in chromium carbide formation ($Cr_{23}C_6$ and Cr_7C_3)and the hardness increased by 2 times as compared to SS 316L and 1.5 times as compared to Inconel718. It was seen that the average wear volume of Inconel 718/carbon fibre/ SS 316L composite is lower than DED built Inconel 718, which shows that the wear resistance of the deposited composite is higher than Inconel 718 and provides better service at higher load when paired with steel-based materials. The influence of laser energy per unit length on the microstructure, micro hardness and wear behaviour of TiC/Inconel 718 composites built using DED was investigated by Sainan and Dongdong [96]. Well distributed TiC particles were identified in the energy range of 100-160 kJ/m, whereas the little amount of micro pores were noticed at low energy 80 kJ/m. The high hardness and wear resistance were noticed at high laser energy per unit length (160 KJ/m) due to large interface layer with carbide formation ((Ti,M)C (M=Nb and Mo)) between matrix and TiC particles, and fine microstructure. The microstructure evaluation, presence of phases and micro-hardness of metal matrix composite was studied by Shishkovsky et al. [97] using binary and ternary intermetallic structure through DED. The system consists of Ti-Al, NiCr-Al and NiTi-Al alloys in which different binary and terinary intermetallic structures were identified. From the results, the highest hardness was 1000 HV obtained with NiTi-Al alloys because of Nix(Al,Ti). Ramakrishnan and Dinda [98] investigated the microstructure of DED built 82 wt % Al and 18 wt % W (82Al-18W) aluminum matrix composites at a different scanning speeds of 1.5 mm/s, 6 mm/s and 12 mm/s. At a scanning speed of 12 mm/s, fine microstructure with varying sizes of Al-W intermetallic phases especially at the interface of W particles and grain boundaries were identified. In addition, it was noticed that the developed Al-W composite showed more strength than the pure aluminium. Betts et al. [99] developed SS 316 based composites using DED and the performance of composites was evaluated by wear and corrosion test. The performance of the composite was poor at higher laser power due to the melting of Al_2O_3. The wear resistance of austenitic stainless steel increased with tungsten carbide addition. However, corrosion resistance reduced with WC addition because of chromium depletion as a result of chromium carbide formation during solidification. Li et al. [100] studied the microstructure, tensile and wear performance of Aluminum metal matrix composite (AMC) fabricated by DED process. In microstructure analysis, coarse $Al_{13}Fe_4$ laths and fine $Al_{13}Fe_4$ particles were identified. The samples were extracted from a different region of composites for evaluating ultimate strength, ductility and hardness, and results showed that the ultimate strength remains the same at every region, whereas ductility at the top region (3.8%) is higher than bottom region (1.1%). The maximum hardness of 84.12 HV was noticed at the bottom region and also wear resistance offered by AMC was higher than the wear resistance offered by conventional cast Al-12Si alloy. Huang et al. [101] studied the effect of scanning speed (low speed (50-100 mm/min) and high speed (700-900 mm/min)) on the microstructure and mechanical properties of alumina/aluminum titanate composites manufactured by DED process. The minimum cracks and pores were identified at the optimum scanning speed range (300-500 mm/min). The identified phases were α-Al_2O_3 and $Al_6Ti_2O_{13}$ in microstructure and also noticed secondary dendrite of Al_2O_3 at high scanning speed. The increase in fracture toughness was noticed with an increased scanning speed due to grain refinement, whereas flexural strength was reduced with scanning speed due to porosity. Liu et al. [102] investigated the effect of laser energy density on relative density, microstructure analysis and mechanical properties of 5 Wt.% TiC/AISI420 stainless steel composites. The relative density of composite is reduced at low laser energy density due to insufficient energy resulting in pores and cracks formation. The fine microstructure and uniform distribution of TiC particles were observed along the grain boundaries with an increase in the laser energy density. The ultimate strength, ductility and micro- hardness of composite were 1452.5MPa, 8.65% and 592.2±53.6HV, respectively at a laser energy density of 85.6 J/mm^3.

Ajay et al. [103] evaluated the microstructure and mechanical properties of graphene reinforced SS 316L composite manufactured by selective laser melting. In microstructure study, elongated and randomly oriented grains in build direction were observed and it might have ascribed to large thermal gradients. The hardness and yield strength of 0.2% graphene reinforced SS 316L are increased by 25% and 70% when compared with casted and hot pressed SS 316L sample. ShifengWen et al. [104] tailored the microstructure and mechanical properties of reduced graphene oxide (RGO)/S136 metal matrix composite prepared by LPBF. The reduced average grain size of 0.75µm was noticed at 0.1 Wt% of RGO and also noticed that the cellular dendritic grains transition to fine equiaxed grain with increasing RGO content. The maximum hardness, yield strength and tensile strength of 580.6 ± 15.4 HV, 515.8 ± 15.3 MPa and 535.3 ± 18.5 MPa were noticed respectively at 0.1% RGO content in S136 powder due to grain refinement, stress transfer and high dislocation strengthening. O.O. Salman et al. [105] studied the effect of TiB_2 particles in SS 316L matrix on microstructure and mechanical properties fabricated by LPBF. The cellular structure with sub grains, TiB_2 circular precipitates along the grain boundaries and reduction in cell and grain size were noticed in microstructure analysis. The yield strength of composite at 2.5 and 5% of TiB_2 is increased by 46% and 105% when compared with unreinforced SS 316L samples. Y. Han et al. [106] studied the microstructure and mechanical properties of the SS 316L reinforced with 0.1 wt.% single-layer graphene nanoplatelets (GNPs) manufactured by selective laser melting process. The high-density distribution of GNPs in the composite are noticed at grain boundaries resulting in fine grain structure. The ultimate strength of the composite was improved by 17.9 % without disturbing the ductility of SS 316L. W Zhai et al. [107] studied the mechanical properties of SS 316L by the addition of 1% TiC and 3% TiC processed by selective laser melting. The grain size of 3% TiC is reduced by 78% as compared to as build condition. The yield strength, ultimate strength and elongation of SS 316L composite (3% TiC) is improved by 40%, 36% and 46% respectively as compared to as-built condition as shown in figure 2.8. It might be attributed to the grain refinement and excellent wettability of TiC particles.

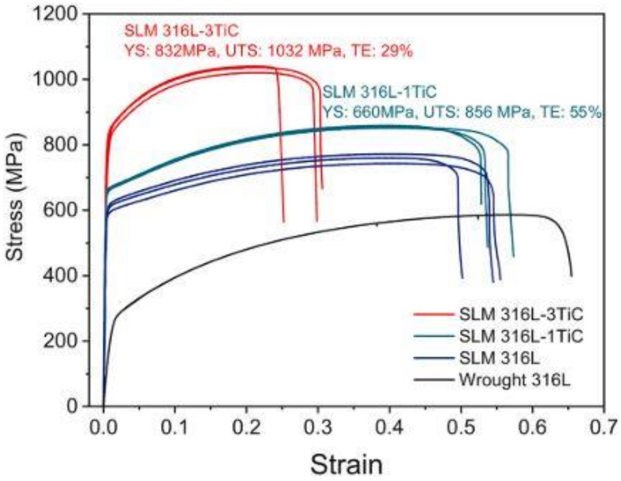

Figure 2.8 Tensile strain-stress curves of SLM-316L, 316L-1TiC and 316L-3TiC

2.4 Effect of process parameters on track geometry and thermal aspects involved in DED process

Chang Li et al. [108] validate the experimental with numerical simulation by cladding Fe60 on ASTM 1045 substrate and noticed that the close agreement between the two results. Besides, observed that 5%, 50%, and 45 % account for planar, thick dendritic and equiaxed crystals respectively were noticed during microstructure analysis. Wei Yaa et al. [109] investigated the track geometry and thermal cycles during single and multi-track deposition and also compared with simulation results. The prediction error between experimental and simulation was 5%. Simon Morville et al. [110] reported the fluid flow and heat transfer analysis during multi-track analysis. The impact of layer thickness, melt pool size and dilution on the surface finish was studied. It is observed that the increase in melt pool size and dilution are given high surface finish whereas reduction in layer thickness showed the improvement in surface finish. In addition, behaviour of melt pool and the effect of surface tension on melt pool size was also considered during multi-track analysis. The three-dimensional heat transfer analysis of DED was investigated by V. Neela and A. De. [111]. The thermal variations in the melt pool were studied during multi-layer deposition. Further added that non-dimensional specific heat energy was optimized to obtain a steady melt pool resulting which improve interlayer bonding. The 3D heat transfer model was developed by Alireza Fathi et al. [112] to forecast the melt pool behaviour, track geometry and dilution ratio, and also compared the model with experimental results. The dilution was increased nonlinearly with scanning speed whereas the increase in dilution and melt pool depth with laser power was observed. Shaoyi Wen et al. [113] reported the 3D transient analysis for laser direct deposition of SS 316L. In this study, a comparative study on simulation and experimental was done about track width and height, and temperature distribution with in the process. From the results, the maximum velocity and temperature in the melt pool were found to be 0.03 m/s and 2300 K, and obtained results well agree with experimental results. P Peyre et al. [114] studied an analytical and numerical model for DED in which powder temperature was estimated by the analytical model. In addition, temperature distribution and surface morphology of wall geometry with 25 layers was analysed and also compared with experimental data is obtained from the thermocouple and fast camera melt pool. Ehsan Toyserkani et al. [115] did the comparative study between simulation and experimental results with regard to track dimensions like width and height by changing laser pulse shape. In addition, found that close relation was noticed between simulation and experimental results. A. Baumard et al. [116] done the numerical analysis on grain structure formation of SS 316L manufactured by SLM process. The grain size was reduced with decreasing laser power at constant speed, or by increasing scanning speed. And also noted that the developed thermal model was validated for considering the effect of process parameters on the grain structure in SS 316L parts. Tian et al. [117] were performed the numerical analysis on single track deposition of SS 316L using SLM process. The different single-track morphologies were identified with the same linear energy density. The single track defects such as balling, porosity and distortion were noticed from simulation. The unsteady behaviour of melt pool, insufficient laser energy and Marangoni effect were main reason for porosity, balling and distortion effect respectively. The literature review of DED built SS 316, after heat treatment, and its composites is summarised in table 2.1.

Table 2.1 Literature summary of DED built SS 316 and SS 316 L, after heat treatment and its composites

SS 316 and SS 316 L are manufactured by DED and PBF processes			
Author	**Year**	**Process parameters**	**Findings**
S. Afkhami [63]	2021	Not available	Hardness, fatigue and tensile strength
J Chen et al. [52]	2020	Laser power of 200 W, scanning speed of 1200 mm/s, layer thick ness of 0.03 mm, and scanning space of 0.07 mm	Tensile strength and hardness
Yusuf et al. [53]	2020	Laser power of 200 W, scanning speed of 1600 mm/s, layer thick ness of 0.03 mm and island strategy	Microstructural study, micro-hardness and wear rate
Richard [54]	2020	Laser power of 200 W, exposure time 80 µs, layer thick ness of 0.05 mm and hatch spacing of 110 µm	creep rate
G. Sander et al.[55]	2020	Laser power of 205 W, scanning speed of 960 mm/s, layer thick ness of 0.04 mm and hatch spacing of 110 µm	Corrosion study
M Ahmed et al. [56]	2020	Volumetric energy density 89 J/mm^3	Comprehensive assessment of spattered material
Y. Song et al.[57]	2020	Laser spot diameter of 80 µm, wave length of 1070 µm, and ayer thick ness of 0.03 mm	Microstructural study, hardness and tensile strength
V. H. Dao et al. [59]	2020	Laser power of 275 W, spot size of 115 µm, scanning speed of 700 mm/s, layer thickness of 50 µm and hatching distance of 0.12 mm	Creep and tensile strength
Y. Sato et al. [60]	2020	Laser power of 150- 200 W, laser beam diameter of 100 µm, layer thick ness of 0.05 mm and hatch spacing of 25 µm	Spatter effect on developed material

M. Laleh et al.[62]	2020	Laser power of 125- 175 W a nd scanning speed of 400-800 mm/s	Corrosion
R.K. Upadhyay et al.[64]	2020	Wave length of 1070 nm, focus diameter of 50 µm and layer thick ness of 25 µm	wear
P. Margerit et al.[68]	2020	Laser power of 245 W, laser beam diameter of 0.338 mm, scanning speed of 33 mm/s, layer spacing of 0.2 mm and powder flow rate 6 g/s	Tensile and ductile fracture
Feenstral et al.[80]	2020	Not available	Microstructural study, hardness and corrosion
Weng et al. [72]	2019	Laser power of 34.3 and 45.2 W, scanning speed of 0.4,0.5 and 0.6 mm/s, and powder flow rate of 2.46,2.81 and 3.09 g/min	Microstructural study and tensile strength
Lei et al. [28]	2019	Laser power of 500-1000 W, scanning speed of 4-12 mm/s, powder flow rate of 1.6-2.8 rpm and overlap ratio 30-50 %	Microstructural study, hardness and corrosion
Tan et al.[77]	2019	Laser power of 1.4 KW, scanning speed of 1000 mm/min, powder flow rate of 14 g/min and overlap ratio 60 %	Microstructural study porosity, density analysis and micro-hardness
Li et al. [50]	2018	Not available	Wear rate and coefficient of friction
Guo et al.[76]	2017	Laser power of 2 KW, scanning speed of 125-200 mm/s, spot diameter of 5 mm, layer thick ness of 1 mm and hatch spacing of 3 mm	
Zhu et al. [49]	2016	Laser power 200 W, scanning speed 700 mm/s and layer thickness 30 μm	Wear rate
Riza et al. [74]	2016	Laser power of 500 W, scanning speed of 60-80 mm/min and powder flow rate of 2.5-3 g/min	Wear
Zhang et al. [73]	2014	Laser power of 600-1400 W, scanning speed of 2-10 mm/s and powder flow rate of 4-20 g/min	Microstructural study, hardness and tensile strength
Sun et al. [51]	2014	Laser power of 150- 200 W, scanning speed of 125-200 mm/s, laser beam diameter of 35 µm, layer thick ness of 0.05 mm and hatch spacing of 90 µm	Wear and corrosion

Milton and Simon [75]	2014	Laser power of 200- 350 W, scanning speed of 200-500 mm/min and overlapping ratio of 33%	Microstructural study and tensile strength
Ma et al.[70]	2013	Laser power of 600-1650 W, scanning speed of 400-1400 mm/min and powder flow rate of 9.8-29.24 g/min	Relative density, micro-hardness and tensile strength
Sun et al.[71]	2013	Not available	Wear test
Tolosa et al.[69]	2010	Laser beam diameter of 80-300 µm, scanning speed of 1000 mm/s, layer thickness of 30-100 µm and powder flow rate 6 g/s	Micro-hardness and tensile strength
Effect of heat treatment on SS 316 and SS 316 L is manufactured by DED and PBF processes			
Tascioglu et al.[85]	2020	Laser power of 200 W, layer thickness of 50 µm and hatch distance of 110 µm, exposure time of 80 µs and hatch pattern strategy	Microstructural study porosity, micro-hardness and wear
Laleh et al.[90]	2020	Laser power of 175 W, scanning speed of 400 mm/s, hatch spacing of 100 µm and layer thickness of 30 µm	Corrosion
Salman et al.[83]	2019	Laser power of 175 W, scanning speed of 688 mm/s, hatch spacing of 120 µm and layer thickness of 30 µm	Microstructural study
Kong et al.[84]	2019	Not available	Microstructure evolution
Chena et al.[46]	2019	Not available	Microstructure evolution
Kong et al. [89]	2018	Laser power of 195 W, scanning speed of 1083 mm/s, hatch spacing of 25 µm and layer thickness of 25 µm	Microstructure evolution and corrosion
Kamariah et al.[86]	2017	Laser power of 200 W, scanning speed of 800 mm/min and layer thickness of 30 µm	Microstructure evolution, hardness and tensile strength
Yadollahi et al.[81]	2015	Laser power of 360 W, scanning speed of 8.5 mm/s, hatch spacing of 0.5 mm, and layer thickness of 0.5 mm	Microstructure evolution, hardness and tensile strength
Saeidi et al.[87]	2015	Laser power of 195 W, scanning speed of 800 mm/s, hatch	Microstructure evolution, hardness and tensile strength

		spacing of 0.1 mm and layer thickness of 0.02 mm	
SS 316 and SS 316 L based composites are manufactured by DED and PBF processes			
Ajay Mandal et al. [103]	2020	Laser power of 320 W, layer thickness of 30 µm, hatch distance of 120 µm and exposure time of 100 µs	Microstructural study porosity, density analysis, micro-hardness and tensile strength
W Zhai et al.[107]	2020	laser power of 200 and 225 W, scanning speed of 800 mm/s, Layer thickness of 30 µm, Hatch distance of 70 µm,	Microstructure evolution and tensile strength
Wu et al.[91]	2019	Laser power of 2000 W, laser spot diameter 5 mm, scanning speed of 8 mm/s, powder flow rate of 11 g/min, overlap ratio 40 %	Microstructure evolution, hardness and corrosion
O.O. Salman et al.[105]	2019	Laser power of 175 W, scanning speed of 688 mm/s, layer thickness of 30 µm, hatch distance of 120 µm and hatch rotation 79°	Microstructure evolution and compressive strength
FEA analysis of DED built SS 316 and SS 316 L			
A. Baumard et al.[116]	2021	Laser power of 320 and 400 W, and scanning speed of 310 and 400 mm/s	Prediction of grain structure
Tian et al.[117]	2020	Laser power of 15-600 W, scanning speed of 50-1300 mm/s, layer thickness of 50 µm and powder bed packing density of 0.37	Morphology and thermal behavior of single melt track
Chang Li et al.[108]	2019	Laser power of 900 W, laser spot diameter 6 mm, scanning speed of 1.8 mm/s and powder flow rate of 6.2 g/min.	Temperature field, velocity field and solidification behaviour
Wei Yaa et al.[109]	2016	Laser power of 800-3600 W, laser spot diameter of 6 mm, scanning speed of 5-20 mm/s, powder flow rate of 0.05-0.5 g/s.	Powder efficiency, single track analysis and temperature field
Shaoyi Wen et.al [113]	2012	Laser power of 300 W, beam spot of 0.5 mm, scanning speed of 12.7 mm/s, and powder flow rate of 7 g/min	Track width and height analysis

Simon Morville et al.[110]	2010	Laser power of 320 to 500 W, laser beam radius of 0.65 mm, scanning speed of 0.1-0.4 m/min and powder flow rate of 1-2 g/min	Single track analysis, dilution ratio and multilayer deposition analysis

2.5 Research gaps

It is observed from the literature that most of the studies are concentrated on LAM of SS 316L. However, there is only very limited study on LAM of SS 316 concentrating on the microstructural and mechanical properties. Thus, in the present work an attempt is made to perform parametric investigation and also compared with finite element analysis results. The derive process parametric combination for maximum deposition rate and hardness, and deploying the above parameters to investigate the tribological behavior of DED built SS 316. The effect of varying process parameters of DED on track geometry and also temperature gradients has not been studied.

It is also observed that the published literature mainly concentrates on the effect of heat-treatment on microstructure and mechanical properties of SS 316L fabricated by LAM, whereas limited study is carried out on SS 316 built using LPBF and DED. Moreover, to the best of the author’s information, there is no literature available on the effect of heat-treatment on corrosion and tribological behavior of stainless steel structures built by LAM. In one of our previous works, parametric investigation was carried out for fabricating bulk SS 316 structures using DED. The samples were characterized using microstructure, mechanical and tribological tests. Microstructure was primarily columnar dendritic in nature with micro-hardness higher than conventional SS 316 samples. Thus, in the present study a comprehensive investigation is carried out to investigate the effect of heat-treatment on the microstructure, mechanical, corrosion and tribological behavior of DED built SS 316 bulk structures.

It was observed from the literature that high-density composites can be successfully built using DED process by introducing ceramic particles such as SiC, carbon fiber, WC, TiC, and Al_2O_3 in metallic alloys by using single and multilayer deposition. Also, a significant improvement in hardness, wear and erosion resistance is noticed by incorporating ceramic particles. Among the different reinforcement materials, WC is selected as a reinforcement material due to its exceptional properties, like - excellent metallurgical bonding with Fe alloy, ability to retain its hardness up to

1400°C and higher melting point [118] and WC based composites are widely used in gas, oil, and petrochemical industries. It is observed that limited literature is available in public platforms on the development of SS 316 – WC based composites using DED process. Therefore, in the present study the microstructure, micro-hardness, wear and corrosion behaviour of DED built SS 316 based composite is investigated using a different fraction of tungsten carbide.

2.6 Research objectives

1. Process parametric investigations on Directed energy deposited (DED) austenitic stainless steel 316 using experimental and finite element analysis.
2. Characterization of DED SS 316 bulk samples.
3. Effect of post heat treatment conditions on DED built SS 316.
4. Characterization of DED built SS 316-WC composites at different volume fraction of WC.

2.7 Research Plan

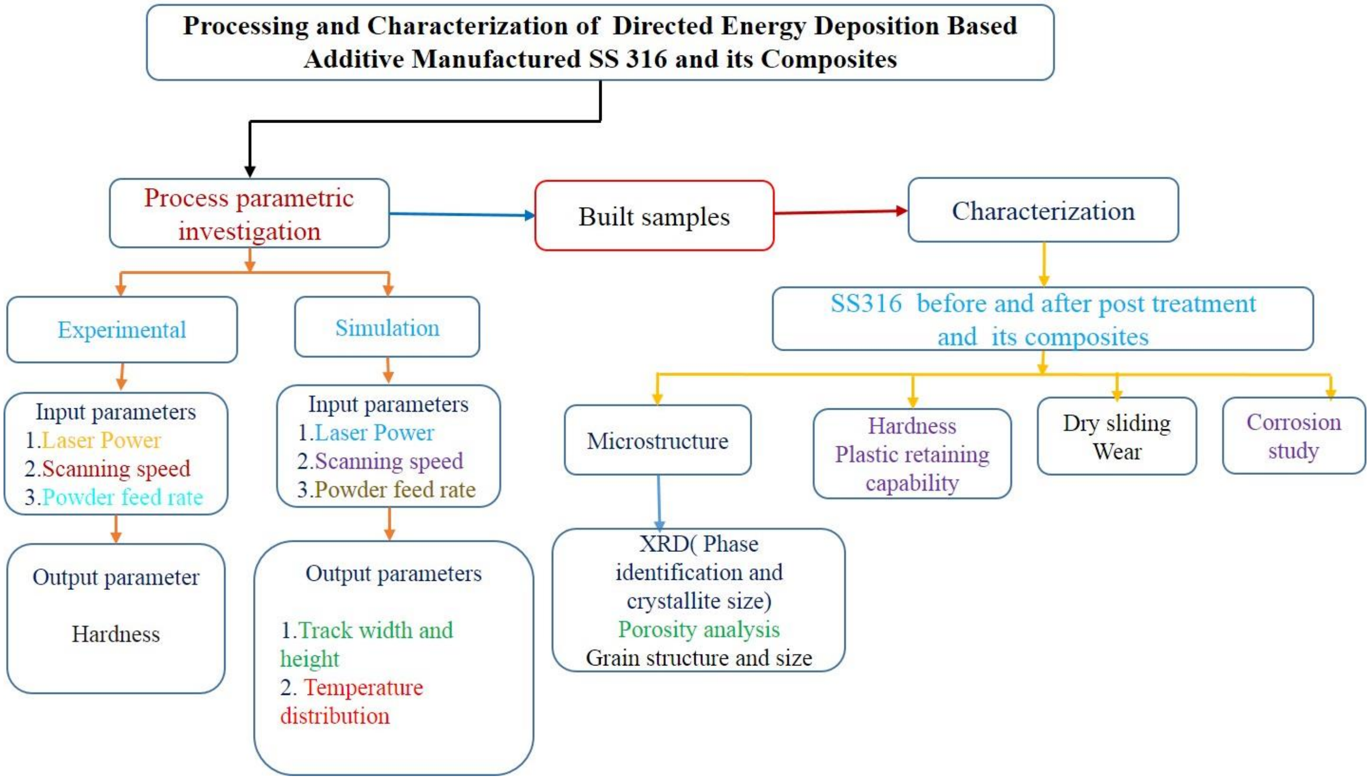

Fig. 2.9 Work plan

CHAPTER 3

MATERIALS AND METHODS

3.1 Materials

Gas atomized austenitic SS 316 powder particles of size in the range of 45 – 105 µm procured from Powder Alloy Corporation, USA is used for building samples using DED. Figure 3.1 and 3.2 (a) presents the morphology of SS 316 powder used for DED and its powder size distribution. Powders are typically spherical in nature with satellite particles attached to them. Table 3.1 presents the chemical composition of SS 316 powder deployed for deposition. Sandblasted SS 316L substrate with dimensions of 75 mm diameter and 10 mm thickness is used for DED experiments.

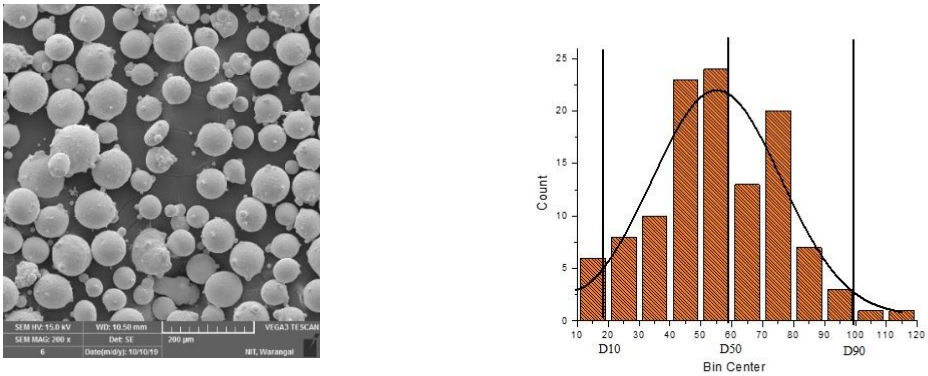

(a) (b)

Figure 3.1 SS 316 powder used for DED (a) SEM image of powder morphology (b) Powder size distribution

Table 3.1: Chemical composition of SS 316 powder

Elements	**C**	**Cr**	**Si**	**Mo**	**S**	**Ni**	**Fe**
Weight (%)	0.08	17	1	2.5	0.035	12	Bal.

SS 316L is used as the substrate material in sandblasted conditions to improve laser absorption. Prior to experiments, the substrate is cleaned with acetone to remove the impurities on the substrate surface. WC powder with the particle size of 45-106 μm is used as the reinforcement material in SS 316 based composites. Figure 3.2 (b) presents the typical morphology of WC powders used for deposition. The powders are well mixed using a powder mixer (Make: Hexagon product development, Model: ALPHIE-3, Power supply: 0.3 HP, 230 V) for 6 hours in a clockwise as well as 6 hours in anticlockwise direction. Figure 3.2 (c) presents the morphology of powder particles after mixing.

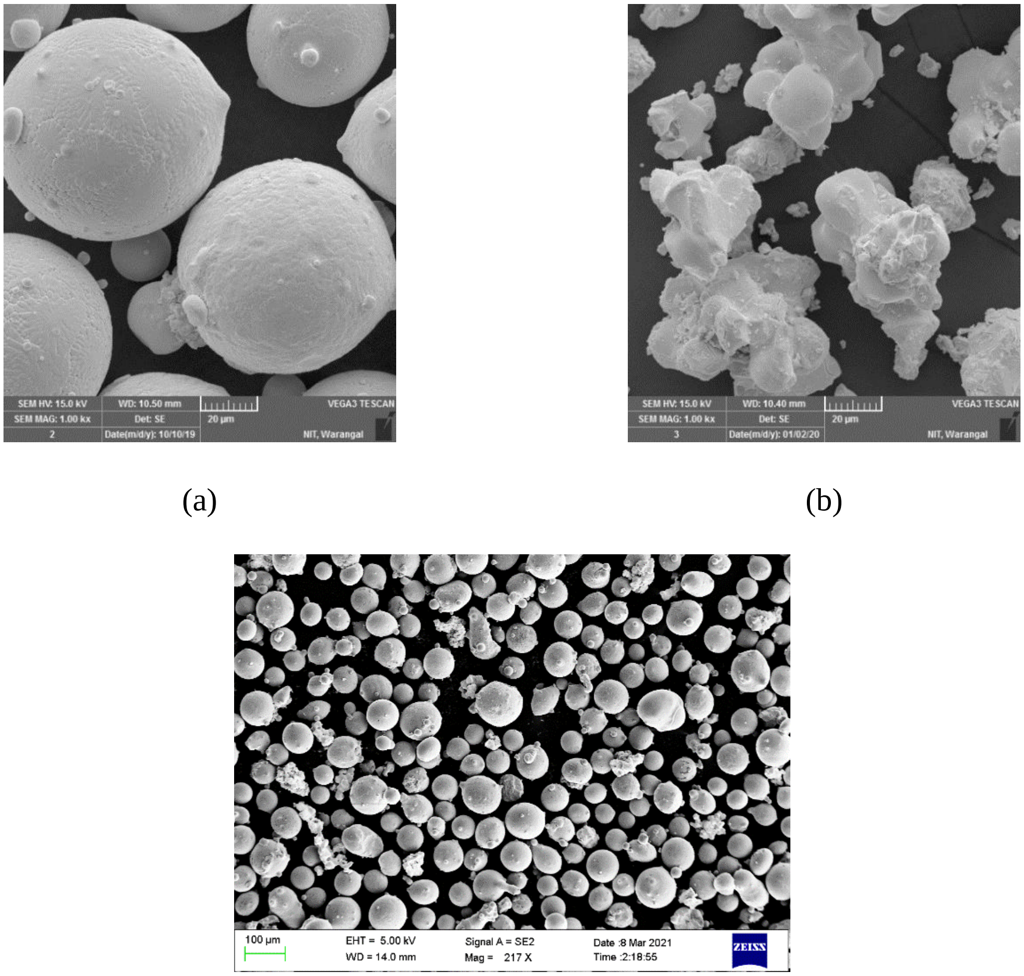

(a)

(b)

(c)

Figure 3.2 SEM image of powder morphology of (a) Stainless Steel 316 (SS 316) (b) Tungsten Carbide (WC) (c) after mixing of SS 316 and WC (8%)

3.2 Methods

In the present investigation, DED system as presented in figure 3.3 is used for depositing SS 316. The system consists of a 2 kW continuous wave fiber laser integrated with a 5 axis workstation and glove box. The system is attached with a dual powder feeder and Argon is used for carrying the powder to the deposition point. Laser and powder are fed through a co-axial nozzle to the point of deposition and a constant standoff distance of 15 mm and beam diameter of 3.2 mm are used for performing the experiments. The X and Y movement is achieved by the movement of the substrate and the increment in Z- direction for depositing one layer over the other is achieved by the movement of the laser head. The raster scanning strategy is deployed for bulk samples.

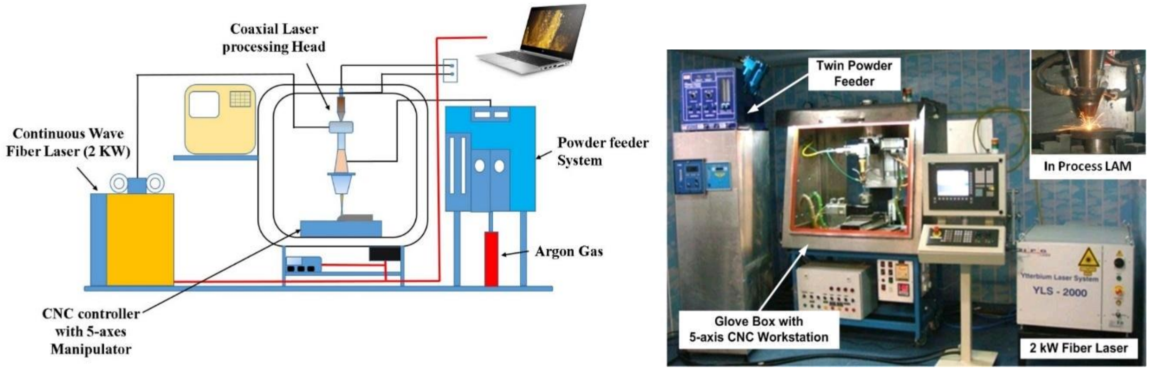

(a) (b)

Figure 3.3 (a) Schematic of DED system (b) DED system deployed for the experiments

The most significant DED process parameters are laser power, laser spot diameter, scanning speed and powder feed rate. As changing the laser spot diameter involves changing the experimental setup, it is kept constant during the study [43]. Full factorial experiments are performed by varying laser power, scanning speed and powder feed rate. Table 3.2 presents the levels used for parametric investigation for continuous deposition of SS 316. The levels for DED process parameters are fixed to avoid discontinuously and cracked deposition using trial experiments. The laser power is varied from 1000 W to 1400 W, scanning speed is varied from 0.4 m/min to 0.6 m/min and powder feed rate is varied from 3 g/min to 8 g/min at three levels each. The process parameters yielding continuous deposits with a maximum deposition rate and hardness are used for bulk deposition as shown in figure 3.4. Subsequent to deposition, the samples are cut transverse to the direction of laying using wire cut electrical discharge machining. The energy input (S) for each level is calculated by equation 3.1. The comparative parameter is akin to Simchi's energy input relationship, in which higher overall energy input to the material comes from increased power and decreased scanning speed. Because of the increased mass delivered to the melt pool and the energy required to melt the succeeding material, the overall energy input reduces with the addition of powder flow rate.

$$S = \frac{P}{v * m} \qquad 3.1$$

Table 3.2: Different combinations of DED process parameters and its corresponding energy input values

S. No	Laser power (W)	Scanning Speed (m/min)	Powder feed rate (g/min)	Laser energy $(\mathrm{W} * \mathrm{min}^2\mathrm{g}^{-1}\mathrm{m}^{-1})$
1	600	0.4	3	500
		0.5		400
2	800	0.4	3	667
		0.5		533.3
		0.6		444.4
3	1000	0.4	3	833.3
		0.5		667
		0.6		555.5
4	1000	0.4	6	417
		0.5		333
		0.6		277.7
5	1000	0.4	8	312.5
		0.5		250
		0.6		208.3
6	1200	0.4	3	1000
		0.5		800
		0.6		666.6
7	1200	0.4	6	500

		0.5		400
		0.6		333
8	1200	0.4	8	375
		0.5		300
		0.6		250
9	1400	0.4	3	1166.66
		0.5		933.3
		0.6		777.7
10	1400	0.4	6	583.3
		0.5		466.6
		0.6		389
11	1400	0.4	8	437.5
		0.5		350
		0.6		292

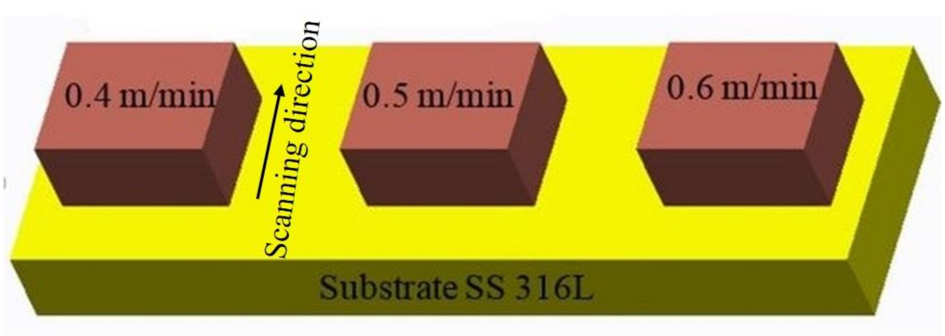

Figure 3.4 Schematic diagram of SS 316 blocks at different scanning speed

Heat treatment analysis is carried out to understand the behaviour of DED deposited SS 316 samples at different scanning speeds. Table 3.3 presents the DED process parameters used for fabricating SS 316 samples for heat treatment analysis, considering maximum hardness and deposition rate [119].

Table 3.3: DED process parameters for SS 316

Process Parameter	Value
Laser power	1000 W
Scanning speed	0.4, 0.5, 0.6 m/min
Powder feed rate	8 g/min
Overlapping ratio	50 %
Laser beam diameter	3.2 mm

The fabricated samples are mechanically polished prior to heat-treatment in a muffle furnace with a quenching facility. The heat-treatment temperatures are selected from previously published literature for SS 316 [82]. Heat-treatment is carried out at temperature of 1073 K and 1273 K (HT1073 and HT1273) for soaking period of 2 hours, followed by water quenching.

The single-track experiments for SS 316 composite are carried out initially by varying laser power (1000, 1200, 1400 W) and scanning speed (0.4, 0.5, 0.6 m/min) at a constant powder feed rate of 8 g/min. The process parameters yielding uniform WC particle distribution inside the SS 316 matrix is selected for further deposition. The bulk composite samples with different WC percentage such as 6% WC, 8% WC and 10% WC are deposited at the optimized parameters for further investigation.

3.3 Characterization tools

The samples are molded with resin and polishing with different grit papers followed by the diamond polishing. The electrolytic etchant (10% of oxalic acid in distilled water at a voltage of 5V for 15 s) is opted for microstructure analysis. Stereo microscope and optical microscope are used for investigating the geometry and microstructure of the deposits, respectively. Average micro-hardness is measured using a Vickers micro-hardness tester at a load of 0.98 N and dwell time period of 10 s. X-ray diffraction (XRD) is carried out from 30 - 100° at a scan step size of 0.016°. The Scherrer formula (refer equation to 3.2) is used for calculating crystallite size for DED samples in as-built and heat-treated samples.

$$d = \frac{C.\lambda}{\beta.cos\theta} \qquad 3.2$$

Where, C is Scherrer constant (0.9), λ is wavelength of the X-ray source, β is full width half maximum (FWHM) in radians, θ is peak position in radians. Rietveld analysis is carried out to estimate the volume fraction of phases in as-built and heat-treated conditions. Porosity analysis is carried out on the optical microscopy images using Image J software. The single cycle Automatic Ball Indentation (ABI) test is opted to compare the plasticity retaining capability of as-built and heat-treated samples as shown in figure 3.5. ABI is carried up to the maximum load of 100 N at a rate of 0.1 mm/min and unloading cycle till load of 10 N.

Figure 3.5 Automatic Ball Indentation (ABI) experimental test

Corrosion study is carried out using electrochemical corrosion set up as shown in figure 3.6. SS 316 samples polished up to 2000 grade grit paper and cleaned with acetone are used as the working electrode (WE) with an exposed area of 1 cm^2. 3.5 % NaCl solution in distilled water is used as the medium for the study. Ag/AgCl and platinum are used as reference electrode (RE) and counter electrode (CE), respectively during the study. Open circuit potential (OCP) is monitored for 1 hour and subsequent to the stabilization of the solution, the Tafel test is carried at a scan rate of 0.16 mV/sec.

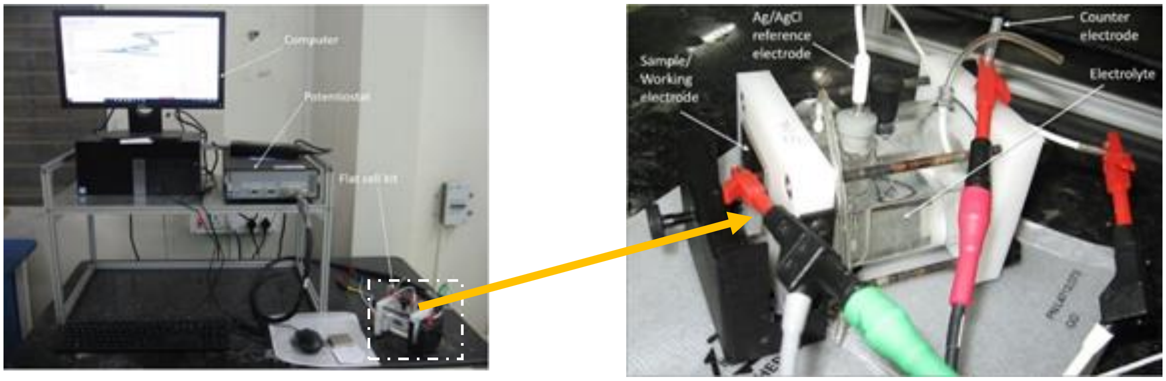

Figure 3.6 Electrochemical setup for corrosion test

Tribology tests are performed using a Pin-on-Disc apparatus as per ASTM-G99 standards as shown in figure 3.7. Cylindrical pins of size 5 mm×27 mm is extracted using wire-cut electrical discharge machining. The extracted pins are polished using different grit papers prior to the tribology test. The EN 31 stainless steel disc with a dimension of 165 x 8 mm is used as a counter material for tribology test. The acetone is used for cleaning the disc and test samples before and after each experiment. The experiments are conducted at constant a sliding distance of 1000 m at different values of normal load (10, 20 and 30 N) and sliding velocity (0.5, 0.75 and 1 m/s). Wear volume is estimated using equation 3.3 and the specific wear rate (SWR) is calculated using equation 3.4. Scanning Electron Microscopy (SEM) is used to analyze the worn surface to understand the wear mechanism. The sliding distance of 1000 m, sliding velocity of 0.5 m/s and normal load of 10 N are selected for conducting pin-on disc experiments for heat-treated samples. Tribology test for composite samples is carried out at normal load of 20 N, sliding velocity of 1 m/s and sliding distance of 1000 m

$$\text{Wear volume (mm}^3\text{)} = \frac{\textbf{Change in weight } (\Delta W)}{\textbf{Density } (\rho)} \tag{3.3}$$

$$\text{SWR (mm}^3\text{/Nm)} = \frac{\textbf{Wear volume(mm}^3\textbf{)}}{\textbf{Normal load } (N)\times\textbf{Sliding distance}(m)} \tag{3.4}$$

Figure 3.7 Experimental setup for Tribology test

CHAPTER 4

Process parametric investigations on Directed energy deposited (DED) Austenitic stainless steel 316 using experimental and finite element analysis

4.1 Introduction

In the previous chapters, the laser additive manufacturing (LAM) process was introduced, the literature review was carried out, gaps were identified and objectives were defined. In addition, the various experimental tools and material details were discussed. It is understood from the literature survey that parametric investigation is important to identify process parameters for continuous tracks deposition without the porosity and cracks for any material during LAM. Process parameter selection is also important for controlling the geometry of LAM built structures. In this chapter, parametric investigation is carried out to identify range of optimum process parameter combinations based on the track geometry by varying two combined DED parameters: laser energy per unit length (*E*) and powder feed per unit length (*F*). Combinations of process parameters yielding maximum hardness and maximum deposition rate are selected for bulk investigation. In addition, experiment results of track geometry are compared with finite element analysis at different combination of process parameters.

4.2 Process parametric Investigation

Initially, the single-track trial experiments are carried out by varying two combined DED parameters: laser energy per unit length (*E*) and powder feed per unit length (*F*) as shown in Table 4.1. *E* denotes the ratio of laser power to scanning speed and *F* refers to the ratio of powder feed rate to scanning speed. It is observed that discontinuous tracks are observed below 85 kJ/m and above 20g/m values of *E* and *F*, respectively. It is primarily because of the unavailability of sufficient "*E*" for regular track formation/ deposition (refer Figure 4.1a). Blackened and circular beads are observed above 210 kJ/m and below 5 g/m (refer Figure 4.1b). Continuous tracks are noticed above 85 kJ/m. It is primarily because of larger thermal energy due to higher "*E*" and lower *F*. Finally, the range of process parameters are used for continuous track deposition tabulated in 3.2.

Table 4.1: Trial experiments at different laser energy per unit length (*E*) and powder feed rate per unit length (*F*)

S. No	***P* (W)**	***v* (m/min)**	***m* (g/min)**	***E* (KJ/m)**	***F* (g/m)**	**Track image**	**Remarks**
1	600	0.4	3	90	7.5		No deposition
		0.5		72	6		
2	800	0.4	3	120	7.5		Discontinuous tracks
		0.5		96	6		
		0.6		80	5		
3	1000	0.4	3	150	7.5	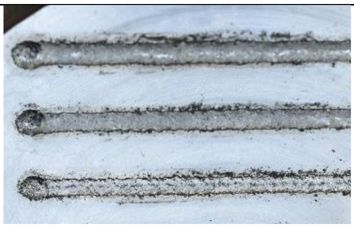	continuous tracks
		0.5		100	6		
		0.6		85.7	5		
4	1000	0.4	6	150	15		continuous tracks
		0.5		100	12		
		0.6		85.7	10		
5	1000	0.4	8	150	20	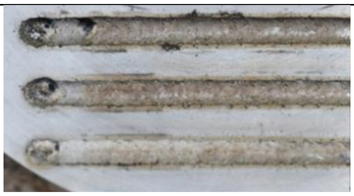	continuous tracks
		0.5		100	16		
		0.6		85.7	13.3		
6	1200	0.4	3	180	7.5	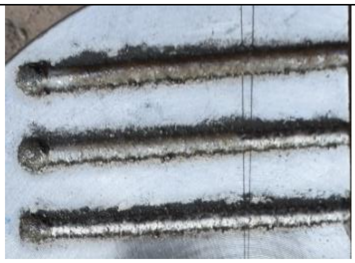	continuous tracks
		0.5		144	6		
		0.6		120	5		
7	1200	0.4	6	180	15		continuous tracks
		0.5		144	12		

		0.6		120	10		
8	1200	0.4	8	180	20		continuous tracks
		0.5		144	16		
		0.6		120	13.3		
9	1400	0.4	3	210	7.5		continuous tracks & Blackened
		0.5		168	6		
		0.6		140	5		
10	1400	0.4	6	210	15		continuous tracks & Blackened
		0.5		168	12		
		0.6		140	10		
11	1400	0.4	8	210	20		continuous tracks & Blackened
		0.5		168	16		
		0.6		140	13.3		

a b

Figure 4.1 Single track deposition at combination of a) $E< 85$ KJ/m & $F> 20$ g/m and b) $E> 210$ KJ/m & $F< 5$ g/m

Energy input calculations are carried out by considering combined effect of laser power, scanning speed and powder feed rate. Discontinue tracks are noticed when laser power $\leq$ 800 W, scanning speed of $\geq 0.5\ \mathrm{m/min}$ and at constant powder feed rate of 3 g/min due to insufficient energy to melt the powder material. Continuous tracks are noticed when laser power $\geq$ 1000 W, scanning speed of 0.4, 0.5 and 0.6 m/min and different powder flow rate of 3 g/min, 6 g/min and 8 g/min. The identified optimum range for continuous tracks for laser deposited SS 316 is (208.3-1166.66) $\mathrm{Wmin^{2}g^{-1}m^{-1}}$ when laser power $\geq$ 1000 W.

Adopting the full factorial design of experiments for analyses at three levels, twenty-seven tracks are laid by varying laser power, scanning speed and powder feed rate. The cross-section of single tracks is analyzed using optical microscopy and track width (*W*) and height (*H*) of track cross-section is measured at different locations using Image J software. Figure 4.2 presents the typical cross-section of DED single track deposit. Table 4.2 presents the width, height, deposition rate and hardness of single tracks deposited at different combinations of DED parameters.

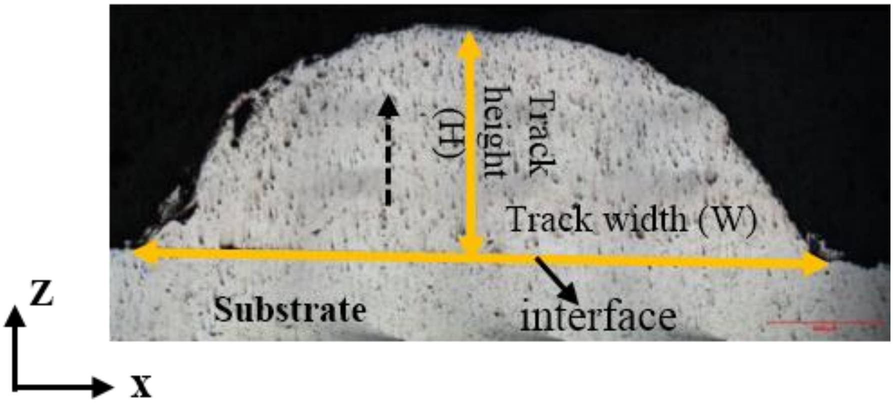

Figure 4.2 Typical cross-section of track geometry

Table 4.2: DED process parameters with track geometry, deposition rate and micro-hardness

S. No.	Laser power (W)	Scanning speed (m/min)	Powder feed rate(g/min)	DR (mm^3/min)	Average micro-hardness
1	1000	0.4	3	260.78 ± 13.04	213.6 ± 5.34
2	1200	0.4	3	371.78 ± 18.6	213.9 ± 5.35

3	1400	0.4	3	471.56 ± 23.6	237.9 ±5.95
4	1000	0.4	6	499.89 ± 25	249.2 ±6.23
5	1200	0.4	6	881.57 ± 14.08	230 ±5.75
6	1400	0.4	6	911.00 ±25.55	208.5 ±5.21
7	1000	0.4	8	1175.18 ±25.76	296 ±7.4
8	1200	0.4	8	1276.30 ±28.81	212.7 ±5.32
9	1400	0.4	8	1434.79 ±23.74	202.15 ±5.05
10	1000	0.5	3	248.41 ±12.42	203.4±5.08
11	1200	0.5	3	436.94 ±21.85	225.5 ±7.27
12	1400	0.5	3	434.96 ±21.75	206.56 ±7.33
13	1000	0.5	6	456.13 ±22.81	243.4 ±6.08
14	1200	0.5	6	789.19 ±39.46	247.1 ±8.35
15	1400	0.5	6	834.43 ±24.72	230 ±10.5
16	1000	0.5	8	1291.28 ±38.56	262.18 ±6.55
17	1200	0.5	8	1311.71 ±39.58	218 ±8.9
18	1400	0.5	8	1312.2 ±65.61	204 ±8.2
19	1000	0.6	3	195.87 ±9.79	194.2 ±4.85
20	1200	0.6	3	354.17 ±17.70	220.3 ±7.01
21	1400	0.6	3	405.38 ±20.26	214.6 ±6.73
22	1000	0.6	6	427.66 ±21.38	241.45 ±6.03
23	1200	0.6	6	664.37 ±33.21	211.2 ±9.56
24	1400	0.6	6	834.21 ±21.71	245 ±8.25
25	1000	0.6	8	913.43 ±27.67	258.6 ±6.46
26	1200	0.6	8	1169.28 ±35.46	218 ±8.9
27	1400	0.6	8	1261.31 ±33.06	195.25 ±9.76

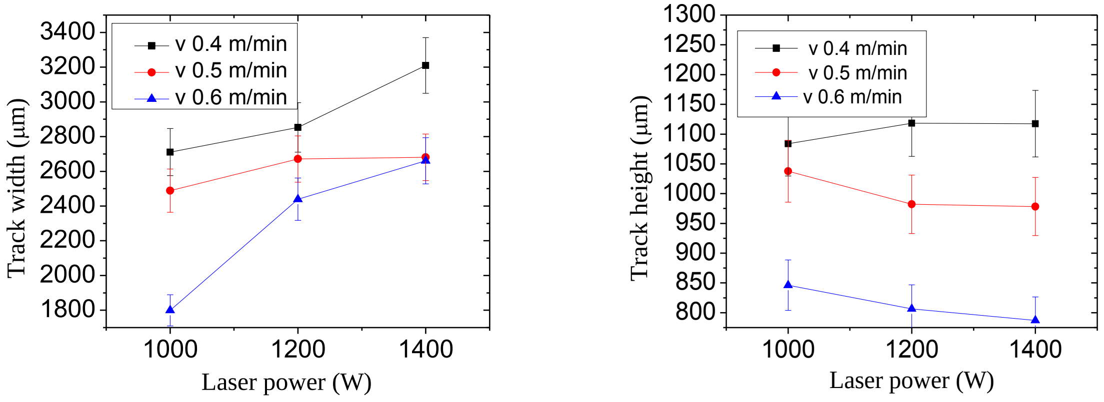

(a) (b)

Figure 4.3 Variation of (a) Track width (b) Track height under different laser power and scanning speed at constant powder feed rate of 8 g/min

Figure 4.3 presents the variation of track geometry with laser power and scanning speed at a constant powder feed rate of 8 g/min. It is observed from figure 4.3a that the track width increases with laser power at a constant powder feed rate and it is attributed to an increase in laser energy per unit length (laser power/scanning speed) resulting in large melt pool width. Similarly, the rise in track height with laser power of 1000 W is observed. However, the reduction of track height is observed at higher values of laser power (≥ 1200 W). It is ascribed to excessive laser energy per unit length causing the material loss due to evaporation of low melting point of chemical elements, which directly influence the microstructure and mechanical properties of DED built SS 316. The observations are in line with other research work [120]. In addition, the decrease in track width and height with increased scanning speed is noticed at all process parameter combinations. It can be attributed to the reduction in laser energy per unit length during single track deposition and reduction of interaction time (Beam diameter/scanning speed).

Further, the deposition rate is estimated using equation 4.1, where n is the geometry factor and v is the scanning speed. [43]. Deposition rate increases with laser power whereas it decreases with scanning speed as shown in figure 4.4a. This is due to the combined effect of laser energy per unit length and powder feed per unit length (powder feed rate/scanning speed). An increase in laser energy per unit length and powder feed per unit length leads to an increase in deposition rate at a higher value of laser power and powder feed rate, and lower values of scanning speed due to a wider melt pool and a large amount of powder available for deposition.

$$\text{Deposition rate} = n \times W \times H \ \times v \tag{4.1}$$

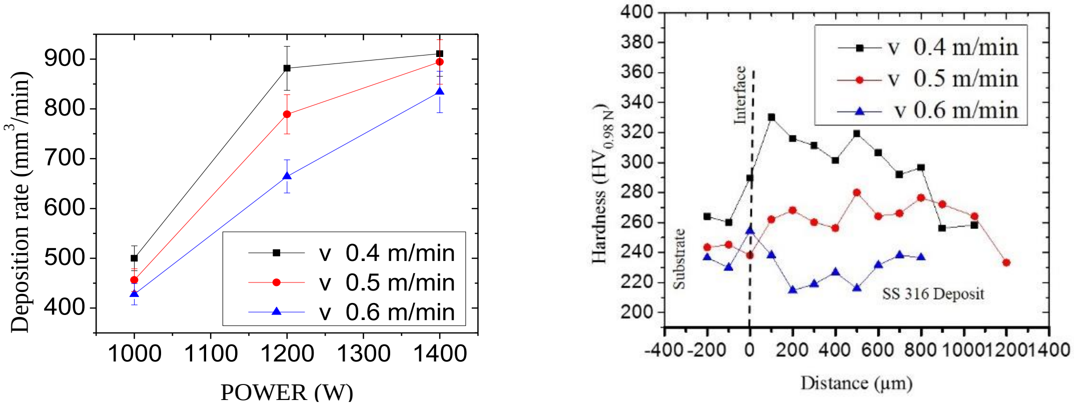

(a)

(b)

Figure 4.4 Effect of laser power and scanning speed on (a) Deposition Rate (b) Micro-hardness

Figure 4.4b presents the variation of hardness along with the vertical distance from the substrate to laser deposited track top surface at a constant laser power of 1000 W. A sudden transition in hardness started from the interface of track and substrate owing to large thermal gradients. A sudden increase is observed at 0.4 m/min and 0.5 m/min, but a sharp decrease is observed at 0.6 m/min at the substrate and track interface. This variation can be due to the difference in the grain structure between substrate and deposit. Figure 4.5a shows the fluctuations in hardness with different powder feed rate and laser power at a constant scanning speed of 0.4 m/min. The low hardness values are attained at high laser powers (≥1200 W) especially with high powder feed rates ($\geq 6\ g/\text{min}$) and it might be attributed to higher laser energy per unit powder feed rate subsequently more voids and pores. It can be observed from figure 4.5b that the high hardness value is attained at high powder feed rate under constant laser power of 1000 W. It is attributed to lower values of laser energy per unit powder feed rate (Laser power/ Powder feed rate), resulting in high hardness and cooling rates. Apart from this, the reduction in hardness values is noticed when scanning speed increases from 0.4 to 0.6 m/min. It can be ascribed to high porosity and lack of fusion during deposition at higher values of scanning speed (0.5 and 0.6 m/min). The diamond tip of the Vickers micro-hardness intender easily penetrates into the track surface due to the presence of pores within the measured area. This results in a lower value of micro-hardness at a higher scanning speed. This is in line with the previous observations on L-PBF built SS 316L samples [48]. Considering the applications of the present work, maximum deposition rate and hardness are considered as the criteria for selecting the process parameters for bulk deposition. Higher hardness values of 258.6, 262.18, and 292 HV are attained with laser power of 1000 W, deposition rate of 8 g/min and at 0.4, 0.5 and 0.6 m/min. The high deposition rates are achieved at a laser power of 1200 and 1400 W as shown in figure 4.4a, but low hardness values are observed due to the presence of pores and voids inside the sample as shown in figure 4.5a. It can be attributed to the evaporation of low melting point elements in SS 316 [72]. In addition, it can be seen from figure 4.5b that hardness reduces with an increase in scanning speed due to increased porosity and a similar observation is reported by Sun et al. [51]. Thus, the identified combination of process parameters: laser power of 1000W, powder feed rate of 8 g/min and different scanning speed of 0.4 m/min, 0.5 m/min and 0.6 m/min for maximum hardness and deposition rate. Further, three blocks are deposited with dimensions of 25 mm x 25 mm x 10 mm at 50% overlap for further investigations.

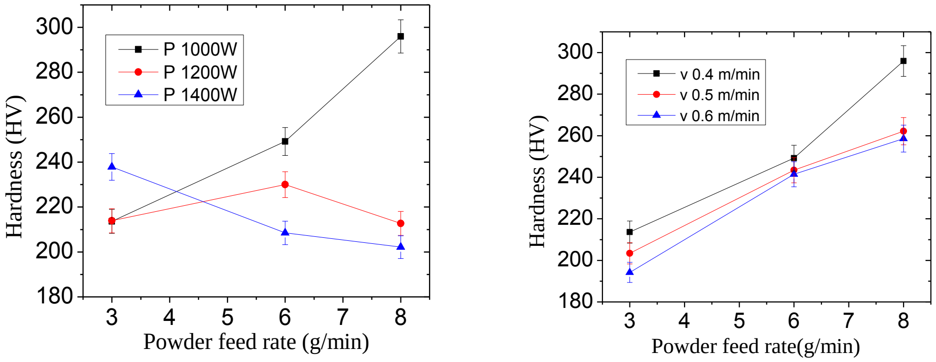

(a) (b)

Figure 4.5 Variation of hardness under different powder feed rate and (a) laser power at constant scanning speed of 0.4 m/min (b) scanning speed at constant laser power of 1000 W

4.3 Finite element analysis

4.3.1 Assumptions

1. The material is considered to be isotropic
2. The effect of surface tension and capillary is negligible.

4.3.2 Governing equations

An axisymmetric model with the dimension of (5 x 2 mm) has been developed to predict the track geometry and thermal analysis during DED process using Comsol Multiphysics 5.3 as shown in figure 4.6.

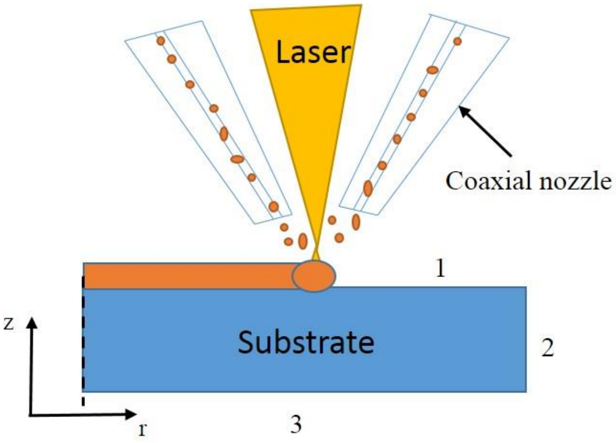

Figure 4.6 Schematic axi-symmetric model for DED

The energy and mass balance equations (4.2 and 4.3) are used in the present analysis [109].

$$\rho C_p \frac{\partial (T)}{\partial t} + \rho C_p \mathrm{V_n} \Delta T + \nabla(-K\Delta T) = Q_r\text{-}\mathrm{Q}_{\mathrm{loss}} \tag{4.2}$$

$$\eta = \frac{A_t \rho v}{m} \tag{4.3}$$

where ρ *is density* $(\frac{kg}{m^3})$, T is temperature (K) , C_p is specific heat capacity (J/kg.K), t is time (s), V_n is boundary velocity (m/s) , Q_r is heat source $(\frac{W}{m^2})$ and K is thermal conductivity (W/m^{2}K), Q_{loss} is the energy lost into ambient air by thermal radiation and convection and by heat conduction,A_t is track area, η is powder efficiency and v is scanning speed.

4.3.3 Heat source

Temperature distributions have a significant impact on the track geometry created during laser deposition. The energy absorbed by the substrate and powder components determines the temperature distributions inside the melt pool. The laser energy used in this current study is implemented by equation (4.4) [110] .For the Nd:YAG laser, the absorption by steel substrate is assumed to be constant, with a value of roughly 0.47. Using the rule of mixtures, the absorptivity of various alloys may be estimated given their composition and the absorptivity of the constituent elements.

$$Q_r = \frac{(4.45AP)}{\pi r^2} \exp(-4.5 \, \frac{(r-vt)^2}{r^2})) \qquad (4.4)$$

Here, the substrate temperature is considered to be room temperature , A is a fraction of heat input to powder, P is laser power, v is scanning speed, r is laser beam radius, ε is emissivity, m is powder feed rate and h is convective heat transfer coefficient. The parameters are used for the FEM analysis presented in Table 4.3.

Table 4.3: Parameters used for finite element analysis

Parameters	Values
A	0.47
ρ_o	7000 $\frac{kg}{m^3}$
r	1.6 mm
T_o	273.15 K
h	10 $\frac{W}{m^2K}$
ε	0.7
C_p	500 J/kg.K
K	16 W/mK

4.3.4 Resolution Parameters & Mesh

The triangular mesh is applied to model and the maximum and minimum mesh sizes are 50 μm and 0.1 μm, respectively. The material deposition throughout the DED process is shown by the expansion of the top surface. The moving mesh is controlled by D_g nodes in COMSOL using the laplace smoothing approach. The direct PARDISO solver is used in conjunction with the generalized- time solver to accomplish the iterative solution. The relative and absolute tolerances are 10^{-2} and 10^{-3}, respectively.

4.3.5 Boundary conditions

The boundary conditions are applied for the axisymmetric model presented in table 4.4. The track geometry is developed by using moving mesh which takes into account for mass addition and solidification phase changes. V_n is boundary velocity due to powder addition and r_p is mean diameter of the powder particles. The calculation of V_n is given by equation 4.5 [109].

Table 4.4: Boundary conditions

Heat transfer	Boundary 1	Boundary 2,3
	$Q_r = \frac{(4.45AP)}{\pi r^2} \exp(-4.5\ \frac{(r-vt)^2}{r^2})$ $Q_{loss} = h\ (T - T_o) - \sigma_b \varepsilon (T^4 - T_o^4)$	$Q_{loss} = h\ (T - T_o) - \sigma_b \varepsilon (T^4 - T_o^4)$
Deformed geometry	V_n	$V_n = 0$

$$V_n = \frac{\boldsymbol{2\eta m}}{\boldsymbol{\rho \pi r_p^2}}\ \exp(-4.5\ \frac{(r-vt)^2}{r_p^2}) \qquad (4.5)$$

4.3.6 Effect of laser power on track geometry

The changes in track width and height are demonstrated under different laser power, at constant scanning speed and powder feed rate in figure 4.7. The increasing track width and height is observed with laser power and it can be due to increase in laser power per scanning speed.

From an analytical study, it was observed that the maximum temperature noticed with different laser power of 1000, 1200, 1400 W is 1800, 2000, 2200 K respectively. The maximum temperature induced in the melt pool is increased with laser power as shown in figure 4.8.And also observed that the changes in track width is more significant than the changes in track height when increasing laser power.It can be attributed to available energy per unit length is high and changes in a temperature gradient in melt pool. A similar observation was noticed by Shuhao Wang et.al [121].

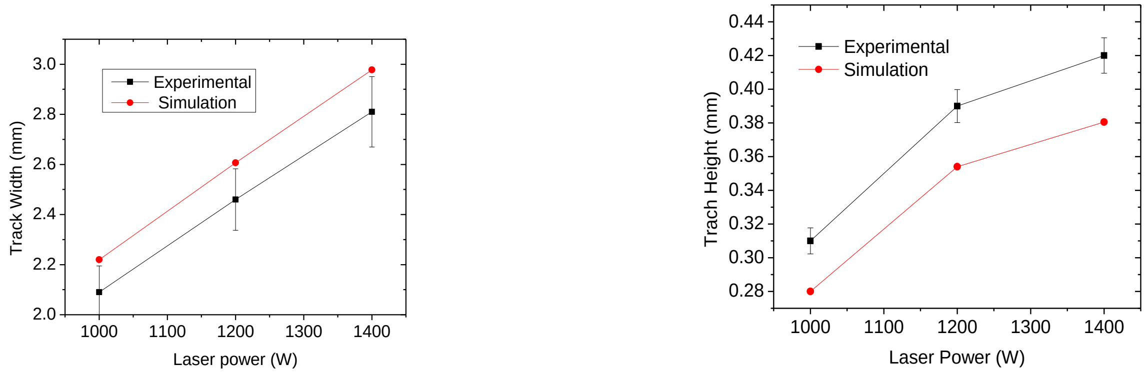

(a) (b)

Figure 4.7 Effect of laser power on (a) track width (b) track height at constant scanning speed and powder feed rate

(a) (b)

Figure 4.8 Variation of track width and height with laser power (a) 1000 W (b) 1200 W at constant scanning speed and powder feed rate

4.3.7 Effect of scanning speed on track geometry

The variation of scanning speed on the track height and width is observed at a laser power of 1000 W and a powder feed rate of 6 g/min depicts in figure 4.9. The decreasing track width and height are noticed with scanning speed. It might have attributed to insufficient laser power per scanning speed and reducing the laser beam interaction with powder. The temperature-induced in melt pool is reduced with increasing scanning speed as shown in figure 4.10. It may be due to the reduction in laser beam interaction with powder and Yuze Huang et al. observed similar results [122]. The maximum temperature of 2500, 2200 and 1800 K for different scanning speed 0.4, 0.5 and 0.6 m/min is noticed from analytical results.

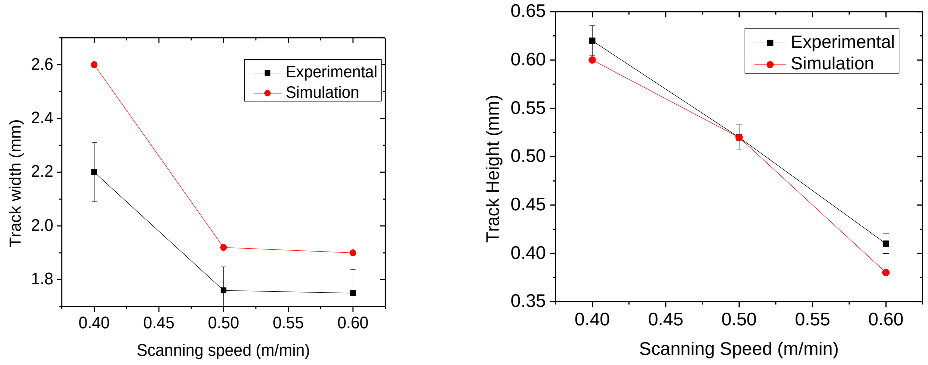

(a) (b)

Figure 4.9 Effect of scanning speed on (a) track width (b) track height at constant laser power and powder feed rate

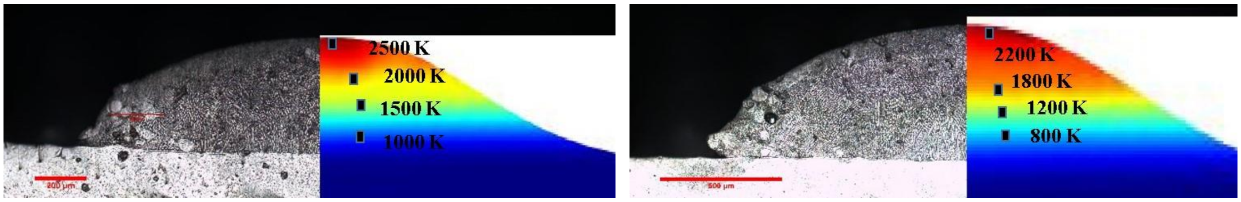

(a) (b)

Figure 4.10 Track width and height with different scanning speed (a) 0.4 m/min (b) 0.5 m/min at constant laser power and powder feed rate

4.3.8 Effect of powder feed rate on track geometry

Figure 4.11 depicts the variation of track width and height with different powder feed rate at a laser power of 1000 W and a scanning speed of 0.4 m/min. As increasing powder feed rate, the rise in track width and height is observed, due to available powder per unit energy increases. The track height is more sensitive to powder feed rate than the track width is noticed with increased powder feed rate due to available powder per unit length increases. The statement was supported by previous authors [122,123]. From analytical results, noticed that the utmost temperature induced in the melt pool is also increasing with powder feed rate owing to heat accumulation within the melt pool as shown in figure 4.12.

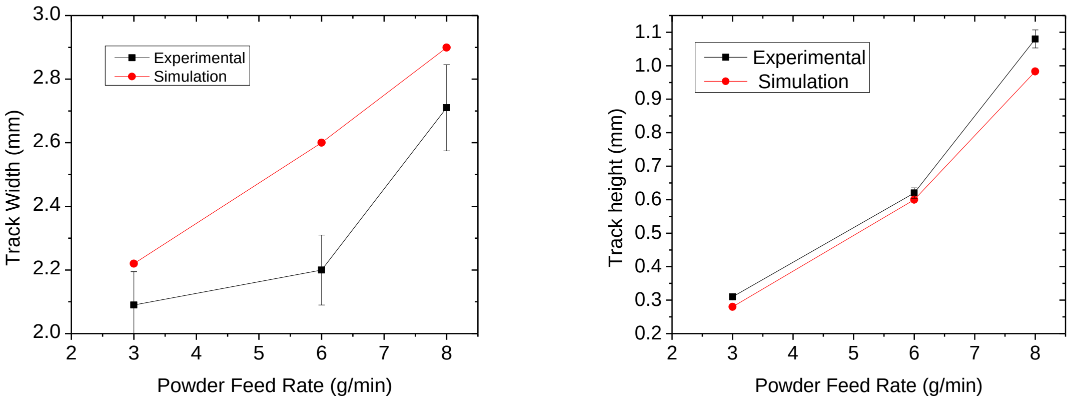

(a) (b)

Figure 4.11 Effect of powder feed rate on (a) track width (b) Track height at constant laser power and scanning speed

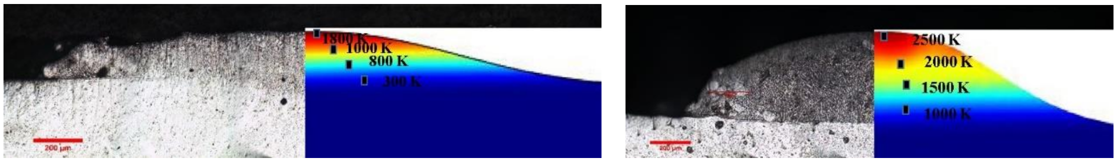

(a) (b)

Figure 4.12 Track width and height under different powder feed rate (a) 3 g/min (b) 6 g/min at constant laser power and scanning speed

4.4 Summary

The track width and track height increases with an increase in laser power and the reduction in track height is observed at higher values of laser power (≥1200 W). In addition, the decrease in track width and track height with increase in scanning speed is noticed at all process parameter combination. The low hardness values are attained at high laser powers (≥ 1200 W) especially with high powder feed rates (≥ 6 g/min) and the reduction in hardness values is noticed when scanning speed increases from 0.4 to 0.6 m/min. It can be ascribed to high porosity and lack of fusion during deposition at higher values of scanning speed.The identified process parameters for bulk deposition are laser power of 1000 W, powder feed rate of 8 g/min and scanning speed of 0.4 m/min, 0.5 m/min and 0.6 m/min. The variation in the track width and track height at different laser power, scanning speed and powder feed rate during finite element analysis is similar to experimental results and maximum percentage error is 9%.

CHAPTER 5

Characterization of Directed Energy Deposited SS 316 bulk samples

5.1 Introduction

In the previous chapter, the different process parameter combinations are identified, and experimental results are compared with finite element analysis. Subsequently, SS 316 bulk structures are deposited at laser power of 1000 W, powder feed rate of 8 g/min and different scanning speed of 0.4, 0.5 and 0.6 m/min. In this chapter, microstructure characterisation, hardness and tribological studies of DED built SS 316 bulk samples is carried out at different scanning speed.

5.2 XRD analysis

Figure 5.1 illustrates the XRD pattern of DED built SS 316 bulk structures under different scanning speed. The austenitic phase (γ) is detected at all the conditions presented in figure 5.1. However, ferrite (δ) peak is observed with low scanning speed and it is attributed to micro-segregation and thermal gradients [124]. A slight shift in the austenitic (γ) peaks towards the left is observed with increased scanning speed primarily due to variation in residual stresses. The peak positions of lattice plane γ (111) are $43.71702^{o}, 43.71449^{o}$ and 43.6668^{o} at 0.6 m/min, 0.5 m/min and 0.4 m/min, respectively. Thus peaks shift towards left with a degree of 0.0025^{0} and 0.05^{0} is observed at 0.5 m/min and 0.4 m/min respectively as compared to peaks obtained at scanning speed of 0.6 m/min. The crystallite size (d) of DED SS 316 at three scanning speed was calculated using the Scherrer equation as shown in equation (3.1). It can be observed from figure 5.1 that the peak width is increasing with an increase in scanning speed from 0.4 m/min to 0.6 m/min. This is mainly due to the reduction in crystallite size with an increase in scanning speed. The estimated crystallite size using Scherrer equation shows that minimum crystallite size is obtained at 0.6 m/min. The estimated crystallite size is 36.741 nm, 36.399 nm and 24.886 nm at 0.4 m/min, 0.5 m/min and 0.6 m/min, respectively. Relatively, fine crystallites are obtained at 0.6 m/min mainly due to the faster cooling rate at higher scanning speed.

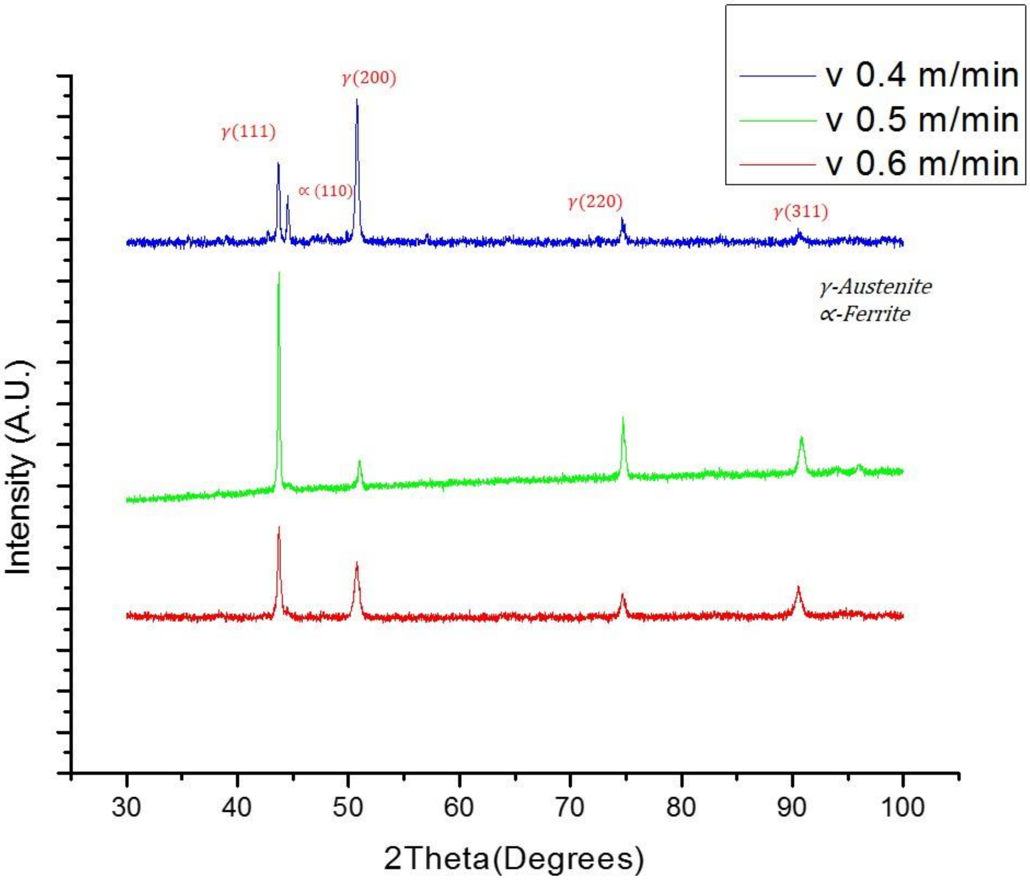

Figure 5.1 XRD scans for laser deposited SS 316 with different scanning speed

5.3 Microstructure

The temperature gradient (G) and growth rate (GR) influences the microstructure of the DED samples. The ratio $\frac{G}{GR}$ generally decides the type of microstructure after solidification and product $G \times GR$ indicates the cooling rate which directly influences the grain size. Figure 5.2 shows the influence of $\frac{G}{GR}$ and $G \times GR$ on the solidification structure and morphology. Figure 5.3b shows the columnar growth for all the samples with slight variation in dendrite size due to the difference in cooling rates. The measured dendritic size is 7.22 μm, 6.99 μm and 6.11 μm for 0.4 m/min, 0.5 m/min and 0.6 m/min respectively, due to low laser energy available at high scanning speeds and consequently achieved high cooling rates. The increase in the percentage of porosity is observed with an increase in scanning speed as shown in figure 5.4, and it can be attributed to the insufficient laser energy available per unit length (laser power/scanning speed) resulting in lack of fusion porosity. These are in line with the observations made by Hu et al. [125] during LAM of 17-4PH stainless steel. The optical microscopic (OM) images for porosity analysis with an increase in scanning speed under constant laser power and powder feed rate as shown in figure 5.5. The similar observations are noticed by OM images.

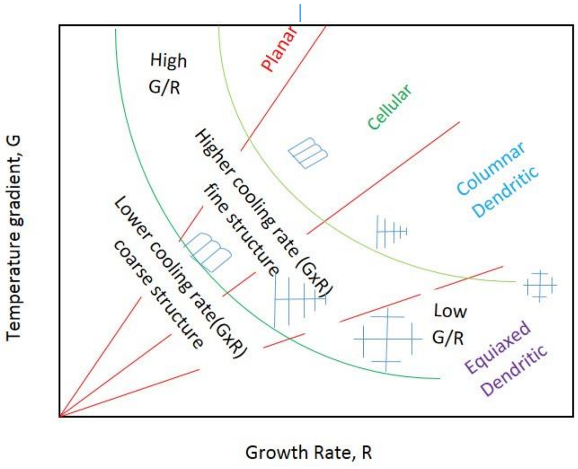

Figure 5.2 Influence of growth rate (GR) and temperature gradient (G) on the size of solidification structure and morphology [3].

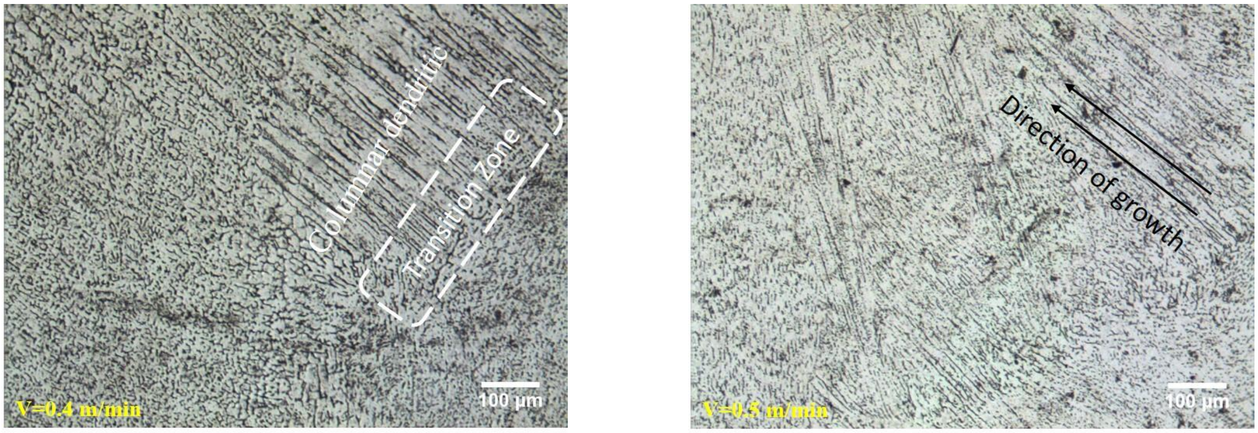

(a) (b)

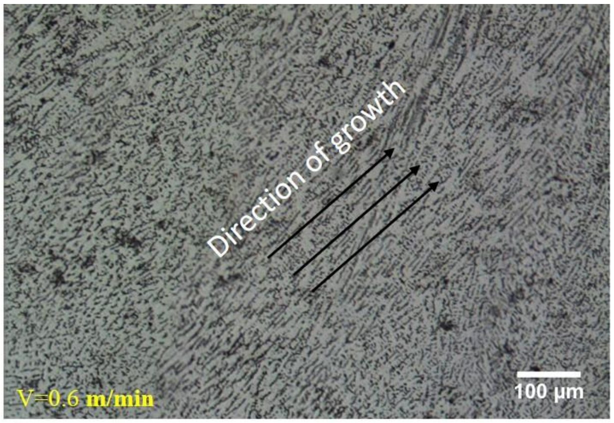

(c)

Figure 5.3 Optical microscopic microstructure images of SS 316 at constant laser power of 1000 W and powder feed rate of 3 g/min, and different scanning speed (a) 0.4 m/min (b) 0.5 m/min (c) 0.6 m/min

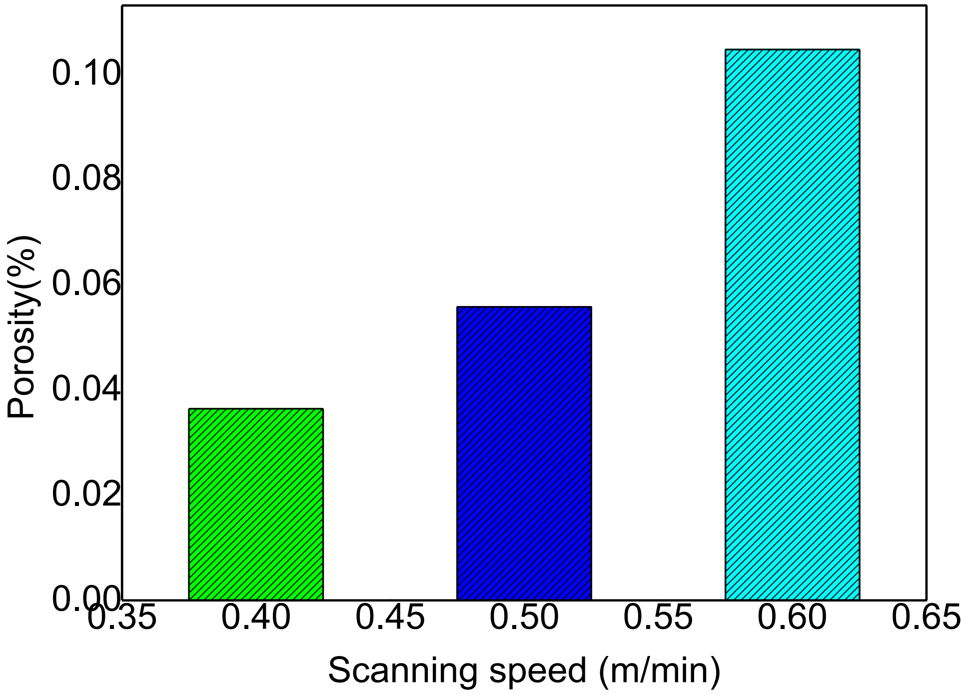

Figure 5.4 Variation of percentage of porosity under different scanning speed

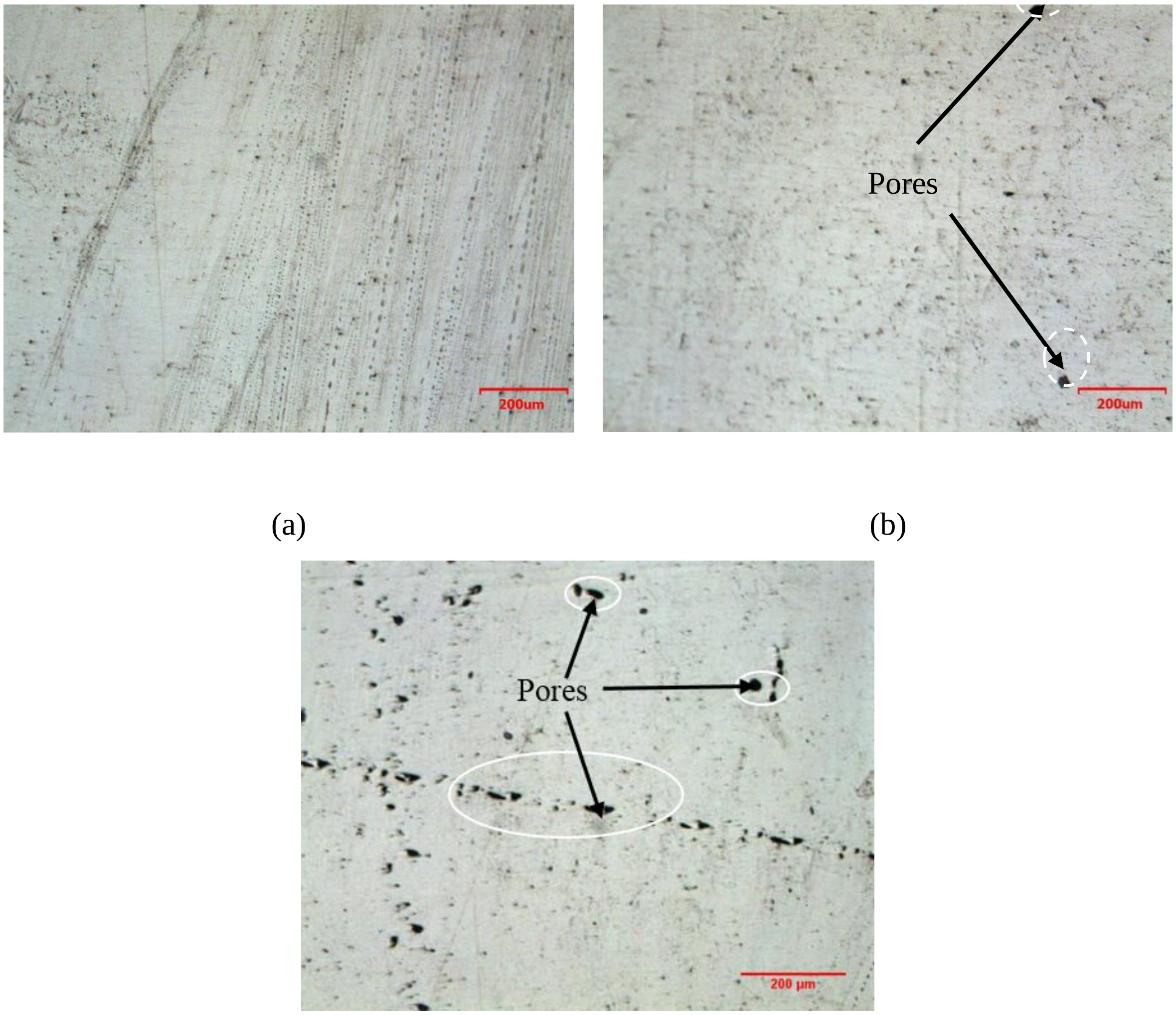

(a) (b)

(c)

Figure 5.5 Optical microscopic images for porosity analysis under constant laser power of 1000 W and powder feed rate of 3 g/min, and different scanning speed (a) 0.4 m/min (b) 0.5 m/min (c) 0.6 m/min

5.4 Hardness

Figure 5.6a presents the variation of micro hardness for laser deposited bulk samples under different scanning speed at a constant laser power of 1000 W. The Vickers micro hardness are taken along the vertical direction of the transverse cross-section of built samples as shown in figure 5.6b. It is observed that the hardness increases with reduction in scanning speed at a constant laser power of 1000 W. It is attributed to the high percentage of pores and incomplete fusion due to the reduction in available laser energy per unit length during deposition at higher scanning speed. A similar trend is observed by Sergio et al.[41]. The obtained average hardness value is 317.42 HV at scanning speed of 0.4 m/min. Figure 5.7 shows the comparison of average micro-hardness values of SS 316 built using DED, L-PBF and conventional methods. The average micro hardness values of SS 316 samples are 326.3± 10.2 HV [126], 317.42 HV and 215-225 HV [127] for LAM –PBF , DED and conventional annealed cast sample respectively. A slight increase in micro hardness of L-PBF samples can be attributed to the relatively faster scanning speed in L-PBF process as compared to DED, leading to a faster cooling rate, fine microstructure and higher hardness. Typical values of cooling rate are 10^5 K/s for LAM process and ~ 10^0 - 10^2 K/s for conventional samples [43].

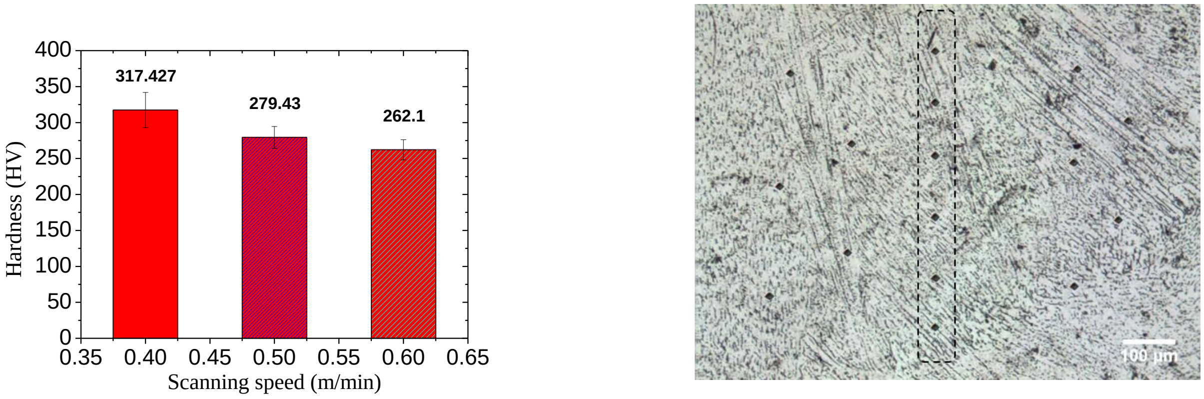

(a)

(b)

Figure 5.6 (a) Variation of micro- hardness for laser deposited bulk samples under different scanning speed at constant laser power of 1000 W and (b) Vickers- Micro hardness indenters along the build direction

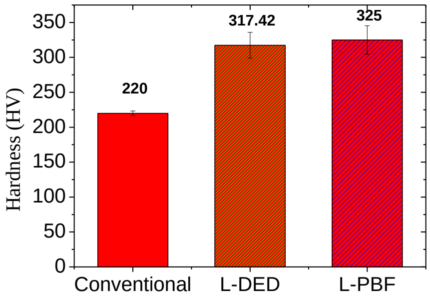

Figure 5.7 Micro hardness of SS316 for conventional and additive manufacturing techniques (L-DED and L-PBF)

5.5 Tribology

Figure 5.8 presents the specific wear rate of DED built SS 316 samples carried out at different scanning speed, sliding velocity and normal load at a constant sliding distance. The increase in wear loss is observed with the rise in sliding velocity under all normal load conditions. From results, it can be noticed that increment in wear loss noticed from 0.18557×10^{-4} mm^3/Nm to 0.295×10^{-4} mm^3/Nm, when sliding velocity is increased from 0.5 m/s to 1 m/s under a normal load of 10 N. It is attributed to a higher amount of friction heat generation resulting in increased wear due to material softening and consequently severe plastic deformation.

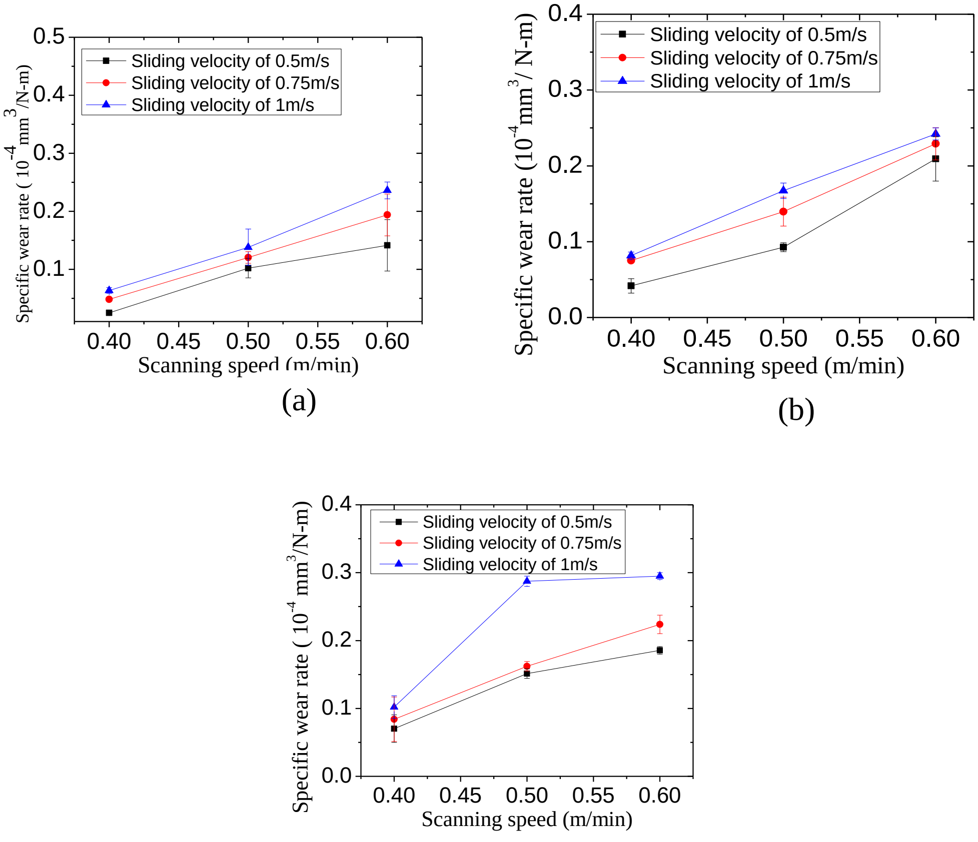

(a)

(b)

(c)

Figure 5.8 Variation of wear loss at different normal load (a) 10N (b) 20N (c) 30N with different laser scanning speed and sliding velocity

In addition, it is observed that the applied normal load significantly influences the specific wear rate than the sliding velocity. The rise in specific wear rate from 0.0247×10^{-4} mm^3/Nm to 0.07022×10^{-4} mm^3/Nm is observed from figure 5.8 when increasing normal load from 10 N to 30 N and similar observations are reported by Li et al [48]. It can be ascribed to delamination of the surface due to the severe plastic deformation due to adhesive wear. In contrast, a sharp decrease in specific wear rate is observed when DED built samples with laser scanning speed greater than 0.4 m/min under three normal load conditions. It may be attributed to pores under samples are compressed at high normal loads and it reduces earlier crack initiation which in turn low specific wear rates. In addition, wear particles move inside the pores and cold welded under high contact pressure during the wear test. These cold welded particles further reduce the specific wear and similar results are reported by Bartolomeu et al. and Hua Li et al. [48,128]. It can be seen from figure 5.8 that the rise in specific wear rate can be clearly observed for samples built with the LAM- DED samples with scanning speed >0.4 m/min due to rise in the percentage of pores and lack of fusion, and similar trend is identified by previous authors [51]. Figure 5.9 shows the evaluation of coefficient of friction (COF) with scanning speed under different normal load and sliding velocities. The high friction values are attained at low sliding velocity and normal load. It is ascribed to the high asperities in the mating surfaces and consequently retards the movement of counter surface. As time moves on, the mating surfaces free from surface asperities lead to constant COF is observed.

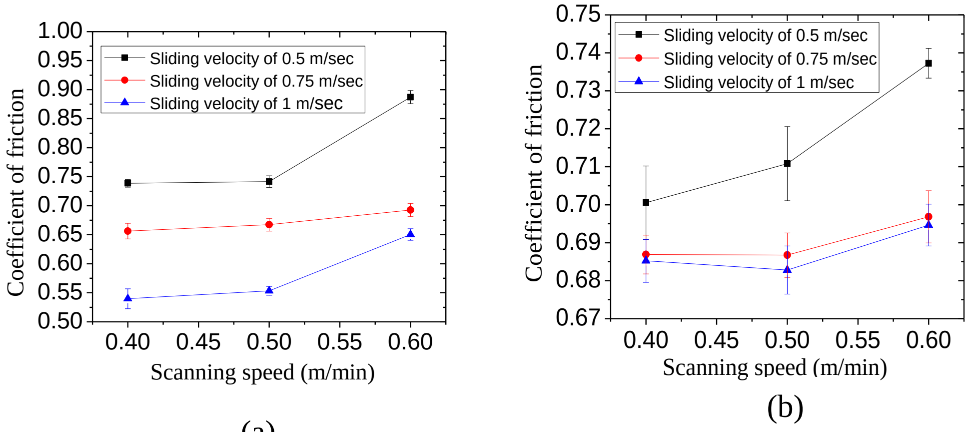

(a)

(b)

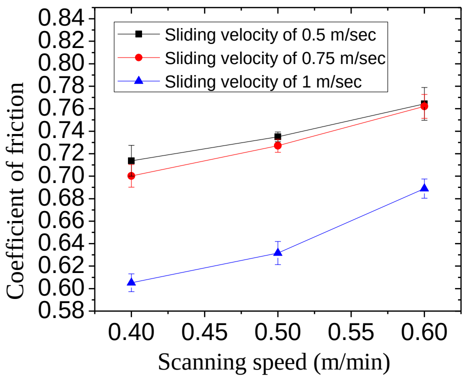

(c)

Figure 5.9 Variation of COF at different normal load (a) 10N (b) 20N (c) 30N with different scanning speed and sliding velocity

The difference in coefficient of friction (COF) values is not more significant at low sliding velocity and normal load due to the low frictional heat generation. In contrast, decreasing in COF values is observed at high sliding velocity and normal load. It can be attributed to the high frictional heat generation resulting in oxide layer formation which acts as tribo-layer leading to reducing in COF. In addition, sliding velocity less than 0.75 m/sec gave higher COF values due to the low interface temperature resulting in no oxide layer and consequently high contact pressure between two mating surfaces. Apart from this, the rise in the trend of COF with scanning speed is noticed as shown figure 5.9. It is attributed to the presence of wear particles cold welded into the pores of SS 316 with increased scanning speed and consequently rougher contact surface. A similar observation is also reported by Li et al. [48]. Figure 5.10 shows the variation of SWR and COF of DED SS 316 and conventional made SS 316L under different sliding velocity. The wear resistance and COF of DED samples are superior to convention made SS 316L. It can be attributed to high cooling rate resulting in fine grain size and high hardness of DED built SS 316 samples. Figure 5.11 illustrates that the scratches and ploughing grooves are aligned parallel to the sliding direction due to the consequence of abrasive wear and a relatively smooth worn surface is identified at lower sliding velocity. The fine wear debris and adhesive wear are noticed at intermediate normal load conditions as shown in figure 5.11e and similar observation is identified by Farias et al [129]. Whereas wear particles are cold welded and forms a rougher surface at normal load of 30 N.

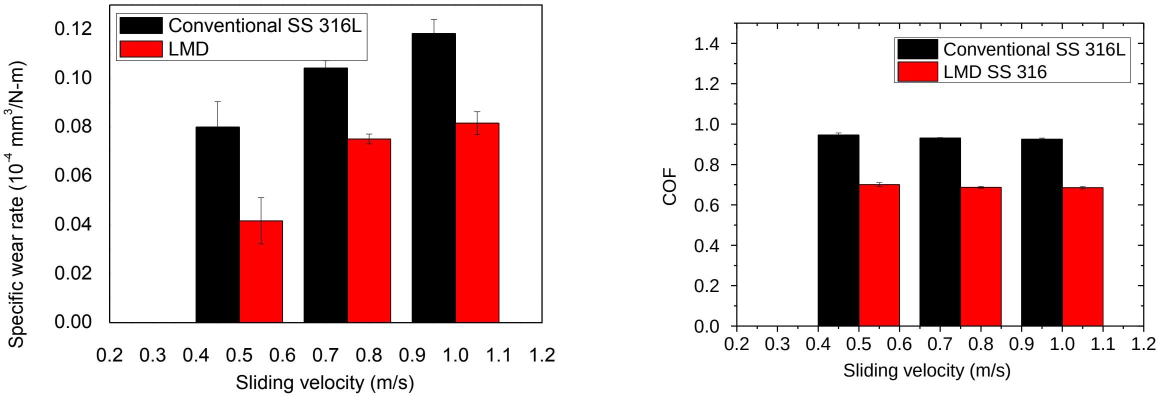

(a) (b)

Figure 5.10 Variation of (a) specific wear rate and (b) COF of convention SS 316L and laser melting deposited SS 316 under different sliding velocity

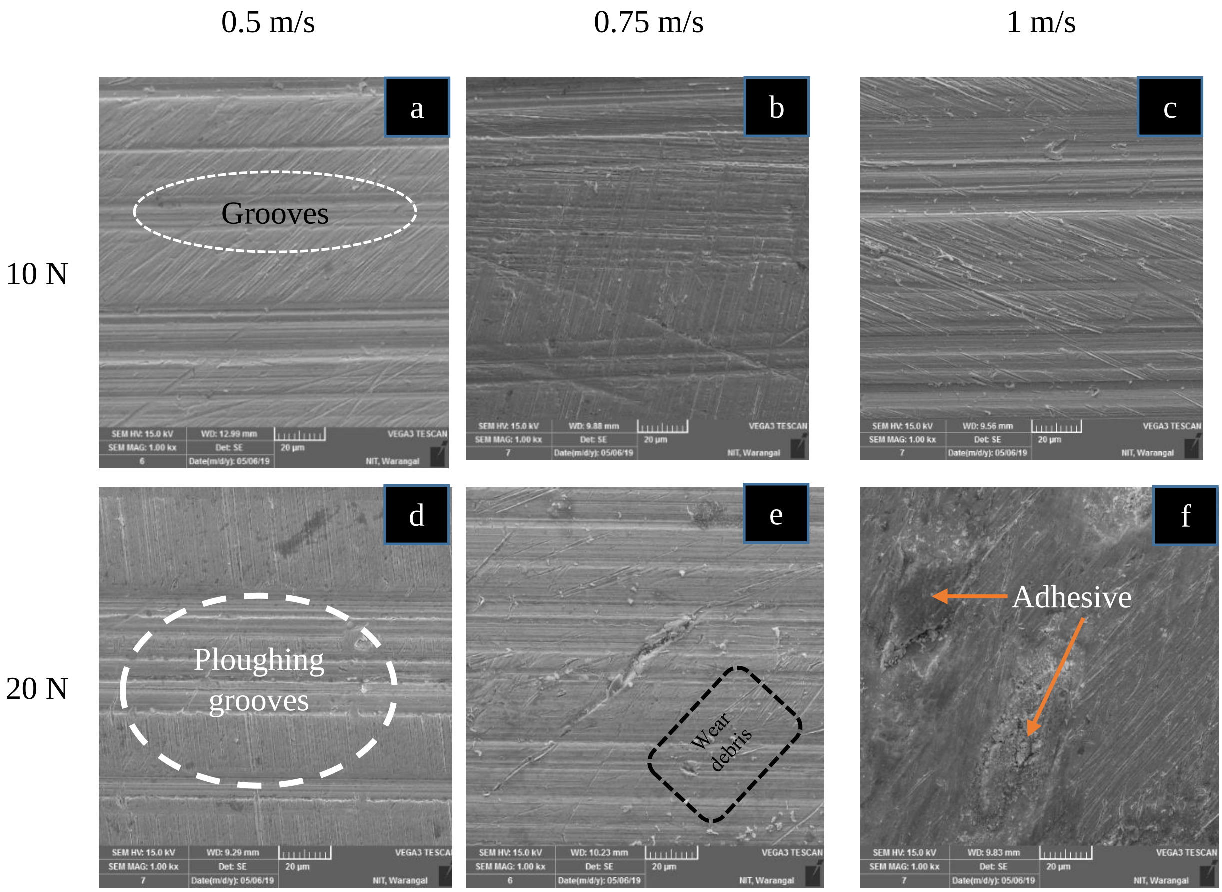

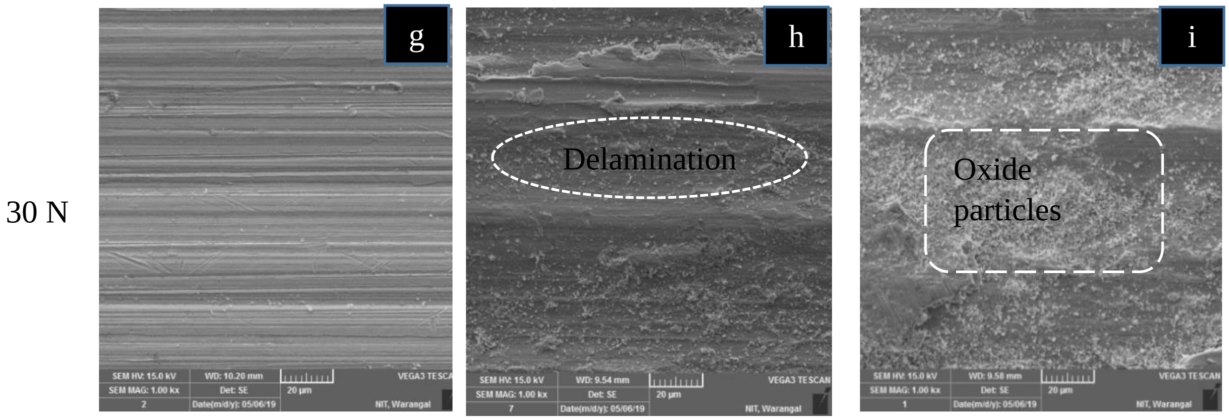

Figure 5.11 SEM images of wear track surface morphology during wear test under different sliding velocity and normal load

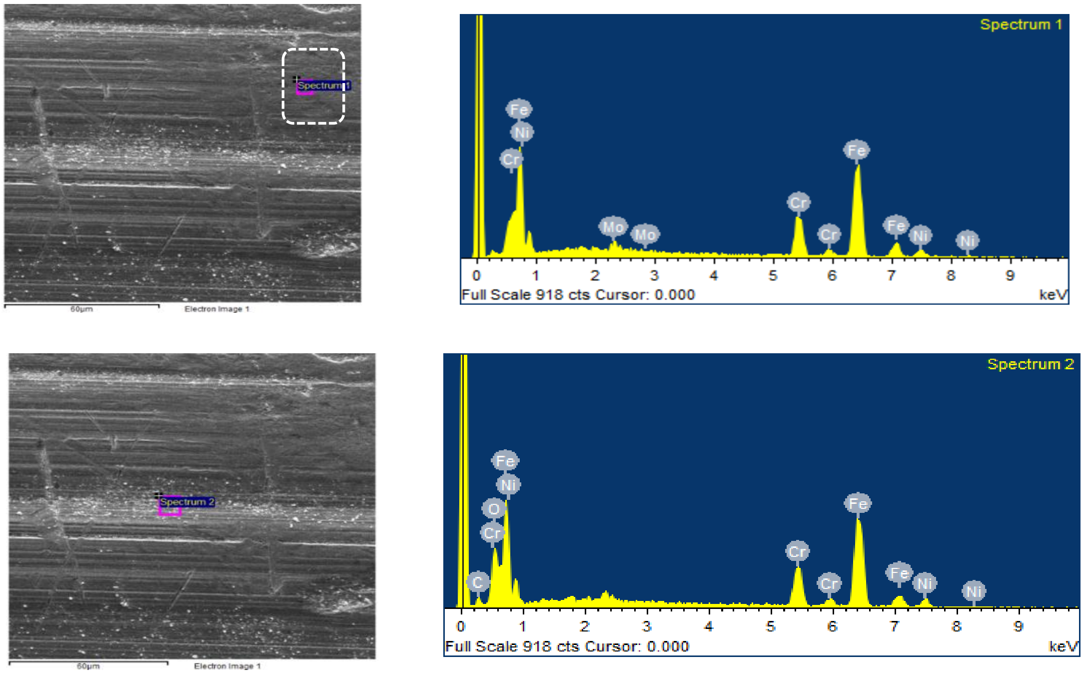

Figure 5.12 EDAX of DED samples after wear analysis

The deep grooves and plastic deformation of wear tracks are noticed at high sliding velocity and normal load. It can be attributed to aggressive abrasive wear mechanism up to certain time of duration, thereafter plastic deformation due to adhesive wear during dry wear test analysis. At higher sliding velocity, surface roughness of wear tracks is more severe and long, thin and bumpy areas would be erased. When sliding velocity increases, high kinetic energy is developed at the interface of test sample and disc. Subsequently, some part of the energy is converted into thermal energy and this leads to material softening. Therefore, easy removal of soft material is noticed especially at high normal load. The presence of oxygen was noticed at different locations (refer Figure 5.11h and 5.11i), in turn, reduces the direct metal-to-metal contact. Consequently, a reduction in COF is noticed with an increase in sliding velocity and normal load owing to oxide layer formation which acts as a lubricant. The presence of oxide particles is more significant and appears like white particles especially at high sliding velocity and normal load, and it is further confirmed by EDAX analysis as shown in figure 5.12.

5.6 Summary

Columnar dendritic growth is identified in microstructure analysis and it is observed that the minimum dendritic size is 6.11µm at scanning speed of 0.6 m/min. From XRD analysis, it is observed that austenite and ferrite phase are noticed under three scanning speeds, but ferrite phase is most significant at high scanning speed. The maximum value of average hardness of 317 HV is obtained at low scanning speed of 0.4 m/min and also hardness values of DED samples lies between the conventional sample and LPBF. In addition, tribological performance of SS316 is carried out under different normal load and sliding velocity. It is deduced from tribology studies that as the sliding velocity increases, the rise in specific wear rate is noticed with different normal loads. The minimum and maximum of specific wear rate of SS316 is $0.02497 \times 10^{-4}\mathrm{mm}^3/\mathrm{Nm}$ and $0.295 \times 10^{-4}\mathrm{mm}^3/\mathrm{Nm}$ respectively under normal load of 10N. The maximum percentage of specific wear rate is increased by 154% and 181.2% when sliding velocity is increased from 0.5 to 1 m/s and normal load from 10N to 30N respectively under three different scanning speed. Apart from this, the increase in specific wear rate is observed when SS316 samples built at scanning speed above 0.4 m/min. The decrease in COF is noticed with high sliding velocity due to oxide layer formation. From SEM analysis, scratches, fine wear debris and grooves parallel to the sliding direction are observed. These are all indications for aggressive abrasive wear as the major wear mechanism and it is mainly due to repetitive sliding on the counter surface on the SS316.

Chapter-6

Effect of post heat treatment conditions on DED built SS 316

6.1 Introduction

In the previous chapter, microstructure characterisation, hardness and tribological studies of DED built SS 316 bulk samples is carried out at different scanning speed. Considering the low porosity percentage and high hardness, DED built SS 316 at laser power of 1000 W, scan speed of 0.4 m/min and powder feed rate of 8 g/min is used for heat treatment analysis. Solution treatment of DED built SS 316 improved the homogeneity in microstructure, increased the plasticity retaining capability and elongation. Microstructure, hardness, automatic ball indentation test, corrosion and tribological study are carried out at different heat treatment temperatures.

6.2 Microstructure

The microstructure of as-built SS 316 and heat-treated samples at different temperatures are presented in figure 6.1. The microstructure is primarily cellular and dendritic in nature for as-built samples as shown in figure 6.1a, due to the higher thermal gradient between the substrate and deposit. The growth is mainly columnar in nature, opposite to the heat transfer direction. The growth is finer in nature which can be attributed to the higher cooling rate during DED process. It can be seen in figure 6.1b and 6.1c that columnar dendrites are dissolved after heat-treatment at HT1073 and HT1273. The microstructure is observed to be more uniform without any directional growth. The microstructure is dominant with austenite phase having face centered cubic (FCC) structure and finely dispersed low volume fraction of ferrite structure with body centered cubic structure [78,82,84]. The presence of chemical elements such as Cr, Si and Mo are mainly conductive for ferrite formation in austenitic stainless steels [130]. SEM images presented in Figure 6.2 also confirm the reduction in ferrite phase with an increase in the heat treatment temperature and similar observations are seen in the literature for similar materials [82,88,130].

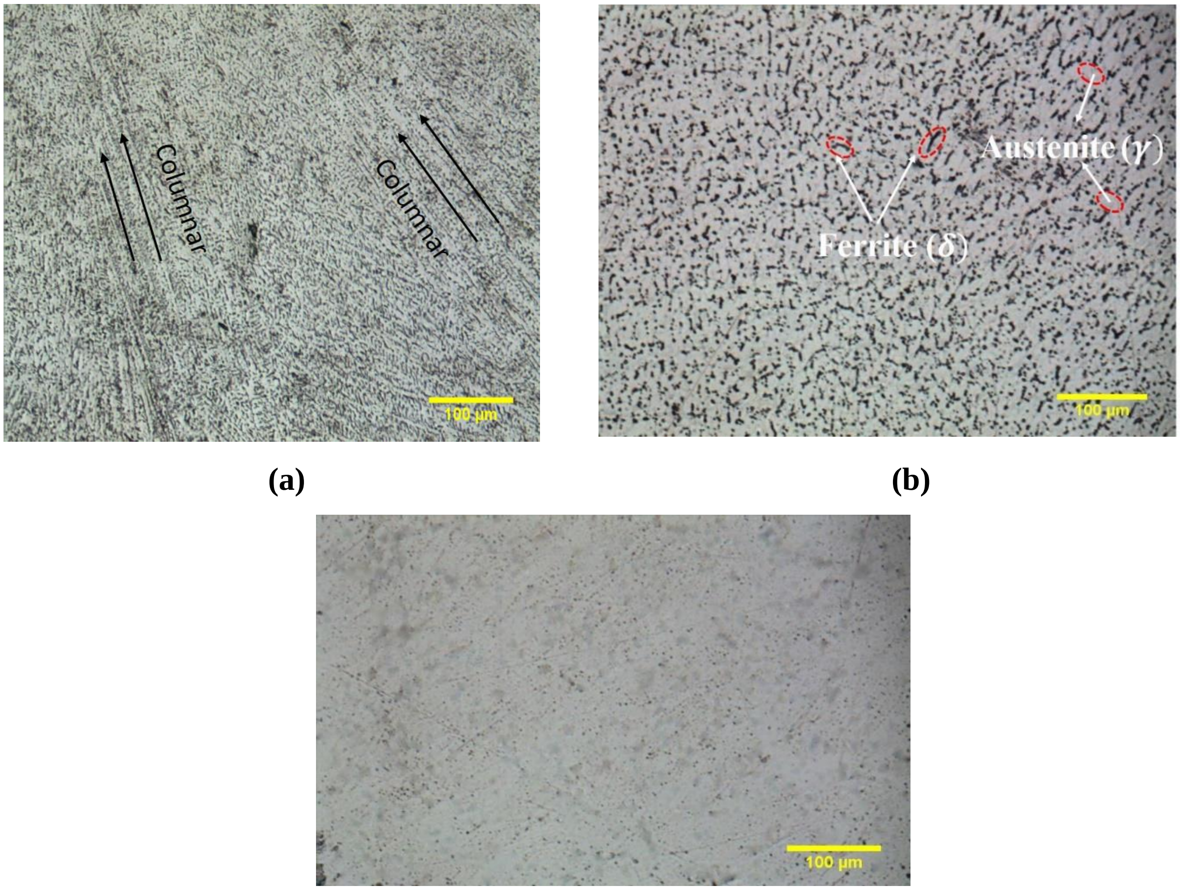

(a) **(b)**

(c)

Figure 6.1 Microstructure of SS 316 at different conditions (a) As-built (b) HT1073 (c) HT1273

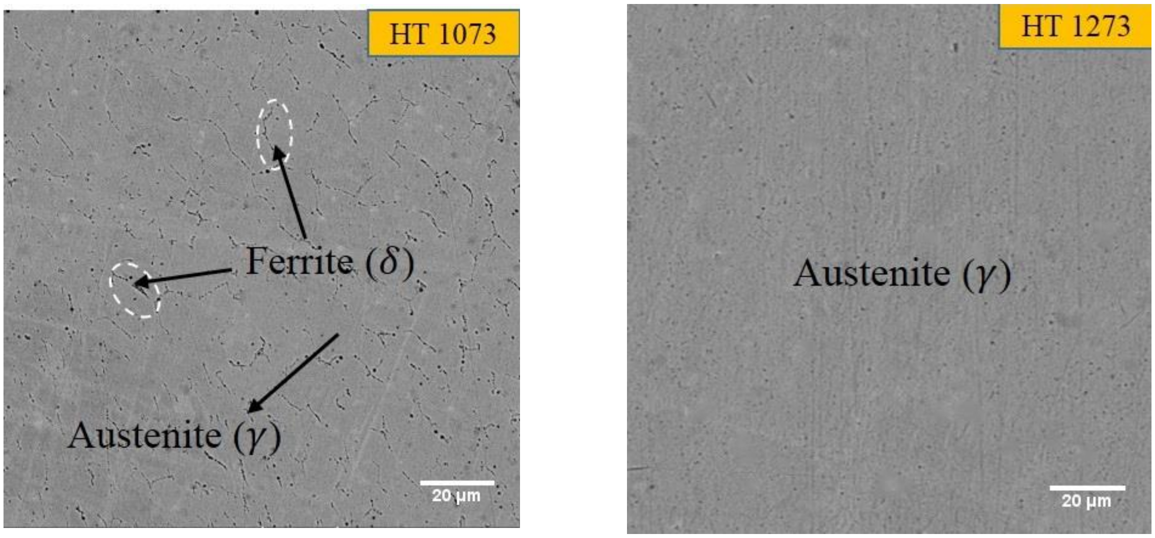

(a) (b)

Figure 6.2 SEM images of SS 316 at different conditions (a) HT1073 (b) HT1273

6.3 XRD analysis

XRD analysis is carried out in as-built and heat-treated samples (HT1073 and HT1273) as shown in figure 6.3. The austenite phase is relatively dominant at all conditions, while reduction in the ferrite phase with increasing heat-treatment temperature is noticed. The volume fraction of ferrite phase for as built, HT1073 and HT1273 samples is 7%, 4.38%, 0.83%, respectively and the decreasing trend in the volume fraction of ferrite phase also agrees with microstructural observations discussed earlier.

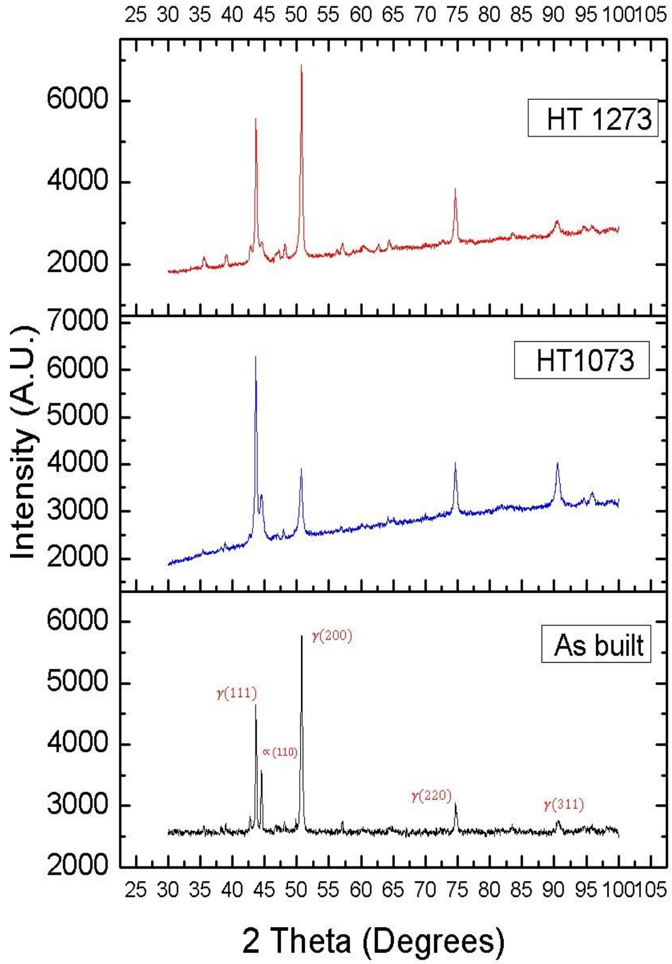

Figure 6.3 XRD pattern for SS 316 samples at different conditions

The average crystallite size of as-built, HT1073 and HT1273 is found out to be 26.741 nm, 27.39488 nm and 32.40242 nm. It can be ascribed to an increase in grain size and coagulation or coalesce of the particles during heat-treatment [131]. In addition, the peak position of $\gamma(111)$ at HT1073 and HT1273 is shifted towards 0.02721^0 and 0.00272^0, respectively with regard to peak position in the as-built sample. It can be due to the variation in residual stresses after heat-treatment conditions.

6.4 Micro-hardness

Figure 6.4 presents the variation in the micro-hardness along the cross-section of as-built and heat- treated samples. The average micro-hardness of as-built sample is $311_{0.98\ \mathrm{N}}$ HV, due to high cooling rates and resulting finer microstructure. The average micro-hardness of HT1073 and HT1273 samples are 296 and 294 HV, respectively. The micro-hardness of heat-treated samples is reduced by 4.8% and 5.5% in HT1073 and HT1273 K, respectively as compared to as-built samples. It can be attributed to increase in the crystallite size and homogenization of grain structure with temperature. In addition, it agrees with the halls patch relation (refer equation 6.1), which implies that the average grain size of the sample inversely proportional to the hardness of the material. Further, the reduction in hardness can also be attributed to the reduction in the amount of ferrite phase with an increase in heat-treatment temperature as the ferrite phase is harder than the austenite phase [130]. This is in line with the XRD and microstructural analysis.

$$H = H_0 + \frac{K}{\sqrt{d}} \tag{6.1}$$

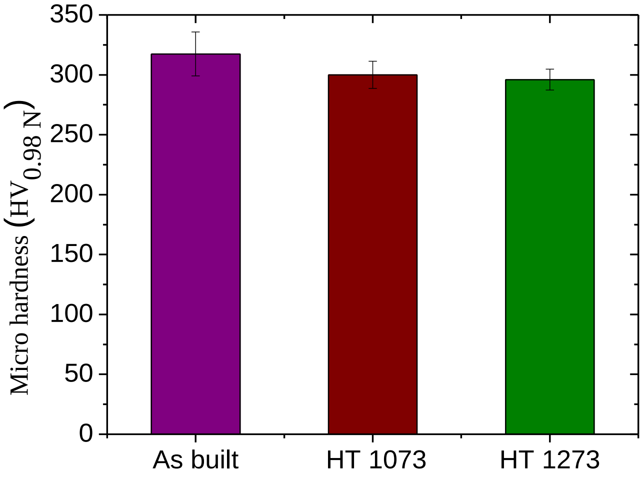

Figure 6.4 Variations of Micro hardness at different heat-treatment temperature

6.5 Automatic ball indentation test

Figure 6.5 presents the load-displacement curve for DED samples before and after heat-treatment. The maximum displacement for as-built, HT1073 K and HT1273 K samples are found to be 0.079 mm, 0.10 mm and 0.11mm, respectively. The increase in displacement indicates that the depth of indentation increased with heat-treated samples under the same loading conditions, which is primarily due to reduction in material hardness. It can be due to coarsening of microstructure and reduction in the ferrite phase, which is harder than the austenite phase. The typical indentation images of ABI test for as-built and heat-treated conditions as shown in figure 6.6. A slight increase in the indentation diameter is observed for heat-treated samples as compared to as-built samples. Further, the diameter also increased with increase in heat-treatment temperature. This increase in the indentation diameter can be attributed to grain coarsening with heat treatment temperature. The observed results are also in line with the micro-hardness and microstructure results. The area under the curve gives the plasticity retaining capability of the material. The energy stored in as-built, HT1073 and HT1273 samples are 1.254 N-mm, 1.824 N-mm and 2.167 N-mm, respectively. The plasticity retaining capability of HT1073 and HT1273 improved by 45.4% and 72.8% as compared to that of the as- built DED sample. It can be due to reduction in the volume fraction of ferrite and increasing grain size with heat-treatment.

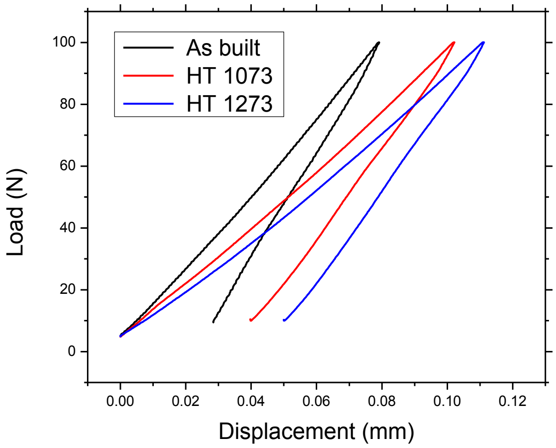

Figure 6.5 Load displacement for SS 316 under varying heat-treatment during ABI test

141.660 µm 145.956 µm 151.325 µm

Figure 6.6 Typical indentation of SS 316 samples during ABI test

6.6 Corrosion test

Figure 6.7 presents the tafel curves of as-built and heat-treated SS 316. The corrosion rate is directly proportional to the corrosion current density (I_{corr}) obtained during electro chemical analysis. It is observed that the metal dissolution rate (corrosion rate) of as-built SS 316 is too low compared to SS 316 sample manufactured by the conventional process as shown in Table 6.1. Similar observations are made by previous researchers on SS 316L [132].

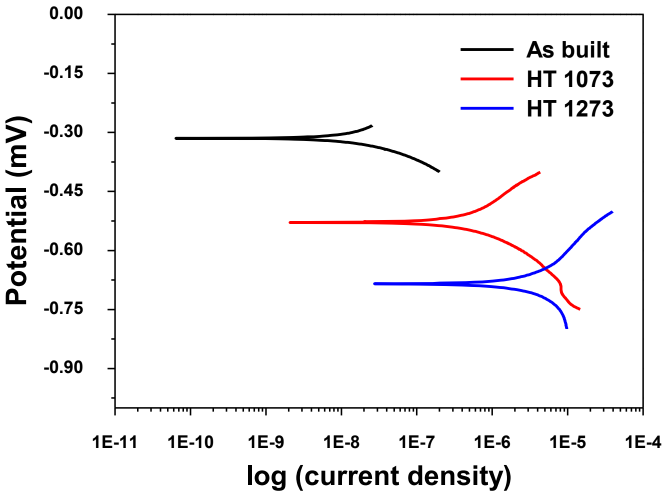

Figure 6.7 Tafel curves for the as-built and heat-treated SS 316 samples

The corrosion rate is observed to increase with an increase in solution treatment temperature. It can be attributed to a decrease in ferrite phase with heat treatment temperature as shown in the SEM images presented in figure 6.2. The austenite phase is more prone to corrosion rate than the ferrite phase which is more rich in chromium [133–135].

Table 6.1: Electro chemical behavior of as-built and heat-treated SS 316

Sl. No.	**Sample**	**Open circuit potential (mV)**	**Corrosion rate C.R. (mpy)**	**Corrosion potential Ecorr (mV)**	**Corrosion current desnity Icorr (µA)**	**Anodic Tafel constant β_A (mV)**	**Cathodic Tafel constant β_c (mV)**
1.	As-built	-254.68	0.0008247	-313.904	2.01E-3	11.14	13.76
2.	HT 800	-486.27	0.09	-525.189	227.80E-3	94.52	75.84
3.	HT 1000	-638.693	0.699	-688.369	1.704	104.36	89.37
4.	Conventional SS 316 [84]	-	-	-208	1.7 (mA/cm^2)	-	-

6.7 Tribology

The variation in specific wear rate of as-built and heat-treated SS 316 samples are analyzed using pin on disc tribometer. Figure 6.8a presents the variation in specific wear rate with heat-treatment temperature. The minimum specific wear rate is observed in the as-built sample, due to high micro hardness and fine grain structure. An increase in specific wear rate is noticed with an increase in heat-treatment temperature, due to increase in grain size and dislocation density [85]. The reduction in volume fraction of ferrite phase with heat treatment which is confirmed by SEM images and XRD plots, lead to low micro-hardness values as ferrite phase is harder than the austenite [86]. In contrast, it can be noticed from figure 6.8b that the coefficient of friction (COF) increased with increase in heat-treatment temperature and it can be ascribed to coarse grain structure and low hardness [136]. The SEM images of worn surfaces of as-built, HT1073 and HT1273 are presented in figure 6.9. The wear debris and ploughing grooves parallel to sliding direction are observed for as- built DED samples as shown in figure 6.9a. The abrasive wear is major mechanism in as- built SS 316 sample, whereas heat-treated samples are characterized by abrasive and adhesive wear.

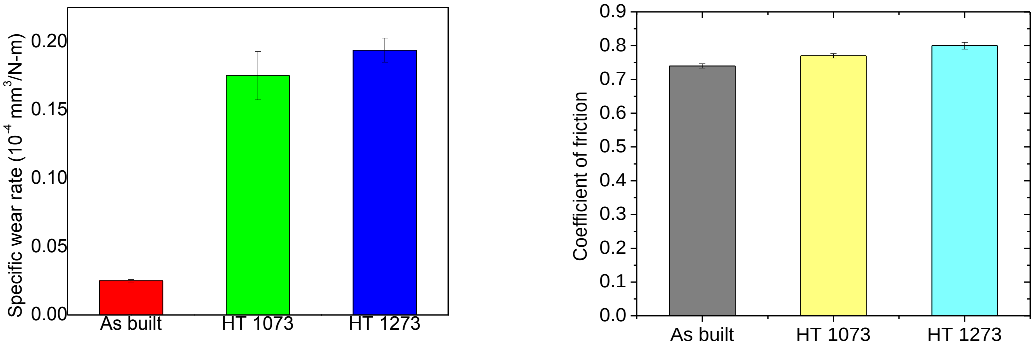

(a) (b)

Figure 6.8 Variations of (a) specific wear rate and (b) coefficient of friction under different heat-treatment conditions

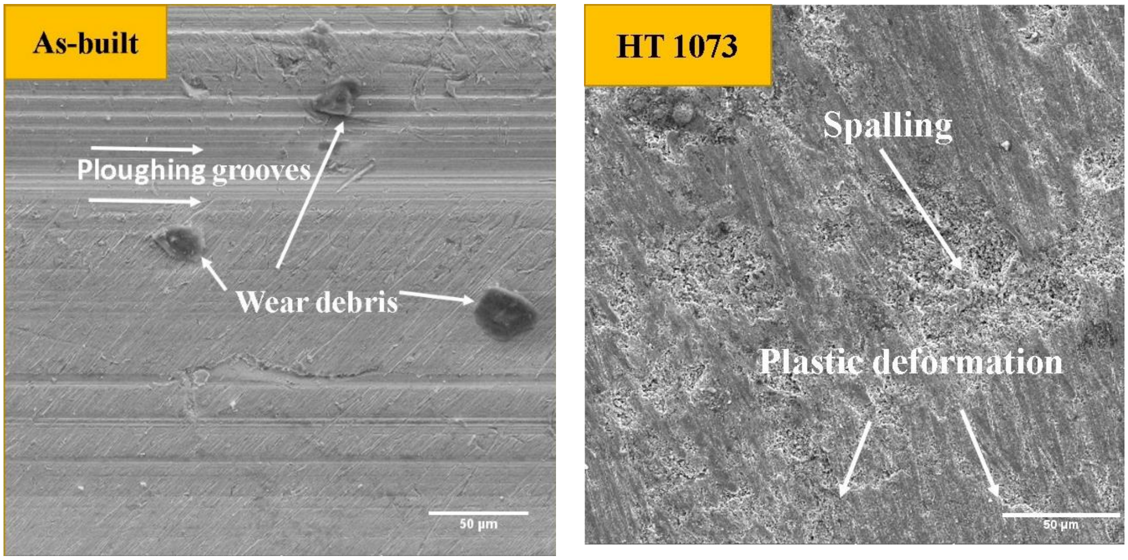

(a) **(b)**

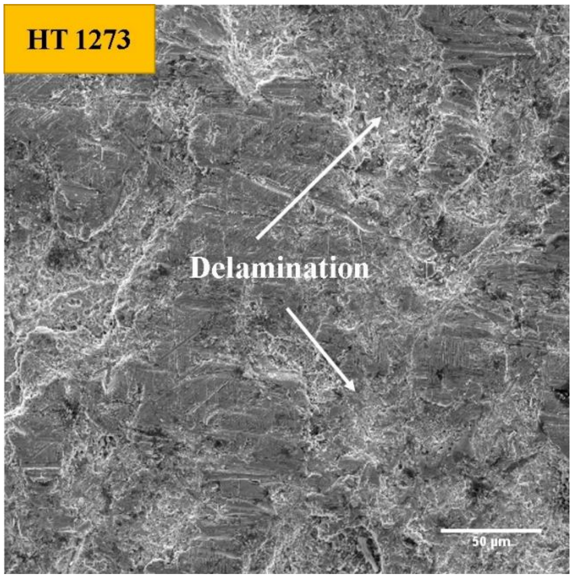

(c)

Figure 6.9 Variations of specific wear rate and coefficient of friction under different heat-treatment conditions

The plastic deformation followed by spalling and delamination effect are observed along the sliding direction of heat-treated samples as shown in figure 6.9b and c. It can be attributed to low volume fraction of ferrite in heat treated samples as seen in the SEM and XRD studies. The surface is subjected to plastic deformation, and subsequently sheared and then ruptured, which lead to micro cracks, resulting in periodic spalling effect. The deep and wider grooves are identified in heat-treated samples as compared to as-built samples, due to low strain hardening effect [71] , reduction in density of ferrite phase and low micro hardness.

6.8 Summary

Columnar growth is observed to be dissolved with heat-treatment and the reduction in fraction of ferrite phase is noticed with heat-treatment, especially at HT1273. It is observed from XRD that the crystallite size increased with heat-treatment and the minimum crystallite size is found to be 24.886 nm for as-built DED sample. The austenite phase is relatively dominant at all conditions, while reduction in the ferrite phase with increasing heat-treatment temperature is noticed. The volume fraction of ferrite phase for as built, HT1073 and HT1273 samples is 7%, 4.38%, 0.83%, respectively. It is observed from ABI studies that the maximum displacement of 0.11 mm is observed at HT1273. The plasticity retaining capability of heat-treated SS 316 sample at HT1073 and HT1273 is increased by 40.4% and 72.8%, respectively as compared to as-built samples. This can be attributed to grain coarsening and reduction in ferrite phase with increase in heat treatment temperature. The hardness of as-built SS 316 samples reduced by 5.47 % after heat-treatment and it can be attributed to grain coarsening and reduction in ferrite phases with increase in heat treatment temperature. The minimum hardness of 294 HV is noticed at HT1273. The corrosion rate of as-built SS 316 is too low compared to corrosion rate of SS 316 samples fabricated through conventional route. The corrosion rate of SS 316 increased with heat-treatment temperature, owing to reduce the ferrite phase with heat treatment temperature. The increase in specific wear rate of SS 316 samples with heat-treatment temperature is observed and minimum specific wear rate of 0.02497 x 10^{-4} mm^3/N-m is obtained for as-built sample. The COF increased with heat-treatment and it can be attributed to coarse grain size and low hardness. The plastic deformation, spalling and delamination effect are major wear mechanism of heat-treated samples due to low volume fraction of ferrite phase in heat treated samples.

Chapter-7

Characterization of DED built SS 316-WC composites at different volume fraction of WC

7.1 Introduction

In the previous chapter, characterization of DED built SS 316 is carried out at different heat treatment temperatures. In this chapter, parametric investigation for SS 316-WC composites is performed at laser power of 1000 W, different scanning speed of 0.4, 0.5 and 0.6 m/min and powder feed rate of 8 g/min. Different volume fraction of WC reinforcement particles are mixed in SS 316 to enhance the grain refinement and hardness of SS 316. The optimum process parameter combination is noticed based on the uniform WC reinforcement particle distribution without any defects. Characterization of DED built SS 316-WC composites at different volume fraction of WC.

7.2 Process parameter selection

Initially, single tracks are laid by varying scanning speed to understand the behavior of WC particles in SS 316 composite at a constant laser power of 1000 W and powder feed rate of 8 g/min. The variation in cross section of track geometry is observed at laser power of 1000 and scanning speed of 0.4, 0.5 and 0.6 m/min at constant powder feed rate of 8 g/min as shown in figure 7.1.

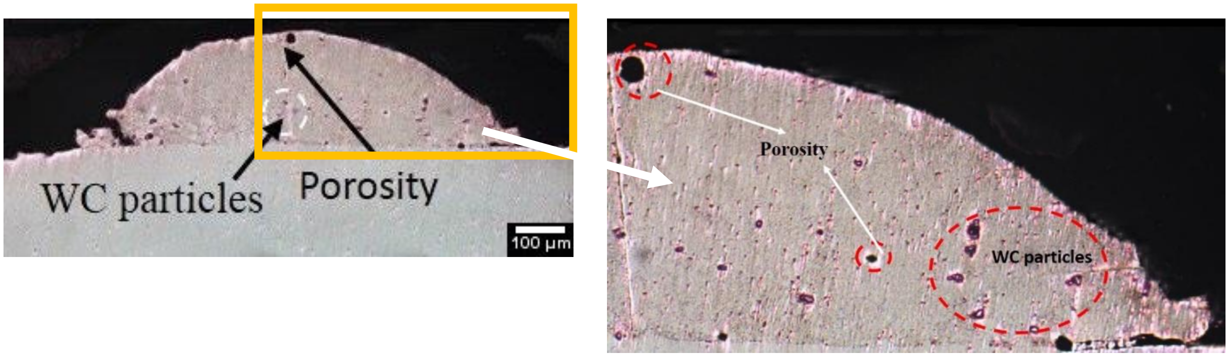

(a)

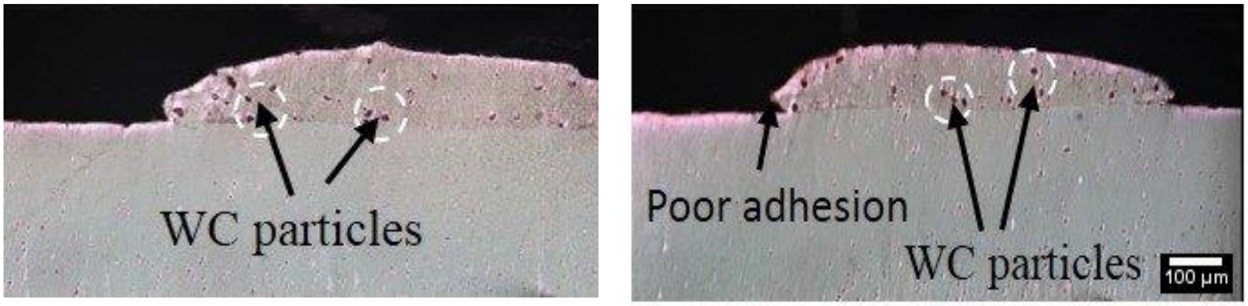

(b) (c)

Figure 7.1 Cross sectional view of single track composites (% 10 WC) at constant laser power of 1000 W and different scanning speed (a) 0.4 m/min (b) 0.5 m/min (c) 0.6 m/min

The uniform distribution of WC particles is noticed at laser power of 1000 W at different scanning speeds (0.4, 0.5 and 0.6 m/min). However, at laser power of 1000 W, scanning speed of 0.4 m/min results in porosity and scanning speed of 0.6 m/min results in poor adhesion with the substrate. The porosity generation is mainly due to higher laser energy per unit length at scanning speed of 0.4 m/min, while the lower laser energy per unit length at scanning speed of 0.6 m/min results in poor adhesion with the substrate. Thus, the chosen parameters for bulk deposition are laser power of 1000 W and laser scanning speed of 0.5 m/min considering the uniform distribution of WC and minimal porosity.

7.3 Relative Density

Figure 7.2 presents the relative density of DED built composites at a different fraction of WC and compared with SS 316 structure without WC. The maximum relative density is detected for SS 316 as compared to composites and it can be attributed to low bulk defects, like - porosity, voids. The chemical reactions between different powder particles, shrinkage during solidification and atmospheric gas entrapment resulted in low relative density for developed composites [137,138]. In addition, relative density decreased with an increase in the composition of WC in SS 316 and it can be ascribed to porosity and cracks formation as shown in figure 7.3d. Particularly at a high percentage of WC. Similar observations are noticed by Manowar Hussain et al. [137].

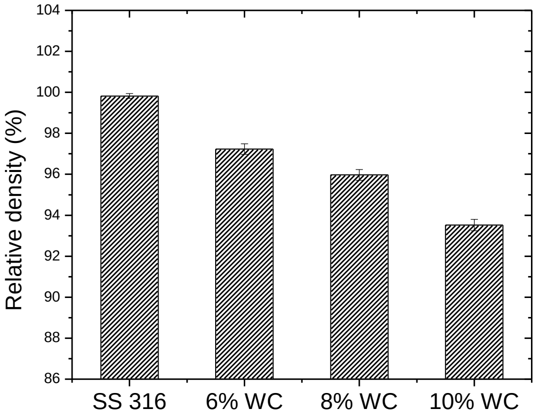

Figure 7.2 Relative density of DED SS 316 structures and SS 316-WC structures at different WC fraction.

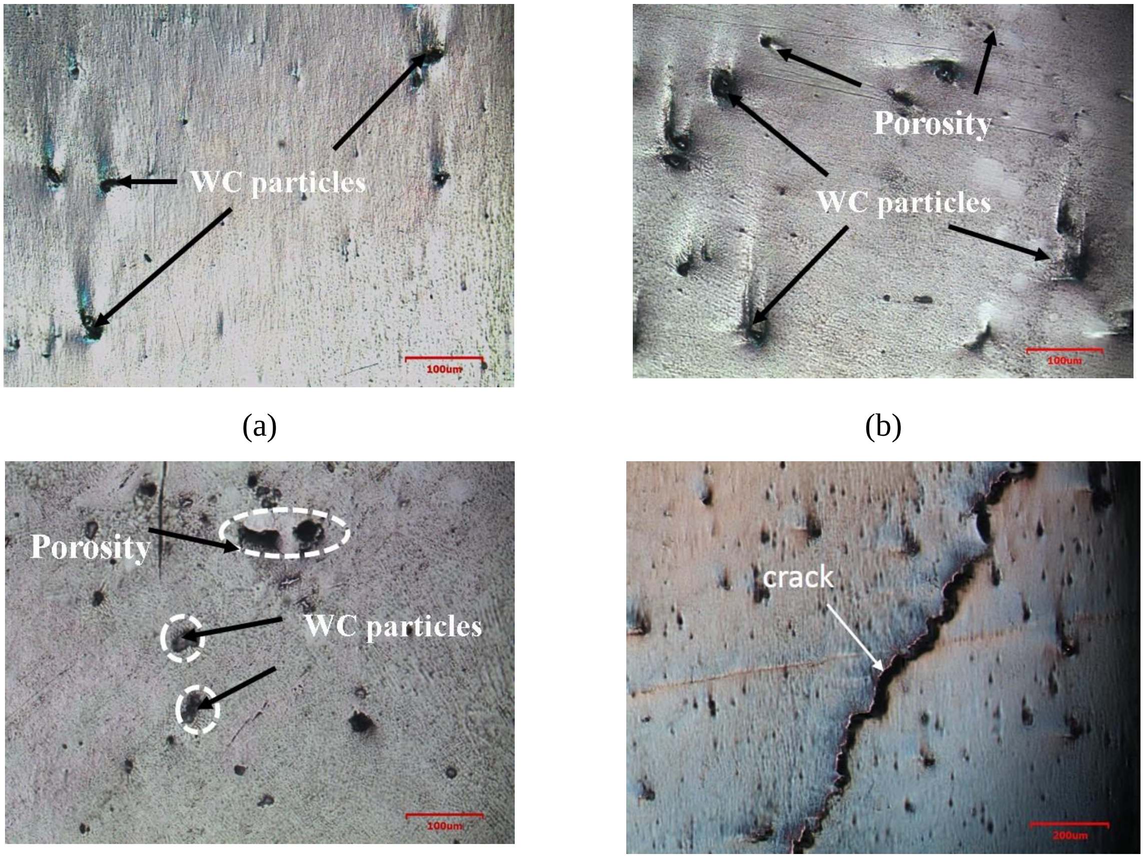

(a) (b)

(c) (d)

Figure 7.3 Optical imcroscopic images of SS 316 composite with (a) 6% WC (b) 8% WC (c) 10% WC and (d) Crack formation

7.4 X-ray Diffraction

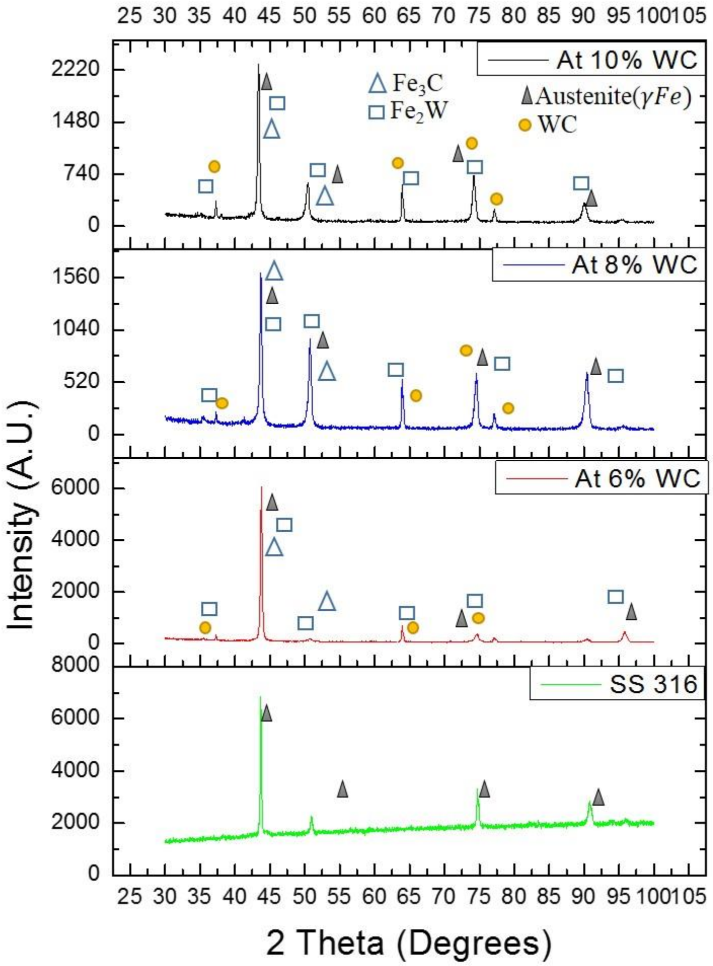

Figure 7.4 XRD spectrums of SS 316 and its composites at different WC percentage

Figure 7.4 presents the XRD patterns for varying percentage of WC (6%, 8% and 10%) in SS 316 based composites. XRD spectra of the composite reveals the presence of WC, γFe, Fe_2W and Fe_3C phases. The WC is partly dissolved into W and C and react with iron during DED process, which results in the formation of Fe_2W and Fe_3C phases. Highest intensity is observed for the peaks corresponding to the austenite phase (FCC), whereas weak diffraction peaks with WC particles are detected. The intensity of WC peaks increased with an increase in the WC composition. The crystallite size is calculated by using Scherrer equation 7.1, where λ is wave length of X-ray source, C is Scherrer constant (0.9), θ is peak position in radians and β is full width at half maximum in radians. The average crystallite size is found to be 23.80 nm, 21.78 nm and 18.82 nm at 6, 8% and 10% volume fraction of composite respectively. It is observed that the crystallite size reduced with an increase in the volume of fraction of WC and it can be attributed to more grain refinement and dislocation density. The highest intensity peak is identified at 2 Theta= 43.71702^0 under 6 % volume fraction of composite which is reflection of γFe phase. The position of austenite phase is shifted towards left to 43.70483^0, 43.70451^0 and 43.38266^0 with reference to peak position (43.71449^0) of SS 316 sample. As per Bragg's law equation (refer equation 7.2), a peak shift to the left side indicates an increase in the distance between lattice planes, which shows the presence of tensile residual stresses on the built samples. It can be concluded that the tensile stresses increased with an increase in the WC content in SS 316. These results are in line with previous literature [96].

$$d = \frac{C\lambda}{\beta \cos\theta} \tag{7.1}$$

$$2d \sin\theta = n\lambda \, (n = 1,2,3 \ldots\ldots) \tag{7.2}$$

7.5 Microstructure

Figure 7.5 demonstrates the microstructure of SS 316 based composite at different WC composition. SEM images in back scattered mode shows the presence of WC (White particles) and pores (Black dots) in DED built SS 316 composites as shown in figure 7.5. The adequate distribution of WC in SS 316 matrix can be observed in the DED built composite. The columnar dendritic and cellular grain structure are observed for 6% WC as shown in figure 7.5a whereas columnar and equiaxed dendritic are more significant in 8% WC and 10% WC as shown in figure 7.5b&c. The measured dendrite size of 6% WC, 8% WC and 10% WC is 6 μm, 4.01 μm and 3.25 μm, respectively. The reduction in the dendrite size with an increase in the WC content in SS 316 matrix is ascribed to the fact that WC behave like heat sinks and also helps in intensifying dislocation density. The presence of WC in SS 316 improves the grain refinement resulting in a denser and uniform microstructure. It might have attributed to excellent wettability of WC with SS 316 matrix [139].

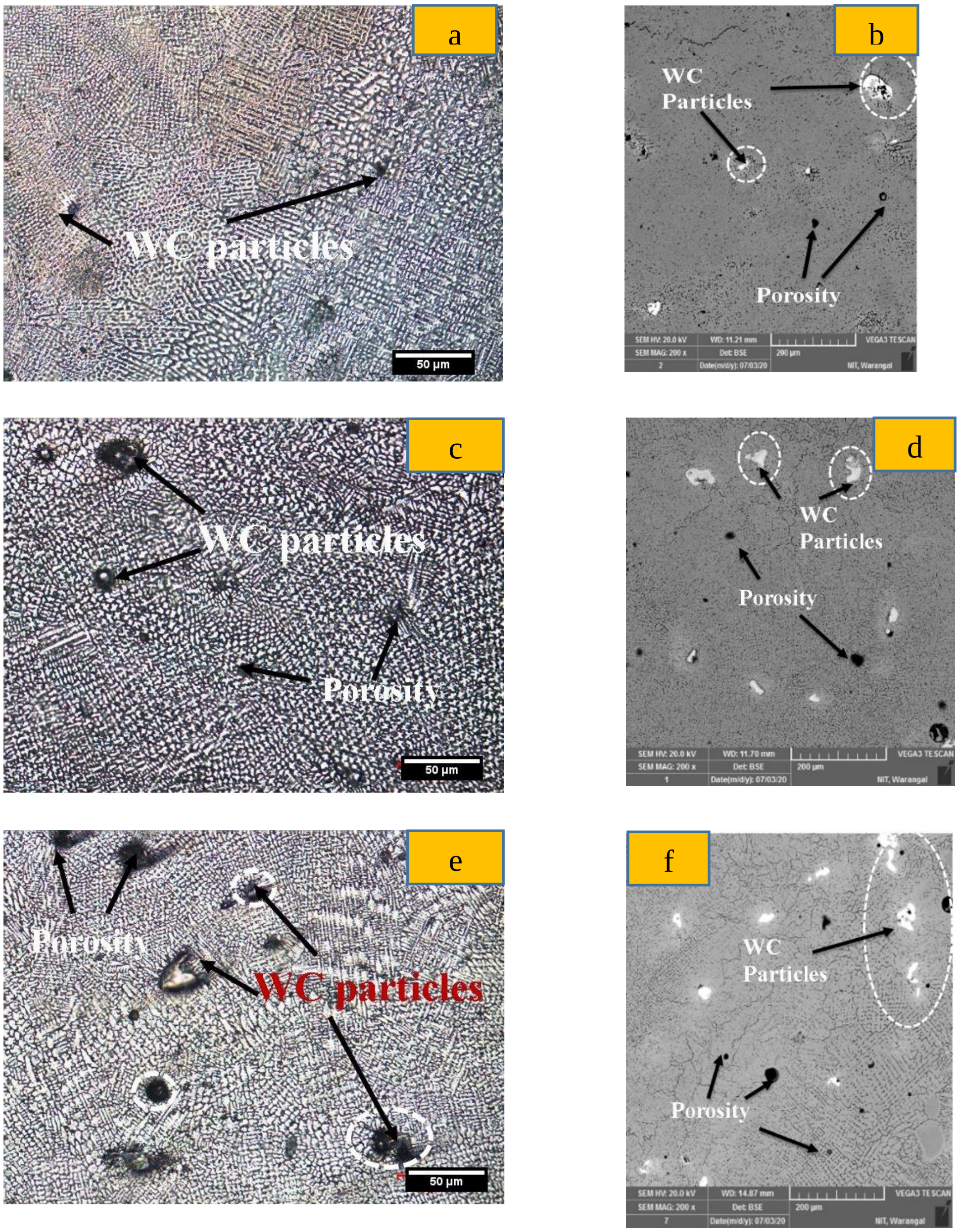

Figure 7.5 Illustrate the optical and SEM images at different concentration a,b) 6% c,d) 8% and e,f) 10% of tungsten carbide in SS 316

7.6 Micro hardness

Figure 7.6 shows the significant improvement in the hardness of SS 316/WC composite as compared to SS 316 built using DED process. The micro hardness of DED built SS 316 and SS 316L substrate are 279 HV and 212 HV respectively. The maximum hardness of 399.5 HV is obtained for samples built with 10% WC and hardness of samples with 6% WC and 8% WC are 321 and 352 HV, respectively. The uniform distribution of WC particles restricts the grain elongation, which results in fine microstructure.

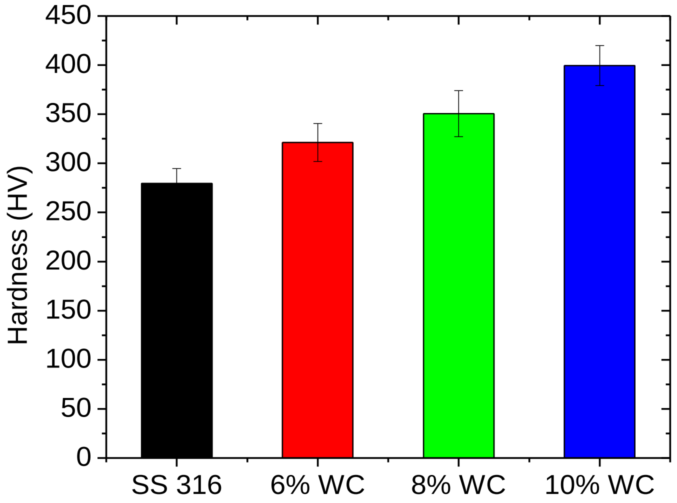

Figure 7.6 Demonstrate the variation of hardness with different concentration of tungsten carbide in SS 316

This increases the hardness of bulk composite samples. As discussed in the previous section, high percentage of WC reinforcement particles in SS 316 increases the cooling rate, which leads to finer grains and higher dislocation density. In addition, the dissociation of WC in to W and C element under high laser power tends to solid solution strengthening effect in SS 316 matrix, and consequently leads to higher hardness [140]. The resistance against plastic deformation can be achieved by adding stronger and stiffer reinforcement in metal matrix which results in increased hardness of composites during micro-hardness test [141].

7.7 Corrosion test

Figure 7.7 presents the potentiodynamic curves of SS 316 and its composites. Table 7.1 presents the various parameters associated with the potentiodynamic study. The low corrosion rate is noticed at 8% WC as compared to 6% WC, 10% WC and SS 316 samples, which is confirmed by the lower I_{corr} values. The increase in corrosion resistance with addition of WC in SS 316 is due to high corrosion resistance of WC as compared to SS 316 [142] . However, corrosion rate of 10% WC is higher than 8% and 6% WC and it can be attributed to the presence of macro pores and cracks resulting in early pit initiation. Similar observations are also reported in the literature [143].

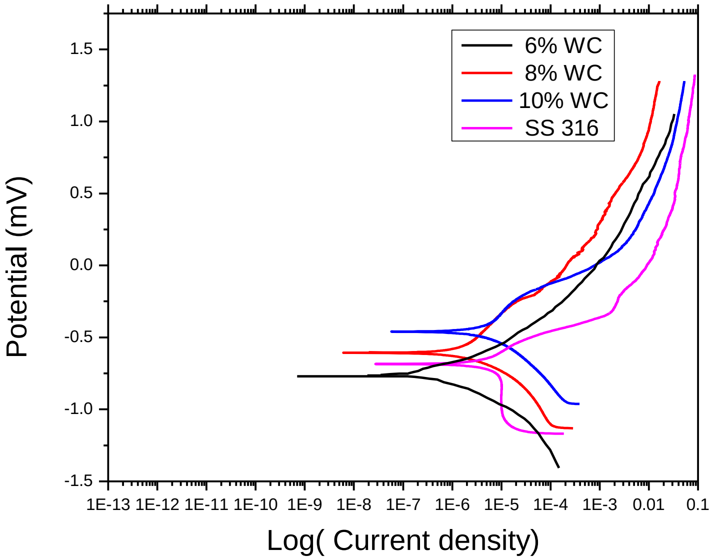

Figure 7.7 Potentiodynamic polarization curves of SS 316 and its composites (6%, 8% and 10% WC)

Table 7.1: Electro chemical behaviour of SS 316 and its composites

	E_{Corr}(mV)	β_a(V)	β_c(V)	$I_{Corr}(\frac{\mu A}{cm^2})$
SS 316	-616	0.162	0.234	3.5
6% WC	-612	0.183	0.796	2.31
8% WC	-463	0.095	0.169	1.47
10% WC	-683	0.165	0.187	2.42

7.7 Tribology

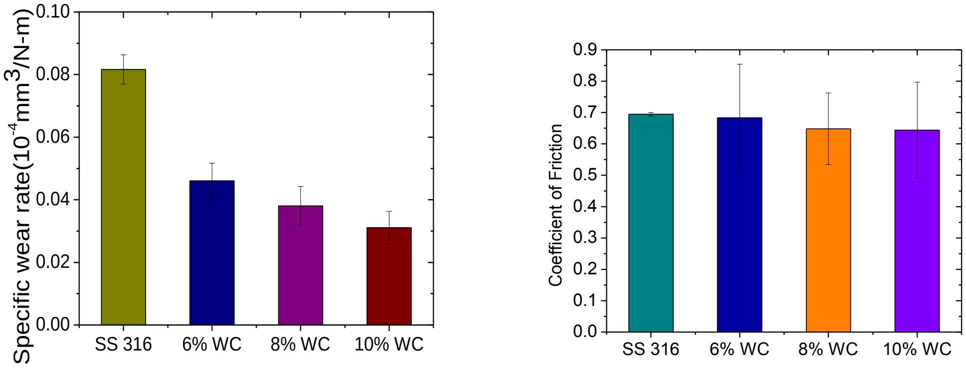

(a) (b)

Figure 7.8 Variation of a) specific wear rate b) COF at different concentration of WC

The specific wear rate (SWR) of composite at different volume fraction of WC in SS 316 built by DED process is shown in figure 7.8a, which shows an improvement in the tribological properties of SS 316 with addition of WC particles. The SWR reduced with an increase in the WC percentage in SS 316/WC composite. The minimum SWR of $0.03107 \times 10^{-4} \frac{mm^3}{N-m}$ is obtained at 10% WC in SS 316 based composite and it can be attributed to higher hardness, dislocation density and fine grain size at higher WC concentration [144]. Coefficient of friction (COF) reduced with an increase in the WC content in SS 316 matrix as shown in figure 7.8 b. The excellent self-lubricant properties of WC might have led to lower COF values with an increasing WC content [145]. Figure 7.9 presents the SEM images of surface morphology of worn out surfaces of SS 316/WC composites. The abrasive and plastic deformation are major wear mechanism in this study. The absence of adhesive wear and oxide layer formation is identified by EDAX analysis as shown in figure 7.9. The abrasive action started initially and after some duration it reduced because of lubricant properties of WC particles. As rubbing continued, wear debris are formed due to generation of high temperature. The deep grooves and plastic deformation are detected over the worn out surface at 6% concentration of WC in SS 316 composite. The shallow groove, wear debris and plastic deformation are observed on the worn out surfaces of composite at 8% and 10% of WC.

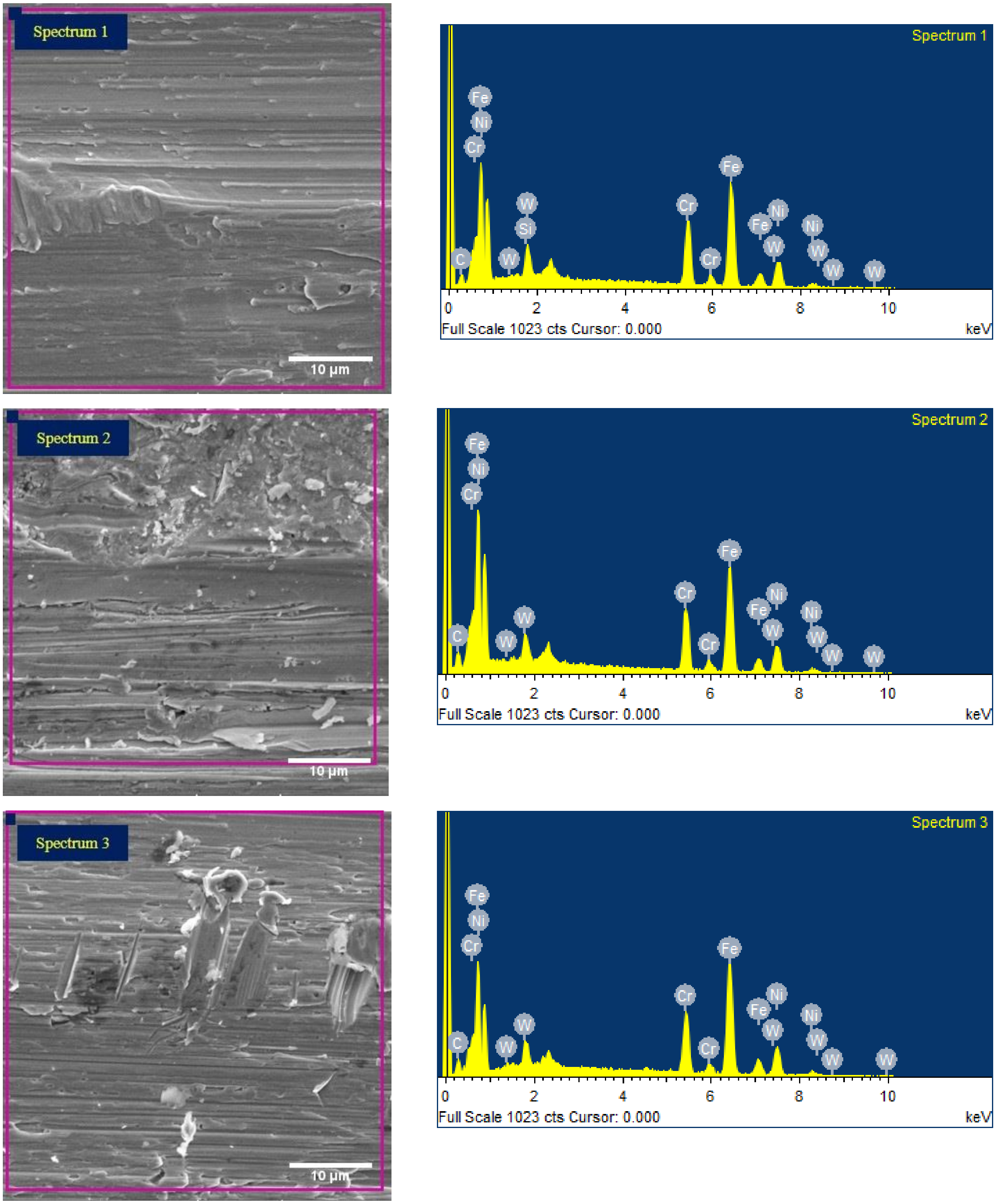

Figure 7.9 SEM images of surface morphology of worn out surfaces of SS 316/WC composites

7.8 Summary

The maximum relative density is noticed for SS 316 samples as compared to composite samples due to more porosity and crack formation during composite fabrication. The cellular, columnar dendritic structure is noticed for 6 and 8% of WC composites, whereas equiaxed dendritic structure is noticed for 10% of WC composite. From XRD analysis, WC, austenite phases are noticed and crystallite size is reduced by 21% when increasing WC content from 6% to 10%. In addition, WC, γFe, Fe_2W and Fe_3C phases are noticed in SS 316 composites. The hardness of 10%WC in SS 316 is increased by 26% as compared to SS 316, but high corrosion rate was noticed due to micro pores and crack formation. The wear resistance of 10%WC content is maximum and it is 61% higher than SS 316 because of its excellent lubricant properties and high hardness.

Chapter-8

CONCLUSIONS AND FUTURE SCOPE

8.1 Conclusions

Parametric investigation and characterization of SS 316 built by directed energy deposition DED are performed. A range of process parameters is selected using single tracks deposition by varying DED process parameters. The single track analysis is carried out using DED process at each parameter and obtained results are compared with finite element analysis. The effect of heat-treatment on the microstructure, mechanical, corrosion and tribological behavior is investigated. Relative density, microstructure analysis, micro-hardness and wear rate of DED built SS 316 based composites with different volume fraction (6%, 8% and 10%) of WC reinforcement are studied.

The following conclusions can be drawn from the obtained results.

- The identified process parameters are laser power of 1000 W, powder feed rate of 8 g/min and scanning speed of 0.4 m/min, 0.5 m/min and 0.6 m/min for maximum hardness and deposition rate. The effect of each DED process parameters on track width and height are studied with finite element analysis as well as experimental results. The results obtained during finite element analysis are close to experimental results, and the maximum percentage error is 9 %.
- From the XRD analysis, it is observed that austenite and ferrite phase are noticed at all the conditions, but ferrite phase is most significant at high scanning speed. The hardness values of DED samples lies between the conventional sample and L-PBF. Tribology studies show that, as sliding velocity increases, the rise in specific wear rate is noticed with different normal loads. The increase in specific wear rate is observed when SS 316 samples is built at scanning speed above 0.4 m/min.
- From the SEM analysis, scratches, fine wear debris and grooves parallel to the sliding direction are observed, which indicates that aggressive abrasive is the major wear mechanism and it is mainly due to repetitive sliding on the counter surface on the SS 316.

- Columnar growth is observed to be dissolved with heat-treatment and the reduction in fraction of ferrite phase is noticed with heat-treatment, especially at HT1273. It is observed from XRD that the crystallite size increased with heat-treatment and the austenite phase is relatively dominant at all conditions, while reduction in the ferrite phase with increasing heat-treatment temperature is noticed. The volume fraction of ferrite phase for as-built, HT1073 and HT1273 samples is 7%, 4.38%, 0.83%, respectively.
- The plasticity retaining capability of heat-treated SS 316 sample at HT1073 and HT1273 increased by 40.4% and 72.8%, respectively as compared to as-built samples. The hardness of as-built SS 316 samples reduced by 5.47 % after heat-treatment.
- The corrosion rate of SS 316 increased with heat-treatment temperature, owing to reduction in the ferrite phase with heat treatment temperature. The increase in specific wear rate of SS 316 samples with heat-treatment temperature is observed. The plastic deformation, spalling and delamination effect are major wear mechanism of heat-treated samples due to low volume fraction of the ferrite phase in heat treated samples.
- The cellular, columnar dendritic structure is noticed for 6 and 8% of WC composites, whereas the equiaxed dendritic structure is noticed for 10% of WC composite.
- From XRD analysis, WC, austenite phases are noticed and crystallite size is reduced by 21% when increasing WC content from 6% to 10%. In addition, WC, γFe, Fe_2W and Fe_3C phases are noticed in SS 316 composites.
- The hardness of 10%WC in SS 316 increased by 26% as compared to SS 316 and it can be due to fine grain structure and high dislocation density. The corrosion resistance increased by 58% for SS 316 composites as compared to SS 316. The wear resistance of 10%WC content is maximum and it is 61% higher than SS 316 because of its excellent lubricant properties and high hardness.

This study provides a path for building various engineering components by DED of SS 316. The properties of DED built SS 316L can be tailored by appropriate post-processing. Solution treatment of DED built SS 316 improved the homogeneity in microstructure, increased the plasticity retaining capability and elongation. On the other side, the corrosion resistance, wear-resistance and micro-hardness reduced with solution treatment. 8% WC doping ratio exhibited optimal combination of relative density, hardness, wear-resistance and corrosion resistance.

8.2 Future Scope

- The future approach can be study the mechanical properties such as compressive test, tensile test, creep and fatigue test of DED built SS 316 for bio medical applications.
- The design and fabricating of DED built SS 316 part can be done at optimum conditions for biomedical implants.
- Study the effect of different heat treatment conditions on the microstructure and mechanical properties of DED-built SS 316 composites.
- The erosion wear behaviour of DED-based additive manufactured SS 316 and its composites can be explored.
- Effect of post-treatment conditions on the surface characteristics of DED built SS 316 is analysed.
- Residual stress analysis on DED built SS 316 deposition using finite element analysis can also be performed.

References

[1] N. Tuncer, A. Bose, Solid-State Metal Additive Manufacturing: A Review, Additive Manufacturing: Beyond the beam technology, 72 (2020) 3090–3111. doi:10.1007/s11837-020-04260-y.

[2] N. Guo, M.C. Leu, Additive manufacturing: Technology, applications and research needs, Frontiers of Mechanical Engineering. 8 (2013) 215–243. doi:10.1007/s11465-013-0248-8.

[3] T. Debroy, H.L. Wei, J.S. Zuback, T. Mukherjee, J.W. Elmer, J.O. Milewski, A.M. Beese, A. Wilson-heid, A. De, W. Zhang, Additive manufacturing of metallic components – Process , structure and properties, Progress in Materials Science. 92 (2018) 112–224. doi:10.1016/j.pmatsci.2017.10.001.

[4] B. Dutta, S. Babu, B. Jared, Additive manufacturing technology, Technology and Applications of Metals in Additive Manufacturing, 2019, 11-53. doi:10.1016/b978-0-12-816634-5.00002-9.

[5] S. Cooke, K. Ahmadi, S. Willerth, R. Herring, Metal additive manufacturing: Technology, metallurgy and modelling, Journal of Manufacturing Processes. 57 (2020) 978–1003. doi:10.1016/j.jmapro.2020.07.025.

[6] M. Javaid, A. Haleem, Additive manufacturing applications in medical cases: A literature based review, Alexandria Journal of Medicine. 54 (2018) 411–422. doi:10.1016/j.ajme.2017.09.003.

[7] R. Liu, Z. Wang, T. Sparks, F. Liou, J. Newkirk, Aerospace applications of laser additive manufacturing, Laser Additive Manufacturing , (2017), 351-371 doi:10.1016/B978-0-08-100433-3.00013-0.

[8] R. Leal, F.M. Barreiros, L. Alves, F. Romeiro, J.C. Vasco, M. Santos, C. Marto, Additive manufacturing tooling for the automotive industry, International Journal of Advanced Manufacturing Technology. 92 (2017) 1671–1676. doi:10.1007/s00170-017-0239-8.

[9] K.S. Prakash, T. Nancharaih, V.V.S. Rao, Additive Manufacturing Techniques in Manufacturing -An Overview, Materials Today: Proceedings. 5 (2018) 3873–3882.

doi:10.1016/j.matpr.2017.11.642.

[10] G. Bansal, D.B. Singh, H.S. Virk, A. Devrani, A. Bhandari, Microstructural characterization, applications and process study of various additive manufacturing process: A review, Materials Today: Proceedings. 26 (2019) 833–837. doi:10.1016/j.matpr.2020.01.048.

[11] A. Bandyopadhyay, Y. Zhang, S. Bose, Recent developments in metal additive manufacturing, Current Opinion in Chemical Engineering. 28 (2020) 96–104. doi:10.1016/j.coche.2020.03.001.

[12] P.K. Gokuldoss, S. Kolla, J. Eckert, Additive manufacturing processes: Selective laser melting, electron beam melting and binder jetting-selection guidelines, Materials. 10 (2017) 672. doi:10.3390/ma10060672.

[13] B. Dutta, S. Babu, B. Jared, Comparison of various additive manufacturing technologies, Science, Technology and Applications of Metals in Additive Manufacturing. (2019) 55–76. doi:10.1016/b978-0-12-816634-5.00003-0.

[14] H.A. Derazkola, F. Khodabakhshi, A. Simchi, Evaluation of a polymer-steel laminated sheet composite structure produced by friction stir additive manufacturing (FSAM) technology, Polymer Testing. 90 (2020) 106690. doi:10.1016/j.polymertesting.2020.106690.

[15] Y. Zhang, L. Wu, X. Guo, S. Kane, Y. Deng, Y.G. Jung, J.H. Lee, J. Zhang, Additive Manufacturing of Metallic Materials: A Review, Journal of Materials Engineering and Performance. 27 (2018) 1–13. doi:10.1007/s11665-017-2747-y.

[16] B. Dutta, S. Babu, B. Jared, Metal additive manufacturing, Science, Technology and Applications of Metals in Additive Manufacturing. (2019) 1–10. doi:10.1016/b978-0-12-816634-5.00001-7.

[17] Y. Hu, W. Cong, A review on laser deposition-additive manufacturing of ceramics and ceramic reinforced metal matrix composites, Ceramics International. 44 (2018) 20599–20612. doi:10.1016/j.ceramint.2018.08.083.

[18] L. Yan, Y. Chen, F. Liou, Additive manufacturing of functionally graded metallic materials

using laser metal deposition, Additive Manufacturing. 31 (2020) 100901. doi:10.1016/j.addma.2019.100901.

[19] M. Ziaee, N.B. Crane, Binder jetting: A review of process, materials, and methods, Additive Manufacturing. 28 (2019) 781–801. doi:10.1016/j.addma.2019.05.031.

[20] C. Li, Z.Y. Liu, X.Y. Fang, Y.B. Guo, Residual Stress in Metal Additive Manufacturing, Procedia CIRP. 71 (2018) 348–353. doi:10.1016/j.procir.2018.05.039.

[21] X. Zhang, X. Wu, J. Shi, Additive manufacturing of zirconia ceramics: a state-of-the-art review, Journal of Materials Research and Technology. 9 (2020) 9029–9048. doi:10.1016/j.jmrt.2020.05.131.

[22] O. Diegel, A. Nordin, D. Motte, Additive Manufacturing Technologies, (2019) 19-39. doi:10.1007/978-981-13-8281-9_2.

[23] N. Shahrubudin, T.C. Lee, R. Ramlan, An overview on 3D printing technology: Technological, materials, and applications, Procedia Manufacturing. 35 (2019) 1286–1296. doi:10.1016/j.promfg.2019.06.089.

[24] C. Robinson, B. Stucker, K.C. Branch, J. Palmer, B. Strassner, S. Allen, R. Bugos, M. Navarrete, A. Lopes, E. Macdonald, F. Medina, R.B. Wicker, Fabrication of a Mini-Sar Antenna Array Using Ultrasonic Consolidation and Direct-Write, 2nd International Conference on Rapid Manufacturing. (2007) 30. https://www.osti.gov/servlets/purl/1267093.

[25] M.N. Gussev, N. Sridharan, M. Norfolk, K.A. Terrani, S.S. Babu, Effect of post weld heat treatment on the 6061 aluminum alloy produced by ultrasonic additive manufacturing, Materials Science and Engineering A. 684 (2017) 606–616. doi:10.1016/j.msea.2016.12.083.

[26] S. Singh, V.S. Sharma, A. Sachdeva, Progress in selective laser sintering using metallic powders: A review, Materials Science and Technology. 32 (2016) 760–772. doi:10.1179/1743284715Y.0000000136.

[27] C.P. Paul, A.N. Jinoop, K.S. Bindra, Metal additive manufacturing using lasers, in: Additive Manufacturing Applications and Innovations, Taylor & Francis Group, 2019.

[28] J. Lei, J. Xie, S. Zhou, H. Song, X. Song, X. Zhou, Comparative study on microstructure and corrosion performance of 316 stainless steel prepared by laser melting deposition with ring-shaped beam and Gaussian beam, Optics and Laser Technology. 111 (2019) 271–283. doi:10.1016/j.optlastec.2018.09.057.

[29] A.N. Jinoop, C.P. Paul, Laser-assisted directed energy deposition of nickel super alloys : A review, Journal of Materilas: Design and Applications. 0 (2019) 1–25. doi:10.1177/1464420719852658.

[30] O. Abdulhameed, A. Al-Ahmari, W. Ameen, S.H. Mian, Additive manufacturing: Challenges, trends, and applications, Advances in Mechanical Engineering. 11 (2019) 1–27. doi:10.1177/1687814018822880.

[31] E. Yasa, J.P. Kruth, Microstructural investigation of selective laser melting 316L stainless steel parts exposed to laser re-melting, Procedia Engineering. 19 (2011) 389–395. doi:10.1016/j.proeng.2011.11.130.

[32] C.H. Zhang, H. Zhang, C.L. Wu, S. Zhang, Z.L. Sun, S.Y. Dong, Multi-layer functional graded stainless steel fabricated by laser melting deposition, Vacuum. 141 (2017) 181–187. doi:10.1016/j.vacuum.2017.04.020.

[33] Y. Zhang, M. Xi, S. Gao, L. Shi, Characterization of laser direct deposited metallic parts, Journal of Materials Processing Technology. 142 (2003) 582–585. doi:10.1016/S0924-0136(03)00663-0.

[34] J.H. Robinson, I.R.T. Ashton, E. Jones, P. Fox, C. Sutcliffe, The effect of hatch angle rotation on parts manufactured using selective laser melting, Rapid Prototyping Journal. 25 (2019) 289–298. doi:10.1108/RPJ-06-2017-0111.

[35] W. Sun, Y. Ma, W. Huang, W. Zhang, X. Qian, Effects of build direction on tensile and fatigue performance of selective laser melting Ti6Al4V titanium alloy, International Journal of Fatigue. 130 (2020). doi:10.1016/j.ijfatigue.2019.105260.

[36] J.P. Rudolph, C. Emmelmann, Self-learning Calculation for Selective Laser Melting, Procedia CIRP. 67 (2018) 185–190. doi:10.1016/j.procir.2017.12.197.

[37] S.K. Everton, M. Hirsch, P.I. Stavroulakis, R.K. Leach, A.T. Clare, Review of in-situ

process monitoring and in-situ metrology for metal additive manufacturing, Materials and Design. 95 (2016) 431–445. doi:10.1016/j.matdes.2016.01.099.

[38] C. Wei, L. Li, X. Zhang, Y.H. Chueh, 3D printing of multiple metallic materials via modified selective laser melting, CIRP Annals. 67 (2018) 245–248. doi:10.1016/j.cirp.2018.04.096.

[39] D. Dai, D. Gu, Influence of thermodynamics within molten pool on migration and distribution state of reinforcement during selective laser melting of AlN/AlSi10Mg composites, International Journal of Machine Tools and Manufacture. 100 (2016) 14–24. doi:10.1016/j.ijmachtools.2015.10.004.

[40] P. Wang, C. Gammer, F. Brenne, T. Niendorf, J. Eckert, S. Scudino, A heat treatable TiB2/Al-3.5Cu-1.5Mg-1Si composite fabricated by selective laser melting: Microstructure, heat treatment and mechanical properties, Composites Part B: Engineering. 147 (2018) 162–168. doi:10.1016/j.compositesb.2018.04.026.

[41] M. Sergio, F. De Lima, S. Sankaré, Microstructure and mechanical behavior of laser additive manufactured AISI 316 stainless steel stringers, Journal of Materials&Design. 55 (2014) 526–532. doi:10.1016/j.matdes.2013.10.016.

[42] A. Das, M. Shukla, Surface morphology, bioactivity, and antibacterial studies of pulsed laser deposited hydroxyapatite coatings on Stainless Steel 254 for orthopedic implant applications, Proceedings of the Institution of Mechanical Engineers, Part L: Journal of Materials: Design and Applications. 233 (2019) 120–127. doi:10.1177/1464420716663029.

[43] A.N. Jinoop, C.P. Paul, S.K. Mishra, K.S. Bindra, Laser Additive Manufacturing using directed energy deposition of Inconel- 718 wall structures with tailored characteristics, Vacuum. 166 (2019) 270–278. doi:10.1016/j.vacuum.2019.05.027.

[44] Z. Gan, G. Yu, X. He, S. Li, International Journal of Heat and Mass Transfer Numerical simulation of thermal behavior and multicomponent mass transfer in direct laser deposition of Co-base alloy on steel, International Journal of Heat and Mass Transfer. 104 (2017) 28–38. doi:10.1016/j.ijheatmasstransfer.2016.08.049.

[45] K.D. Traxel, A. Bandyopadhyay, First Demonstration of Additive Manufacturing of Cutting

Tools using Directed Energy Deposition System: Stellite^{TM}-Based Cutting Tools, Additive Manufacturing. 25 (2019) 460–468. doi:10.1016/j.addma.2018.11.019.

[46] N. Chen, G. Ma, W. Zhu, A. Godfrey, Z. Shen, G. Wu, X. Huang, Enhancement of an additive-manufactured austenitic stainless steel by post-manufacture heat-treatment, Materials Science and Engineering A. 759 (2019) 65–69. doi:10.1016/j.msea.2019.04.111.

[47] B.R. Padhy, R.G. Reddy, Performance of DMFC with SS 316 bipolar/end plates, Journal of Power Sources. 153 (2006) 125–129. doi:10.1016/j.jpowsour.2005.02.089.

[48] H. Li, M. Ramezani, M. Li, C. Ma, J. Wang, Tribological performance of selective laser melted 316L stainless steel, Tribiology International. 128 (2018) 121–129. doi:10.1016/j.triboint.2018.07.021.

[49] Y. Zhu, J. Zou, X. Chen, H. Yang, Tribology of selective laser melting processed parts : Stainless steel 316 L under lubricated conditions, Wear. 350–351 (2016) 46–55. doi:10.1016/j.wear.2016.01.004.

[50] H. Li, M. Ramezani, M. Li, C. Ma, J. Wang, Effect of process parameters on tribological performance of 316L stainless steel parts fabricated by selective laser melting, Manufacturing Letters. 16 (2018) 36–39. doi:10.1016/j.mfglet.2018.04.003.

[51] Y. Sun, A. Moroz, K. Alrbaey, Sliding Wear Characteristics and Corrosion Behaviour of Selective Laser Melted 316L Stainless Steel, Journal of Materials Engineering & Performance. 23 (2014) 518–526. doi:10.1007/s11665-013-0784-8.

[52] J. Chen, Y. Yang, C. Song, D. Wang, S. Wu, M. Zhang, Influence mechanism of process parameters on the interfacial characterization of selective laser melting 316L/CuSn10, Materials Science and Engineering A. 792 (2020) 139316. doi:10.1016/j.msea.2020.139316.

[53] S. Mohd Yusuf, D. Lim, Y. Chen, S. Yang, N. Gao, Tribological behaviour of 316L stainless steel additively manufactured by laser powder bed fusion and processed via high-pressure torsion, Journal of Materials Processing Technology. 290 (2020) 116985. doi:10.1016/j.jmatprotec.2020.116985.

[54] R.J. Williams, J. Al-Lami, P.A. Hooper, M.S. Pham, C.M. Davies, Creep deformation and

failure properties of 316 L stainless steel manufactured by laser powder bed fusion under multiaxial loading conditions, Additive Manufacturing. (2020) 101706. doi:10.1016/j.addma.2020.101706.

[55] G. Sander, A.P. Babu, X. Gao, D. Jiang, N. Birbilis, On the effect of build orientation and residual stress on the corrosion of 316L stainless steel prepared by selective laser melting, Corrosion Science. (2020) 109149. doi:10.1016/j.corsci.2020.109149.

[56] M. Ahmed Obeidi, A. Mussatto, R. Groarke, R.K. Vijayaraghavan, A. Conway, F. Rossi Kaschel, E. McCarthy, O. Clarkin, R. O'Connor, D. Brabazon, Comprehensive assessment of spatter material generated during selective laser melting of stainless steel, Materials Today Communications. 25 (2020) 101294. doi:10.1016/j.mtcomm.2020.101294.

[57] Y. Song, Q. Sun, K. Guo, X. Wang, J. Liu, J. Sun, Effect of scanning strategies on the microstructure and mechanical behavior of 316L stainless steel fabricated by selective laser melting, Materials Science and Engineering A. 793 (2020) 139879. doi:10.1016/j.msea.2020.139879.

[58] J. Ghorbani, J. Li, A.K. Srivastava, Application of optimized laser surface re-melting process on selective laser melted 316L stainless steel inclined parts, Journal of Manufacturing Processes. 56 (2020) 726–734. doi:10.1016/j.jmapro.2020.05.025.

[59] V.H. Dao, J.M. Yu, K.B. Yoon, Anisotropic creep behavior of stainless steel produced by selective laser melting, Materials Science and Engineering A. 796 (2020) 140040. doi:10.1016/j.msea.2020.140040.

[60] Y. Sato, S. Srisawadi, D. Tanprayoon, T. Suga, T. Ohkubo, M. Tsukamoto, Spatter behavior for 316L stainless steel fabricated by selective laser melting in a vacuum, Optics and Lasers in Engineering. 134 (2020) 106209. doi:10.1016/j.optlaseng.2020.106209.

[61] G. Dursun, S. Ibekwe, G. Li, P. Mensah, G. Joshi, D. Jerro, Influence of laser processing parameters on the surface characteristics of 316L stainless steel manufactured by selective laser melting, Materials Today: Proceedings. 26 (2019) 387–393. doi:10.1016/j.matpr.2019.12.061.

[62] M. Laleh, A.E. Hughes, S. Yang, J. Li, W. Xu, I. Gibson, M.Y. Tan, Two and three-

dimensional characterisation of localised corrosion affected by lack-of-fusion pores in 316L stainless steel produced by selective laser melting, Corrosion Science. 165 (2020) 108394. doi:10.1016/j.corsci.2019.108394.

[63] S. Afkhami, M. Dabiri, H. Piili, T. Björk, Effects of manufacturing parameters and mechanical post-processing on stainless steel 316L processed by laser powder bed fusion, Materials Science and Engineering A. 802 (2021) 140660. doi:10.1016/j.msea.2020.140660.

[64] R.K. Upadhyay, A. Kumar, Scratch and wear resistance of additive manufactured 316L stainless steel sample fabricated by laser powder bed fusion technique, Wear. 458–459 (2020) 203437. doi:10.1016/j.wear.2020.203437.

[65] J.K. Veetil, M. Khorasani, A.H. Ghasemi, B. Rolfe, I. Vrooijink, K. Van Beurden, S. Moes, I. Gibson, Build position-based dimensional deviations of laser powder-bed fusion of stainless steel 316L, Precision Engineering. 67 (2021) 58–68. doi:10.1016/j.precisioneng.2020.09.024.

[66] L. Chen, B. Richter, X. Zhang, K.B. Bertsch, D.J. Thoma, F.E. Pfefferkorn, Effect of laser polishing on the microstructure and mechanical properties of stainless steel 316L fabricated by laser powder bed fusion, Materials Science and Engineering: A. (2020) 140579. doi:10.1016/j.msea.2020.140579.

[67] P. Deng, M. Karadge, R.B. Rebak, V.K. Gupta, B.C. Prorok, X. Lou, The origin and formation of oxygen inclusions in austenitic stainless steels manufactured by laser powder bed fusion, Additive Manufacturing. 35 (2020) 101334. doi:10.1016/j.addma.2020.101334.

[68] P. Margerit, D. Weisz-Patrault, K. Ravi-Chandar, A. Constantinescu, Tensile and ductile fracture properties of as-printed 316L stainless steel thin walls obtained by directed energy deposition, Additive Manufacturing. (2020) 101664. doi:10.1016/j.addma.2020.101664.

[69] I. Tolosa, F. Garciandía, F. Zubiri, Study of mechanical properties of AISI 316 stainless steel processed by “ selective laser melting ” , following different manufacturing strategies,The Internation Journal of Advanced Manufacturing Technology. (2010) 639–647. doi:10.1007/s00170-010-2631-5.

[70] M. Ma, Z. Wang, D. Wang, X. Zeng, Control of shape and performance for direct laser fabrication of precision large-scale metal parts with 316L Stainless Steel, Optics and Laser Technology. 45 (2013) 209–216. doi:10.1016/j.optlastec.2012.07.002.

[71] Y. Sun, Sliding wear behaviour of surface mechanical attrition treated AISI 304 stainless steel, Tribology International. 57 (2013) 67–75. doi:10.1016/j.triboint.2012.07.015.

[72] F. Weng, S. Gao, J. Jiang, J. Wang, P. Guo, A novel strategy to fabricate thin 316L stainless steel rods by continuous directed energy deposition in Z direction, Additive Manufacturing. 27 (2019) 474–481. doi:10.1016/j.addma.2019.03.024.

[73] K. Zhang, S. Wang, W. Liu, X. Shang, Characterization of stainless steel parts by Laser Metal Deposition Shaping, Journal of Materials and Design. 55 (2014) 104–119. doi:10.1016/j.matdes.2013.09.006.

[74] S.H. Riza, S.H. Masood, C. Wen, Wear behaviour of DMD-generated high-strength steels using multi-factor experiment design on a pin-on-disc apparatus, The International Journal of Advanced Manufacturing Technology. (2016) 461–477. doi:10.1007/s00170-016-8505-8.

[75] M.S.F. De Lima, S. Sankaré, Microstructure and mechanical behavior of laser additive manufactured AISI 316 stainless steel stringers, Materials and Design. 55 (2014) 526–532. doi:10.1016/j.matdes.2013.10.016.

[76] P. Guo, B. Zou, C. Huang, H. Gao, Study on microstructure, mechanical properties and machinability of efficiently additive manufactured AISI 316L stainless steel by high-power direct laser deposition, Journal of Materials Processing Technology. 240 (2017) 12–22. doi:10.1016/j.jmatprotec.2016.09.005.

[77] Z.E. Tan, J.H.L. Pang, J. Kaminski, H. Pepin, Characterisation of porosity, density, and microstructure of directed energy deposited stainless steel AISI 316L, Additive Manufacturing. 25 (2019) 286–296. doi:10.1016/j.addma.2018.11.014.

[78] F. Weng, S. Gao, J. Jiang, J.J. Wang, P. Guo, A novel strategy to fabricate thin 316L stainless steel rods by continuous directed energy deposition in Z direction, Additive Manufacturing. 27 (2019) 474–481. doi:10.1016/j.addma.2019.03.024.

[79] J.D. Majumdar, L. Li, Studies on direct laser cladding of SiC dispersed AISI 316L stainless steel, Metallurgical and Materials Transactions A: Physical Metallurgy and Materials Science. 40 (2009) 3001–3008. doi:10.1007/s11661-009-0018-8.

[80] D.R. Feenstra, V. Cruz, X. Gao, A. Molotnikov, N. Birbilis, Effect of Build Height on the Properties of Large Format Stainless Steel 316L Fabricated via Directed Energy Deposition, Additive Manufacturing. (2020) 101205. doi:10.1016/j.addma.2020.101205.

[81] A. Yadollahi, N. Shamsaei, S.M. Thompson, D.W. Seely, Effects of process time interval and heat treatment on the mechanical and microstructural properties of direct laser deposited 316L stainless steel, Materials Science and Engineering A. 644 (2015) 171–183. doi:10.1016/j.msea.2015.07.056.

[82] X. Chen, J. Li, X. Cheng, H. Wang, Z. Huang, Effect of heat treatment on microstructure, mechanical and corrosion properties of austenitic stainless steel 316L using arc additive manufacturing, Materials Science and Engineering A. 715 (2018) 307–314. doi:10.1016/j.msea.2017.10.002.

[83] O.O. Salman, C. Gammer, A.K. Chaubey, J. Eckert, S. Scudino, Effect of heat treatment on microstructure and mechanical properties of 316L steel synthesized by selective laser melting, Materials Science and Engineering A. 748 (2019) 205–212. doi:10.1016/j.msea.2019.01.110.

[84] D. Kong, C. Dong, X. Ni, L. Zhang, J. Yao, C. Man, X. Cheng, K. Xiao, X. Li, Mechanical properties and corrosion behavior of selective laser melted 316L stainless steel after different heat treatment processes, Journal of Materials Science and Technology. 35 (2019) 1499–1507. doi:10.1016/j.jmst.2019.03.003.

[85] E. Tascioglu, Y. Karabulut, Y. Kaynak, Influence of heat treatment temperature on the microstructural , mechanical , and wear behavior of 316L stainless steel fabricated by laser powder bed additive manufacturing, (2020) 1947–1956.

[86] M.S.I.N. Kamariah, W.S.W. Harun, N.Z. Khalil, F. Ahmad, M.H. Ismail, S. Sharif, Effect of heat treatment on mechanical properties and microstructure of selective laser melting 316L stainless steel, IOP Conference Series: Materials Science and Engineering. 257

(2017). doi:10.1088/1757-899X/257/1/012021.

[87] K. Saeidi, X. Gao, F. Lofaj, L. Kvetková, Z.J. Shen, Transformation of austenite to duplex austenite-ferrite assembly in annealed stainless steel 316L consolidated by laser melting, Journal of Alloys and Compounds. 633 (2015) 463–469. doi:10.1016/j.jallcom.2015.01.249.

[88] K. Saeidi, X. Gao, Y. Zhong, Z.J. Shen, Hardened austenite steel with columnar sub-grain structure formed by laser melting, Materials Science and Engineering A. 625 (2015) 221–229. doi:10.1016/j.msea.2014.12.018.

[89] D. Kong, X. Ni, C. Dong, L. Zhang, C. Man, J. Yao, K. Xiao, X. Li, Heat treatment effect on the microstructure and corrosion behavior of 316L stainless steel fabricated by selective laser melting for proton exchange membrane fuel cells, Electrochimica Acta. 276 (2018) 293–303. doi:10.1016/j.electacta.2018.04.188.

[90] M. Laleh, A.E. Hughes, W. Xu, P. Cizek, M.Y. Tan, Unanticipated drastic decline in pitting corrosion resistance of additively manufactured 316L stainless steel after high-temperature post-processing, Corrosion Science. 165 (2020) 108412. doi:10.1016/j.corsci.2019.108412.

[91] C.L. Wu, S. Zhang, C.H. Zhang, J.B. Zhang, Y. Liu, J. Chen, Effects of SiC content on phase evolution and corrosion behavior of SiC-reinforced 316L stainless steel matrix composites by laser melting deposition, Optics and Laser Technology. 115 (2019) 134–139. doi:10.1016/j.optlastec.2019.02.029.

[92] P.K. Farayibi, T.E. Abioye, A. Kennedy, A.T. Clare, Development of metal matrix composites by direct energy deposition of ‘satellited’ powders, Journal of Manufacturing Processes. 45 (2019) 429–437. doi:10.1016/j.jmapro.2019.07.029.

[93] P. Xu, C.X. Lin, C.Y. Zhou, X.P. Yi, Wear and corrosion resistance of laser cladding AISI 304 stainless steel/Al2O3 composite coatings, Surface and Coatings Technology. 238 (2014) 9–14. doi:10.1016/j.surfcoat.2013.10.028.

[94] C.P. Paul, S.K. Mishra, P. Tiwari, L.M.Kukreja, Solid-Particle Erosion Behaviour of WC_Ni Composite Clad layers with Different Contents of WC Particles, Optics and Laser Technology.50(2013) 155–162.

[95] A.I. Gorunov, Investigation microstructure of carbon fibers reinforced composite on Fe and Ni-based obtained by laser metal deposition, Surface and Coatings Technology. 364 (2019) 279–288. doi:10.1016/j.surfcoat.2019.03.006.

[96] S. Cao, D. Gu, Laser metal deposition additive manufacturing of TiC / Inconel 625 nanocomposites : Relation of densi fi cation , microstructures and performance, Journal of Material Research. 30(2015) 3616-3628. doi:10.1557/jmr.2015.358.

[97] I. Shishkovsky, F. Missemer, I. Smurov, Metal matrix composites with ternary intermetallic inclusions fabricated by laser direct energy deposition, Composite Structures. 183 (2018) 663–670. doi:10.1016/j.compstruct.2017.09.004.

[98] A. Ramakrishnan, G.P. Dinda, Microstructural control of an Al–W aluminum matrix composite during direct laser metal deposition, Journal of Alloys and Compounds. 813 (2020) 152208. doi:10.1016/j.jallcom.2019.152208.

[99] J.C. Betts, B.L. Mordike, M. Grech, Characterisation, wear and corrosion testing of laser-deposited AISI 316 reinforced with ceramic particles, Surface Engineering. 26 (2010) 21–29. doi:10.1179/174329409X433920.

[100] J.C. Li, X. Lin, N. Kang, J.L. Lu, Q.Z. Wang, W.D. Huang, Microstructure, tensile and wear properties of a novel graded Al matrix composite prepared by direct energy deposition, Journal of Alloys and Compounds.826 (2020) 154077. doi:10.1016/j.jallcom.2020.154077.

[101] Y. Huang, D. Wu, D. Zhao, F. Niu, H. Zhang, S. Yan, G. Ma, Process Optimization of Melt Growth Alumina/Aluminum Titanate Composites Directed Energy Deposition: Effects of Scanning Speed, Additive Manufacturing. (2020) 1010210. doi:10.1016/j.addma.2020.101210.

[102] Y. Liu, M. Tang, Q. Hu, Y. Zhang, L. Zhang, Densification behavior, microstructural evolution, and mechanical properties of TiC/AISI420 stainless steel composites fabricated by selective laser melting, Materials and Design. 187 (2020) 108381. doi:10.1016/j.matdes.2019.108381.

[103] A. Mandal, J.K. Tiwari, N. Sathish, A.K. Srivastava, Microstructural and mechanical properties evaluation of graphene reinforced stainless steel composite produced via

selective laser melting, Materials Science and Engineering A. 774 (2020) 138936. doi:10.1016/j.msea.2020.138936.

[104] S. Wen, K. Chen, W. Li, Y. Zhou, Q. Wei, Y. Shi, Selective laser melting of reduced graphene oxide/S136 metal matrix composites with tailored microstructures and mechanical properties, Materials and Design. 175 (2019) 107811. doi:10.1016/j.matdes.2019.107811.

[105] O.O. Salman, C. Gammer, J. Eckert, M.Z. Salih, E.H. Abdulsalam, K.G. Prashanth, S. Scudino, Selective laser melting of 316L stainless steel : In fl uence of TiB 2 addition on microstructure and mechanical properties, Materials Today Communications. 21 (2019) 100615. doi:10.1016/j.mtcomm.2019.100615.

[106] Y. Han, Y. Zhang, H. Jing, D. Lin, L. Zhao, L. Xu, P. Xin, Selective laser melting of low-content graphene nanoplatelets reinforced 316L austenitic stainless steel matrix: Strength enhancement without affecting ductility, Additive Manufacturing. 34 (2020) 101381. doi:10.1016/j.addma.2020.101381.

[107] W. Zhai, Z. Zhu, W. Zhou, S.M.L. Nai, J. Wei, Selective laser melting of dispersed TiC particles strengthened 316L stainless steel, Composites Part B: Engineering. 199 (2020) 108291. doi:10.1016/j.compositesb.2020.108291.

[108] C. Li, Z. Yu, J. Gao, J. Zhao, X. Han, Numerical simulation and experimental study of cladding Fe60 on an ASTM 1045 substrate by laser cladding, Surface & Coatings Technology. 357 (2019) 965–977. doi:10.1016/j.surfcoat.2018.10.099.

[109] W. Ya, B. Pathiraj, S. Liu, 2D modelling of clad geometry and resulting thermal cycles during laser cladding, Journal of Materials Processing Technology. 230 (2016) 217–232.

[110] S. Morville, M. Carin, M. Muller, M. Gharbi, P. Peyre, D. Carron, P. Le, 2D axial-symmetric model for fluid flow and heat transfer in the melting and resolidification of a vertical cylinder, Excerpt from the Proceedings of the COMSOL Conference. 2010 Paris.

[111] V. Neela, A. De, Three-dimensional heat transfer analysis of LENS TM process using finite element method, The International Journal of Adavanced Manufacturing Technology. 45 (2009) 935–943. doi:10.1007/s00170-009-2024-9.

[112] A. Fathi, E. Toyserkani, A. Khajepour, Prediction of melt pool depth and dilution, Journal

of Physics D: Applied Physics. 39 (2006) 2613–2623. doi:10.1088/0022-3727/39/12/022.

[113] S. Wen, Y.C. Shin, Modeling of transport phenomena during the coaxial laser direct deposition process, Journal of Applied Physics, 108 (2012) 044908. doi:10.1063/1.3474655.

[114] P. Peyre, P. Aubry, R. Fabbro, R. Neveu, A. Longuet, Analytical and numerical modelling of the direct metal deposition laser process, Journal of Physics D: Applied Physics 41 (2008) 025403. doi:10.1088/0022-3727/41/2/025403.

[115] E. Toyserkani, A. Khajepour, S. Corbin, 3-D finite element modeling of laser cladding by powder injection : effects of laser pulse shaping on the process, Optics and Lasers in Engineering. 41 (2004) 849–867. doi:10.1016/S0143-8166(03)00063-0.

[116] A. Baumard, D. Ayrault, O. Fandeur, C. Bordreuil, F. Deschaux-beaume, Numerical prediction of grain structure formation during laser powder bed fusion of 316 L stainless steel, Materials & Design. 199 (2021) 109434. doi:10.1016/j.matdes.2020.109434.

[117] Y. Tian, L. Yang, D. Zhao, Y. Huang, J. Pan, Numerical analysis of powder bed generation and single track forming for selective laser melting of SS 316L stainless steel, Journal of Manufacturing Processes. 58 (2020) 964–974. doi:10.1016/j.jmapro.2020.09.002.

[118] D. Gu, J. Ma, H. Chen, K. Lin, L. Xi, Laser additive manufactured WC reinforced Fe-based composites with gradient reinforcement/matrix interface and enhanced performance, Composite Structures. 192 (2018) 387–396. doi:10.1016/j.compstruct.2018.03.008.

[119] K. Benarji, Y.R. Kumar, C.P. Paul, A.N. Jinoop, K.S. Bindra, Parametric investigation and characterization on SS 316 built by laser-assisted directed energy deposition, Proceedings of the Institution of Mechanical Engineers, Part L: Journal of Materials: Design and Applications. 0 (2019) 1–15. doi:10.1177/1464420719894718.

[120] K. Zhang, S. Wang, W. Liu, X. Shang, Characterization of stainless steel parts by Laser Metal Deposition Shaping, Materials and Design. 55 (2014) 104–119. doi:10.1016/j.matdes.2013.09.006.

[121] S. Wang, L. Zhu, J.Y.H. Fuh, H. Zhang, W. Yan, Multi-physics modeling and Gaussian process regression analysis of cladding track geometry for direct energy deposition, Optics

and Lasers in Engineering. 127 (2020) 105950. doi:10.1016/j.optlaseng.2019.105950.

[122] Y. Huang, M.B. Khamesee, E. Toyserkani, A new physics-based model for laser directed energy deposition (powder-fed additive manufacturing): From single-track to multi-track and multi-layer, Optics and Laser Technology. 109 (2019) 584–599. doi:10.1016/j.optlastec.2018.08.015.

[123] S. Wang, L. Zhu, J.Y.H. Fuh, H. Zhang, W. Yan, Multi-physics modeling and Gaussian process regression analysis of cladding track geometry for direct energy deposition, Optics and Lasers in Engineering. 127 (2020) 105950. doi:10.1016/j.optlaseng.2019.105950.

[124] J.S. Zuback, T. Debroy, The Hardness of Additively Manufactured Alloys, Materials. 11(2018) 2070. doi:10.3390/ma11112070.

[125] Z. Hu, H. Zhu, H. Zhang, X. Zeng, Experimental investigation on selective laser melting of 17-4PH stainless steel, Optics and Laser Technology. 87 (2017) 17–25. doi:10.1016/j.optlastec.2016.07.012.

[126] K. Saeidi, X. Gao, Y. Zhong, Z.J. Shen, Materials Science & Engineering A Hardened austenite steel with columnar sub-grain structure formed by laser melting, Materials Science & Engineering A. 625 (2015) 221–229. doi:10.1016/j.msea.2014.12.018.

[127] T. Durejko, M. Pola, I. Kunce, P. Tomasz, K.J. Kurzyd, Z. Bojar, The microstructure , mechanical properties and corrosion resistance of 316 L stainless steel fabricated using laser engineered net shaping, Materials Science & Engineering A. 677 (2016) 1–10. doi:10.1016/j.msea.2016.09.028.

[128] F. Bartolomeu, M. Buciumeanu, E. Pinto, N. Alves, O. Carvalho, F.S. Silva, G. Miranda, 316L stainless steel mechanical and tribological behavior — A comparison between selective laser melting , hot pressing and conventional casting, Additive Manufacturing. 16 (2017) 81–89. doi:10.1016/j.addma.2017.05.007.

[129] M.C.M. Farias, R.M. Souza, A. Sinatora, D.K. Tanaka, The influence of applied load, sliding velocity and martensitic transformation on the unlubricated sliding wear of austenitic stainless steels, Wear. 263 (2007) 773–781. doi:10.1016/j.wear.2006.12.017.

[130] M.S.I.N. Kamariah, W.S.W. Harun, N.Z. Khalil, F. Ahmad, M.H. Ismail, S. Sharif, Effect

of heat treatment on mechanical properties and microstructure of selective laser melting 316L stainless steel, IOP Conference Series: Materials Science and Engineering. 257 (2017) 012021. doi:10.1088/1757-899X/257/1/012021.

[131] A.N. Jinoop, C.P. Paul, S.K. Mishra, K.S. Bindra, Laser Additive Manufacturing using directed energy deposition of Inconel-718 wall structures with tailored characteristics, Vacuum. 166 (2019) 270–278. doi:10.1016/j.vacuum.2019.05.027.

[132] M. Ziętala, T. Durejko, M. Polański, I. Kunce, T. Płociński, W. Zieliński, M. Łazińska, W. Stępniowski, T. Czujko, K.J. Kurzydłowski, Z. Bojar, The microstructure, mechanical properties and corrosion resistance of 316 L stainless steel fabricated using laser engineered net shaping, Materials Science and Engineering A. 677 (2016) 1–10. doi:10.1016/j.msea.2016.09.028.

[133] A. V. Bansod, A.P. Patil, J. Verma, S. Shukla, Microstructure, mechanical and electrochemical evaluation of dissimilar low Ni SS and 304 SS using different filler materials, Materials Research. 22 (2019) 1–14. doi:10.1590/1980-5373-MR-2017-0203.

[134] Y. Cui, C.D. Lundin, Austenite-preferential corrosion attack in 316 austenitic stainless steel weld metals, Materials and Design. 28 (2007) 324–328. doi:10.1016/j.matdes.2005.05.022.

[135] C.C. Silva, H.C. Miranda, H.B. de Sant’Ana, J.P. Farias, Austenitic and ferritic stainless steel dissimilar weld metal evaluation for the applications as-coating in the petroleum processing equipment, Materials and Design. 47 (2013) 1–8. doi:10.1016/j.matdes.2012.11.048.

[136] A.N. Jinoop, J. Denny, C.P. Paul, J. Ganesh Kumar, K.S. Bindra, Effect of post heat-treatment on the microstructure and mechanical properties of Hastelloy-X structures manufactured by laser based Directed Energy Deposition, Journal of Alloys and Compounds. 797 (2019) 399–412. doi:10.1016/j.jallcom.2019.05.050.

[137] M. Hussain, V. Mandal, V. Kumar, A.K. Das, S.K. Ghosh, Development of TiN particulates reinforced SS 316 based metal matrix composite by direct metal laser sintering technique and its characterization, Optics and Laser Technology. 97 (2017) 46–59. doi:10.1016/j.optlastec.2017.06.006.

[138] D.S. Prasad, C. Shoba, N. Ramanaiah, Investigations on mechanical properties of aluminum hybrid composites, Journal of Materials Research and Technology. 3 (2014) 79–85. doi:10.1016/j.jmrt.2013.11.002.

[139] J. Wang, L. Li, W. Tao, Crack initiation and propagation behavior of WC particles reinforced Fe-based metal matrix composite produced by laser melting deposition, Optics and Laser Technology. 82 (2016) 170–182. doi:10.1016/j.optlastec.2016.03.008.

[140] Y. Hu, F. Ning, X. Wang, H. Wang, B. Zhao, W. Cong, Y. Li, Laser deposition-additive manufacturing of in situ TiB reinforced titanium matrix composites: TiB growth and part performance, International Journal of Advanced Manufacturing Technology. 93 (2017) 3409–3418. doi:10.1007/s00170-017-0769-0.

[141] S. Liu, Y. Wang, T. Muthuramalingam, G. Anbuchezhiyan, Effect of B4C and MOS2 reinforcement on micro structure and wear properties of aluminum hybrid composite for automotive applications, Composites Part B: Engineering. 176 (2019). doi:10.1016/j.compositesb.2019.107329.

[142] Y. Yang, C. Zhang, D. Wang, L. Nie, D. Wellmann, Y. Tian, Additive manufacturing of WC-Co hardmetals, The International Journal of Advanced Manufacturing Technology, 108 (2020) 1653–1673.

[143] N. A. Ahmad , Z. Kamdi, A. L. M. Tobi, Wear and corrosion behavior of tungsten carbide based coating on carbon steel, International Journal of Integrated Engineering. 10 (2018) 119-125.

[144] Y. Xu, Y. Gong, P. Li, Y. Yang, Y. Qi, The effect of laser power on the microstructure and wear performance of IN718 superalloy fabricated by laser additive manufacturing, International Journal of Advanced Manufacturing Technology. 108 (2020) 2245–2254. doi:10.1007/s00170-020-05172-6.

[145] X. Yan, C. Huang, C. Chen, R. Bolot, L. Dembinski, R. Huang, W. Ma, H. Liao, M. Liu, Additive manufacturing of WC reinforced maraging steel 300 composites by cold spraying and selective laser melting, Surface and Coatings Technology. 371 (2019) 161–171. doi:10.1016/j.surfcoat.2018.03.072.

Appendix-1

Finite element analysis

Governing equations

An axisymmetric model with the dimension of (5 x 2 mm) has been developed to predict the track geometry and thermal analysis during DED process using Comsol Multiphysics 5.3. The energy and mass balance equations (1A and 2A) are used in the present analysis [109].

$$\rho C_p \frac{\partial (T)}{\partial t} + \rho C_p \mathrm{V_n} \Delta T + \nabla(-K\Delta T) = Q_r \text{-} \mathrm{Q}_{\mathrm{loss}} \tag{1A}$$

$$\eta = \frac{A_t \rho v}{m} \tag{2A}$$

where $\rho\ is\ density\ (\frac{kg}{m^3})$, T is temperature (K) , C_p is specific heat capacity (J/kg.K), t is time (s), V_n is boundary velocity (m/s) , Q_r is heat source $(\frac{W}{m^2})$ and K is thermal conductivity (W/m^2K), Q_{loss} is the energy lost into ambient air by thermal radiation, convection and heat conduction, A_t is track area, η is powder efficiency and v is scanning speed.

Heat source

Temperature distributions have a significant impact on the track geometry created during laser deposition. The energy absorbed by the substrate and powder components determines the temperature distributions inside the melt pool. The laser energy used in this current study is implemented by equation (3A) [110] .For the Nd:YAG laser, the absorption by steel substrate is assumed to be constant, with a value of roughly 0.47. Using the rule of mixtures, the absorptivity of various alloys may be estimated given their composition and the absorptivity of the constituent elements.

$$Q_r = \frac{(4.45AP)}{\pi r^2} \exp(-4.5\ \frac{(r-vt)^2}{r^2})) \tag{3A}$$

Here, the substrate temperature is considered to be room temperature , A is a fraction of heat input to powder, P is laser power, v is scanning speed, r is laser beam radius, ε is emissivity, m is powder feed rate and h is convective heat transfer coefficient. The parameters are used for the FEM analysis presented in Table 1A.

Table 1A: Parameters used for finite element analysis

Parameters	Values
A	0.47
ρ_o	7000 $\frac{kg}{m^3}$
r	1.6 mm
T_o	273.15 K
h	10 $\frac{W}{m^2K}$
ε	0.7
C_p	500 J/kg.K
K	16 W/mK

Boundary conditions

Heat source and moving mesh equations (3A and 5A) are assigned to the boundary 1 as shown in figure 1A. Surface 1 is subjected to convection and radiation by considering heat exchange between the substrate and the surroundings. Surfaces 2 and 3 are the work piece's vertical surfaces that are thought to experience natural convection and radiation.

$$Q_{\text{loss}} = h\,(T - T_o) + \sigma_b \varepsilon (T^4 - T_o^4) \qquad (4A)$$

Where h is heat transfer coefficient. Q_{loss} is the sum of heat loss as thermal radiation, heat convection with ambient air in Eq. (4A). The track geometry is developed by using moving mesh which takes into account for mass addition and solidification phase changes. V_n is boundary velocity due to powder addition and r_p is mean diameter of the powder particles. The calculation of V_n is given by equation 5A [109]:

$$V_n = \frac{\mathbf{2\eta m}}{\boldsymbol{\rho\pi r_p^2}} \exp(-4.5\ \frac{(r-vt)^2}{r_p^2}) \qquad (5A)$$

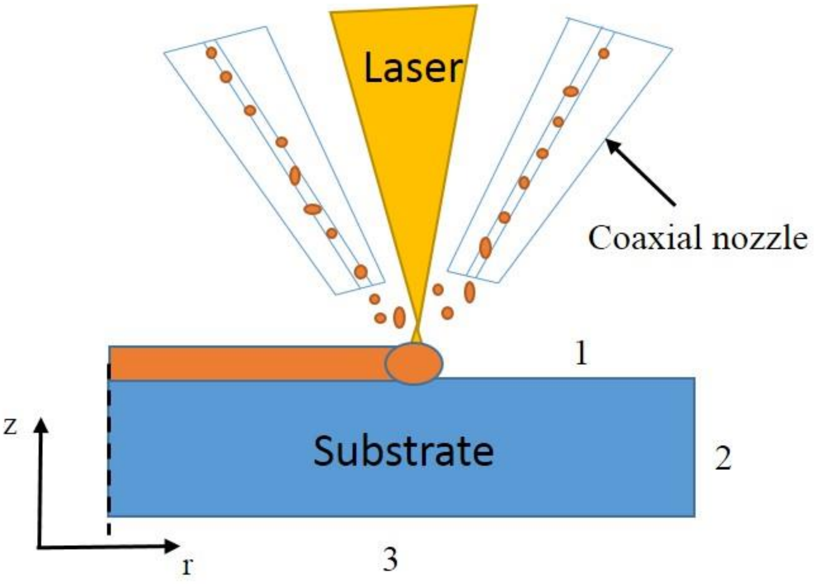

Figure 1A. Schematic axi-symmetric model for DED

Table 2A: Boundary conditions

Heat transfer	Boundary 1	Boundary 2,3
	$Q_r = \frac{(4.45AP)}{\pi r^2} \exp(-4.5\ \frac{(r-vt)^2}{r^2})$ $Q_{\text{loss}} = h\,(T - T_o) - \sigma_b \varepsilon (T^4 - T_o^4)$	$Q_{\text{loss}} = h\,(T - T_o) -$ $\sigma_b \varepsilon (T^4 - T_o^4)$
Deformed geometry	V_n	$V_n=0$

Resolution Parameters & Mesh

The triangular mesh is applied to model are shown in figure 2A. The highest and minimum mesh sizes are 50 μm and 0.1 μm, respectively. The material deposition throughout the DED process is shown by the expansion of the top surface. The moving mesh is controlled by D_g nodes in COMSOL using the laplace smoothing approach. The direct PARDISO solver is used in conjunction with the generalized- time solver to accomplish the iterative solution. The relative and absolute tolerances are 10^{-2} and 10^{-3}, respectively.

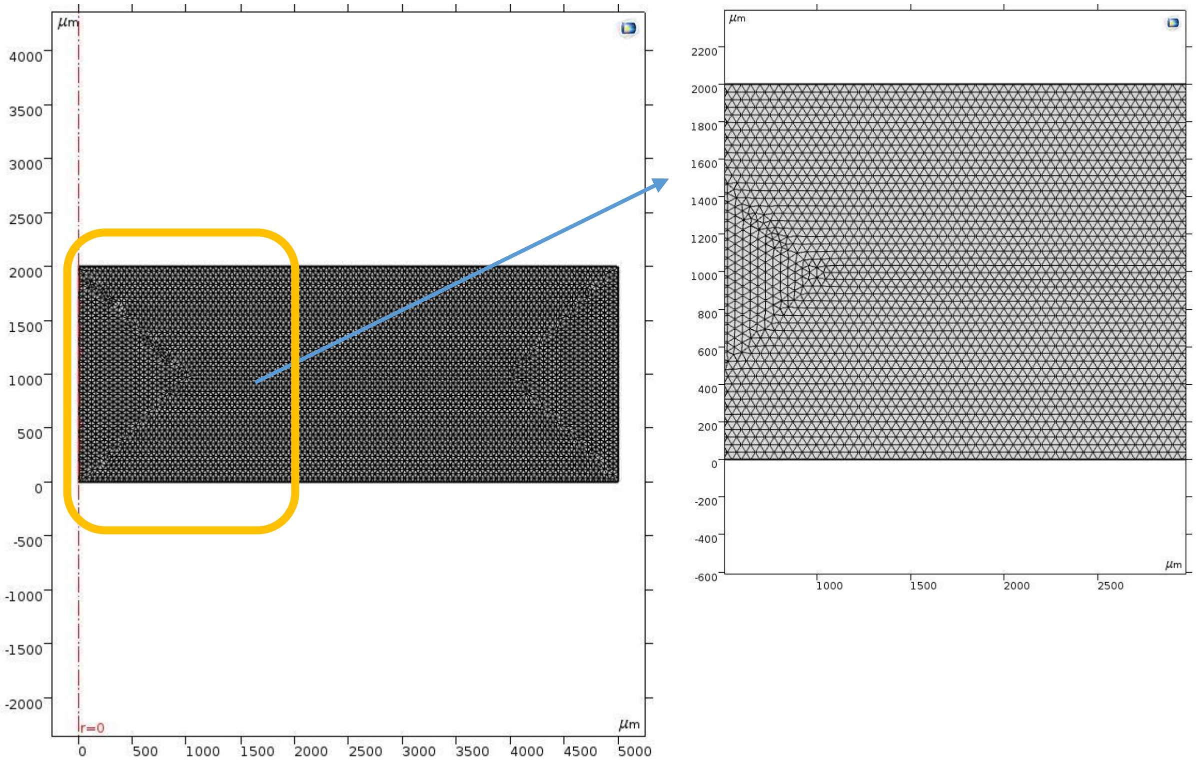

a b

Figure 2A. a) Illustration of substrate after mesh b) Enlarged view

Appendix-2

Specific wear data

Scanning speed (m/min)	**At normal load of 10 N**					
	SWR at Sliding velocity 0.5 m/sec	Standard deviation error	SWR at Sliding velocity 0.75 m/sec	Standard deviation error	SWR at Sliding velocity 0.1 m/sec	Standard deviation error
0.4	0.02497	9.50E-04	0.04817	0.00275	0.0635	0.00507
0.5	0.15133	0.00709	0.16217	0.00701	0.2875	0.0075
0.6	0.18557	0.00565	0.22383	0.01366	0.295	0.005
	At normal load of 20 N					
0.4	0.04167	0.00946	0.07516	0.00202	0.08163	0.0047
0.5	0.09273	0.00582	0.13958	0.01909	0.16717	0.01013
0.6	0.20916	0.02919	0.22917	0.02126	0.24208	0.00804
	At normal load of 30 N					
0.4	0.07022	0.02023	0.0841	0.03282	0.102	0.01682
0.5	0.102	0.01682	0.12027	0.0101	0.138	0.03143
0.6	0.14131	0.04425	0.19383	0.03598	0.23605	0.01449
	SWR after heat treatment					
As built	0.02497	9.50E-04				
HT 1073	0.175	0.01768				
HT 1273	0.19375	0.00884				
	SWR for composite					
SS 316	0.08163	0.0047				
6% WC	0.046	0.0057				
8% WC	0.038	0.00625				
10% WC	0.03107	0.0052				

Coefficient of friction data

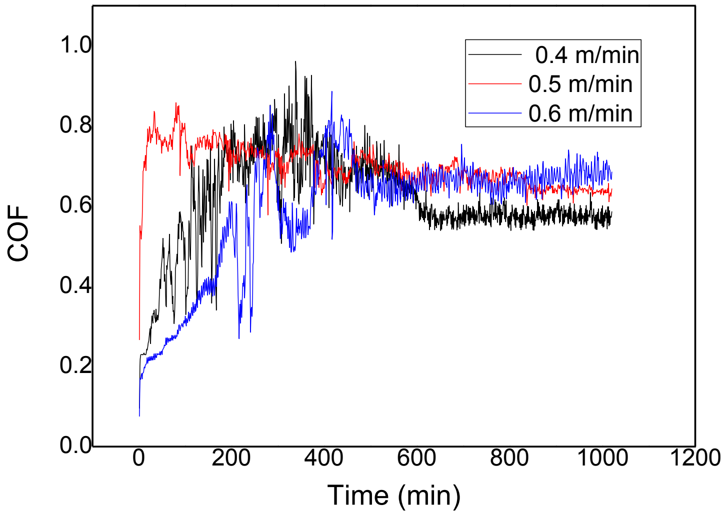

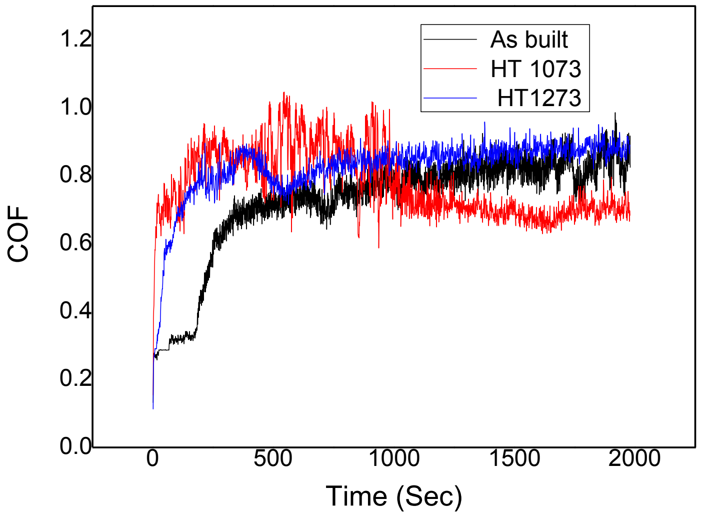

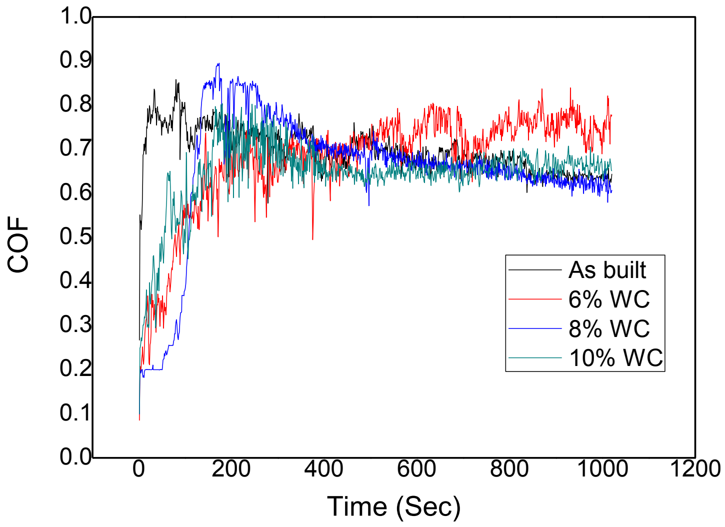
COF
1.0
0.9
0.8
0.7
0.6
0.5
0.4
0.3
0.2
0.1
0.0
0
200
400
600
800
1000
1200
Time (Sec)
As built
6% WC
8% WC
10% WC